Edgar José Sanches Mascarenhas

Licenciatura em Ciências da Engenharia Biomédica

Mechanical characterization of aortas using 2D ultrasound elastography

Dissertação para obtenção do Grau de Mestre em Engenharia Biomédica

Orientadores: Richard Loptata, Professor Auxiliar, Technische Universiteit Eindhoven, Holanda
Mathijs Peters, M.Sc., Technische Universiteit Eindhoven, Holanda

Co-orientador: Pedro Vieira, Professor Auxiliar, FCT-UNL

Júri:

Presidente: Prof. Doutora Carla Maria Quintão Pereira

Arguente: Prof. Doutor Mário António Basto Forjaz Secca

Vogal: Prof. Doutor Pedro Manuel Cardoso Vieira

FACULDADE DE CIÊNCIAS E TECNOLOGIA
UNIVERSIDADE NOVA DE LISBOA

[Outubro 2014]

Mechanical characterization of aortas using 2D ultrasound elastography

Acknowledgments

First, I would like to thank Professor Frans van de Vosse for welcoming me in the Cardiovascular Biomechanics Group at Technische Universiteit Eindhoven (TU/e), and giving this great opportunity of doing my master thesis in his research group.

Secondly, a deep and meaningful thanks to my supervisor Richard Lopata, for believing in my work and being always present, while giving me the freedom to build my own path at the same time. Richard, I will always be grateful for your guidance during these seven months. With you I learnt not only scientific method, but far beyond the books and conventional.

I would also like to thank my daily supervisor Mathijs Peters for the assistance during the development of this thesis, in particular with laboratory procedures. Mathijs, thank you for all the support, without pre-scheduling meetings or formalities since the first day.

I kindly thank Professor Mário Forjaz Secca for supporting me in establishing the required agreement between both universities.

A word to Professor Pedro Vieira for remaining my link to FCT-UNL and for the help provided during the seven months abroad.

I also want to express my gratitude to all Master students at TU/e who worked by my side and to the *Dispuut 3004* – TU/e Materials Technology Student Association. This was a remarkable experience, and part of it was also due to the friends from around the world that gathered for the Spring semester at TU/e in 2014.

To all my friends in Portugal with whom I shared this journey on the last five years, Rui Dinis, Bruno Ribeiro, João Tavares, Artur Gonçalves, Manuel Coelho, Alexandre Medina, Ana Isabel Sousa, Luísa Fialho, Andreia Serrano, Inês Ropio and Joana Costa, you have made this 5-year journey more fun and pleasant.

Finally, a special thanks to my family, my parents and my sister for their unconditional support and for always encouraging me to face new challenges.

Abstract

Rupture of aortic aneurysms (AA) is a major cause of death in the Western world. Currently, clinical decision upon surgical intervention is based on the diameter of the aneurysm. However, this method is not fully adequate. Noninvasive assessment of the elastic properties of the arterial wall can be a better predictor for AA growth and rupture risk.

The purpose of this study is to estimate mechanical properties of the aortic wall using *in vitro* inflation testing and 2D ultrasound (US) elastography, and investigate the performance of the proposed methodology for physiological conditions.

Two different inflation experiments were performed on twelve porcine aortas: 1) a static experiment for a large pressure range (0 – 140 mmHg); 2) a dynamic experiment closely mimicking the *in vivo* hemodynamics at physiological pressures (70 – 130 mmHg). 2D raw radiofrequency (RF) US datasets were acquired for one longitudinal and two cross-sectional imaging planes, for both experiments. The RF-data were manually segmented and a 2D vessel wall displacement tracking algorithm was applied to obtain the aortic diameter–time behavior. The shear modulus G was estimated assuming a Neo-Hookean material model. In addition, an incremental study based on the static data was performed to: 1) investigate the changes in G for increasing mean arterial pressure (MAP), for a certain pressure difference (30, 40, 50 and 60 mmHg); 2) compare the results with those from the dynamic experiment, for the same pressure range.

The resulting shear modulus G was 94 ± 16 kPa for the static experiment, which is in agreement with literature. A linear dependency on MAP was found for G, yet the effect of the pressure difference was negligible. The dynamic data revealed a G of 250 ± 20 kPa. For the same pressure range, the incremental shear modulus (G_{inc}) was 240 ± 39 kPa, which is in agreement with the former. In general, for all experiments, no significant differences in the values of G were found between different image planes.

This study shows that 2D US elastography of aortas during inflation testing is feasible under controlled and physiological circumstances. In future studies, the *in vivo*, dynamic experiment should be repeated for a range of MAPs and pathological vessels should be examined. Furthermore, the use of more complex material models needs to be considered to describe the non-linear behavior of the vascular tissue.

Key-words: aortic aneurysm, vascular biomechanics, inflation testing, 2D ultrasound elastography

Resumo

A rutura de aneurismas da aorta (AA) é das principais causas de morte no mundo ocidental. Atualmente, a decisão clínica sobre a realização de uma intervenção cirúrgica é baseada no diâmetro do aneurisma. Contudo, este método não é o mais adequado. A avaliação não invasiva das propriedades elásticas da parede da artéria poderá ser um melhor indicador na previsão do crescimento e risco de rutura do AA.

O objetivo deste estudo é determinar as propriedades mecânicas da parede da aorta, recorrendo a experiências de pressurização *in vitro* e a elastografia 2D por ultrassom (US), e investigar o desempenho da metodologia proposta sob condições fisiológicas.

Duas experiências de pressurização foram executadas em doze aortas de porco: 1) uma experiência 'estática', considerando um intervalo significativo de pressão (0 - 140 mmHg); 2) uma experiência 'dinâmica', simulando as condições hemodinâmicas presentes *in vivo* a pressões fisiológicas (70 – 130 mmHg). Para ambas as experiências, conjuntos de dados 2D de radiofrequência (RF) foram adquiridos para um plano de imagem longitudinal e duas secções transversais. Os dados de RF foram segmentados manualmente e um algoritmo 2D de monitorização do deslocamento da parede da artéria foi aplicado com o intuito de obter o diâmetro da aorta em função do tempo. O *shear modulus G* foi estimado assumindo um modelo de material Neo-Hookeneano. Além disso, um estudo 'incremental' baseado nos dados da experiência 'estática' foi realizado com o propósito de 1) investigar as mudanças nos valores de *G* no caso de aumento na pressão arterial média (PAM), para uma determinada diferença de pressão (30, 40, 50 e 60 mmHg); 2) comparar os resultados com os da experiência 'dinâmica', considerando o mesmo intervalo de pressão.

No caso da experiência 'estática', o valor de *G* resultante foi de 94 ± 16 kPa, o que está de acordo com a literatura. Foi observada uma dependência linear entre os valores de *G* e PAM, contudo o efeito da diferença da pressão revelou-se negligível. Os resultados da experiência 'dinâmica' revelaram um valor de *G* de 250 ± 20 kPa. Para o mesmo intervalo de pressão, o *shear modulus* incremental (G_{inc}) foi de 240 ± 39 kPa, estando em concordância com o anterior. No geral, para todas as experiências, não foram verificadas diferenças significativas nos valores de *G* entre os diferentes planos de imagem.

Este estudo demonstra que o método de elastografia 2D por US em aortas durante experiências de pressurização é viável sob circunstâncias controláveis e fisiológicas. Em estudos futuros, a experiência 'dinâmica' poderá ser repetida para um intervalo de PAMs e poderão ser analisadas artérias patológicas. Além disso, a utilização de modelos mais complexos necessita de ser considerada a fim de se obter uma descrição do comportamento não-linear do tecido vascular.

Key-words: aneurisma da aorta, biomecânica vascular, experiências de pressurização, elastografia 2D por ultrassom.

Contents

List of Figures

List of Tables

Acronyms

AA: Aortic aneurysm

AAA: Abdominal Aortic Aneurysm

BNC Connector: Bayonet Neill-Concelman Connector

CCF: Cross-Correlation Function

COPD: Chronic Obstructive Pulmonary Disease

CPU: Central Processing Unit

CT: Computed Tomography

CVD: Cardiovascular Disease

EVAR: Endovascular Repair

FEA: Finite Element Analysis

FOV: Field of View

GUI: Graphical User Interface

ILT: Intraluminal Thrombus

IVUS: Intravascular Ultrasound

MAP: Mean Arterial Pressure

MRI: Magnetic Resonance Imaging

PBS-solution: Phosphate Buffered Saline solution

RF: Radiofrequency

ROI: Region of Interest

SMC: Smooth Muscle Cells

SNR: Signal-to-Noise Ratio

US: Ultrasound

1. Introduction

1.1 Motivation

In this day and age, cardiovascular disease (CVD) is the leading cause of deaths worldwide. An estimated 17.3 million people died in 2008, representing 30% of all global deaths (Mendis et al., 2011). A sub-group of patients suffer from a thoracic, abdominal or even cerebral aneurysm.

In particular, an abdominal aortic aneurysm (AAA) is a permanent local dilatation of the aorta in the abdominal cavity of more than 50% of its original diameter (Zankl et al., 2007). The incidence of this condition is growing due to general aging of population and an increase in the amount of screening programs (Lederle et al., 1997), with approximately 150.000 new cases being diagnosed every year (Bengtsson et al., 1996). If left untreated, AAA will increase in size, until it eventually ruptures, causing a life-threatening hemorrhage. Of the patients with an AAA, 75% remain symptom free until AAA rupture occurs, which is fatal in most cases (Zankl et al., 2007). Annually, 15.000 to 20.000 deaths occur in the United States due to AAA rupture (Bush et al., 2003) and, as a result, remains the 13th most common cause of death in that country (Wilmink et al., 1998).

In order to determine if an AAA requires surgical intervention, the risk of rupture should be carefully assessed and balanced against the risk associated with the surgical repair. Currently, the decision to electively repair an AAA is based on the maximum anterior-posterior diameter of the aneurysm, i.e., when the maximum anterior-posterior diameter of the aneurysm is larger than 5-5.5 cm it is thought that the risk of rupture is high (Greenhalgh et al., 1998; Zankl et al., 2007). However, this criterion is regarded only as a general rule-of-thumb and is unreliable to predict

AAA rupture, since several studies have shown that small aneurysms, i.e., below 5.5 cm, can rupture (Choksy et al., 1999; Nicholls et al., 1998), while stable AAAs considered large, i.e., above 5.5 cm, do not rupture, given the life expectancy of the patient (Darling et al., 1977; Conway et al., 2001). Hence, intervention based on the maximum diameter criterion can be performed too late, prematurely or even subject patients to unnecessary surgical risks.

Besides maximum diameter, AAA growth rate can also be taken into consideration in the decision for AAA repair. Yet, previous studies have shown large variations in growth rate between AAAs and discontinuous growth was observed (Kurvers et al., 2004).

Both these criteria should be replaced by a more patient-specific criterion to better predict the likelihood of AAA rupture. In general, such a solution is sought for in the field of biomechanics. As a result, AAA wall stress analyses have been introduced (Raghavan et al., 2000; Fillinger et al. 2002). The basic principle of this approach is that when the stress in the AAA wall locally exceeds the strength of the wall, AAA rupture occurs. A thorough analysis on biomechanical properties of AAAs such as wall strength, elasticity or aortic compliance (Vorp et al., 1996; Imura et al., 1986; Long et al., 2004) can give a better understanding on AAA biomechanical behavior and, thus, a more accurate prediction of AAA growth and rupture. Elasticity can be assessed by destructive testing, but also non-invasively by means of ultrasound (US) elastography (Lopata et al., 2014).

This study intends to develop an accurate and reproducible method for the mechanical characterization of aortas by determining and analyzing biomechanical properties of the aortic wall, such as the shear modulus G, using *in vitro* inflation testing and 2D US elastography. The performance of this method was also investigated for physiological conditions. Ultimately, the goal is to provide a non-invasive tool based on *in vivo* US imaging and biomechanical patient-specific analysis, with the purpose of helping clinicians to detect and monitor weakening of the aortic wall, which may lead to an improvement of AAA growth prediction, and an optimization of both the follow-up plan and the moment of aortic surgical repair. In this sense, this approach may have the potential to serve as an accurate and robust method to improve AAA risk stratification.

1.2 State of the art

Current widespread clinical thinking is that AAA rupture is best predicted by monitoring its maximum diameter; i.e., it is conventionally accepted that the risk of rupture is highest when the maximum anterior-posterior AAA diameter reaches 5.5 cm (Greenhalgh et al., 1998). However, from previous research it becomes clear that the maximum AAA diameter in some cases underestimates the risk of rupture (Choksy et al., 1999; Nicholls et al., 1998), leading to unexpected ruptures, whereas in other cases the risk is overestimated (Darling et al., 1977; Conway et al., 2001). In the latter case, AAA may be unnecessarily repaired, with all associated surgical risks. Hence, additional indicators are required to provide a more accurate and robust assessment of AAA growth and rupture, based on a more patient-specific approach.

From a biomechanical perspective, rupture of AAA occurs when wall stress locally surpasses wall strength. The Law of Laplace states that wall stress in a thin-walled cylinder increases linearly with increasing diameter and transmural pressure, and decreases for increasing wall thickness. In this way, the Law of Laplace is regarded as the theoretical framework for using the "maximum diameter criterion" for potential AAA rupture prediction (Hall et al. 2000), since it states that the stress on the AAA wall is proportional to its diameter. However, the stresses acting on an AAA wall are not evenly distributed and are highly dependent on the shape (e.g. profile, tortuosity) of the specific AAA (Vorp et al., 1998).

Over the past two decades, several research groups have been suggesting patient-specific wall stress analyses as a potential predictor of AAA rupture, based on Finite Element Analysis (FEA) (Fillinger et al., 2002; Truijers et al., 2007; Raghavan et al., 2000; Speelman et al., 2010). Fillinger et al. (2002) found that the peak wall stress for ruptured and symptomatic AAAs was significantly higher than that for electively repaired AAAs. In another study conducted by this same group, it was shown that the peak wall stress is a better predictor of AAA rupture than the maximum AAA diameter (Fillinger et al., 2003). Likewise, a more recent study found similar results, showing a high correlation between the AAA rupture and the location of the peak wall stress (Venkatasubramaniam et al., 2004). Moreover, in a study of Speelman et al. (2010) it was observed that relatively low AAA wall stress is associated with lower AAA growth rate, but no significant correlation was found between absolute or relative wall stress analysis and AAA biomarker concentrations. In all aforementioned studies, patient-specific AAA geometries were obtained using FEA based on Computed Tomography (CT) data.

In order to monitor and assess AAA wall growth in a clinical environment, follow-up surveillance on a regular basis is required. In this sense, CT imaging is not adequate, considering the use of ionizing radiation and lack of patient-specific input apart from geometry. Alternatively, MRI (Magnetic Resonance Imaging) is often used to examine AAAs, owing its good image quality (Lee et al., 1984). One example is the study of Kramer et al. (2004) where T1 and T2-weighted spin echo imaging was performed in 23 AAA patients in order to detect atherosclerotic plaque components in AAAs. The study reports that higher signal on T2-weigthed MRI provides an accurate identification of the fibrous cap and thrombus within an AAA. Nonetheless, MRI is very time-consuming and expensive. Besides, contrast agents may be needed to enhance image quality and to acquire dynamic MRI scans.

Ultrasound (US) imaging combines its non-invasive nature, the absence of radiation hazard and its high temporal resolution. US imaging represents the modality of choice for AAA detection, initial assessment and follow-up surveillance, with a sensitivity of 95% and a specificity of almost 100% (Lindholt et al., 1999). The accuracy of size measurements using US is especially important to reliably monitor AAA growth. Singh et al. (1998) reported intra- and inter-observer variability in US measurements of AAA diameter less than 4 mm and concluded that the maximum AAA diameter could be measured using US imaging with a high degree of accuracy.

The high temporal resolution of US imaging enables a comprehensive study of the dynamical behavior of the aneurysm when exposed to blood pulse, providing an accurate assessment of patient-specific parameters, such as distensibility, tissue deformation (i.e., strain) or aortic compliance, which can be used to improve FEA or used as indicators of aneurysm growth. Several authors have used ultrasound to estimate the mechanical properties of AAA by tracking the dynamical change in diameter due to the passing blood pulse (Imura et al., 1986; Long et al., 2004; Wilson et al, 2003). The changing diameter is used to achieve a measure of strain. This approach provides information about the dilation of the aorta as function of time and space along the segment of the aorta. Imura et al. (1986) presented a method using B-mode US imaging for tracking the dynamic diameter of the abdominal aorta over the cardiac cycle in order to assess elastic properties of human abdominal aorta in vivo. Wilson et al. (1999) used US diameter tracking to report that large aneurysms tend to be stiffer than smaller, but found large variations for equally sized aneurysms. In a more recent study (Wilson et al., 2003), it was shown by means of an US scan-based diameter tracking technique that an increase in AAA distensibility over time is related to a significantly reduced time to AAA rupture.

In the aforementioned studies, distensibility was estimated by measuring the dynamical change in diameter over the cross-sectional area of the aneurysm only. However, several studies show that the biomechanical properties of the AAA wall vary heterogeneously over the wall (Thubrikar et al., 2001; Vallabhaneni et al., 2004). A method to measure displacements is to track the speckle patterns produced by microstructures present in different tissues, e.g. collagen fibers and blood cells, producing the so-called speckle pattern which can be seen in B-mode ultrasound images. This technique, commonly known as speckle tracking, was first introduced by Bohs and Trahey (1991) and has already been attempted for strain estimation of aortic aneurysms. One example is the study of Brekken et al. (2006), where speckle tracking was performed on 2D cross-sectional B-mode ultrasound image sequences to calculate strain in AAAs. In a more recent study (Jongen, 2011), the distensibility and E-modulus of both AAAs and aortas of healthy volunteers were determined using 2D ultrasound and RF-based wall tracking, with promising results. RF-based displacement tracking and subsequent strain estimation was introduced by Ophir et al. (1991). However, further studies are necessary to investigate the potential of this technique for improved assessment of AAA growth and rupture so that it can ultimately be introduced in a clinical environment.

1.3 Thesis Outline

This report is divided in six chapters. In this first chapter the motivation that led to the development of this thesis and the main objectives are presented, as well as the state of the art. Theoretical concepts are introduced in Chapter 2 providing the reader with the main subjects involved in this work. Chapter 3 gives insight on the preparation of the experimental setup, US acquisition and US-data processing. In addition, a detailed derivation of the material model used in this study is provided and the statistical tools used are described. In Chapter 4 the results are presented. A follow-up discussion is addressed in Chapter 5. Finally, Chapter 6 states the conclusions from this study and presents recommendations for future research.

2. Background Overview

2.1 Abdominal Aortic Aneurysms

The aorta is the largest artery in the human body, transporting oxygenized blood directly from the left ventricle of the heart to the rest of the body. The term *aneurysm* derives from the Greek *ανευρψσμα*, meaning widening.

An abdominal aortic aneurysm (AAA) is defined as a permanent and irreversible localized balloon-like dilation of the abdominal region of the aorta - between the renal arteries and the iliac bifurcation (Figure 2.1). Conventionally, in clinical practice, this disorder is diagnosed if the aortic diameter is 3 cm or more, which is about 1.5 times the expected normal diameter (Sakalihasan et al., 2005). The large majority of AAA (> 90%) originate below the renal arteries - infrarenal aneurysms (Zankl et al., 2007).

The incidence and detection of AAAs has increased during the past two decades mostly due to the introduction of screening programs and improved diagnostic tools. The estimated prevalence of AAAs in both men and women is age-dependent and varies between 1.3% and 8.9% in men and between 1.0% and 2.2% in women (Zankl et al., 2007; Wilmink et al., 1998). Risk factors associated with the development, expansion and rupture of AAA include advanced age, male sex, tobacco smoking, hypertension, chronic obstructive pulmonary disease (COPD), hyperlipidemia (abnormally elevated concentration of lipids and/or lipoproteins in the blood) and positive family history (Zankl et al., 2007; Golledge et al., 2006; Wilmink et al., 1998).

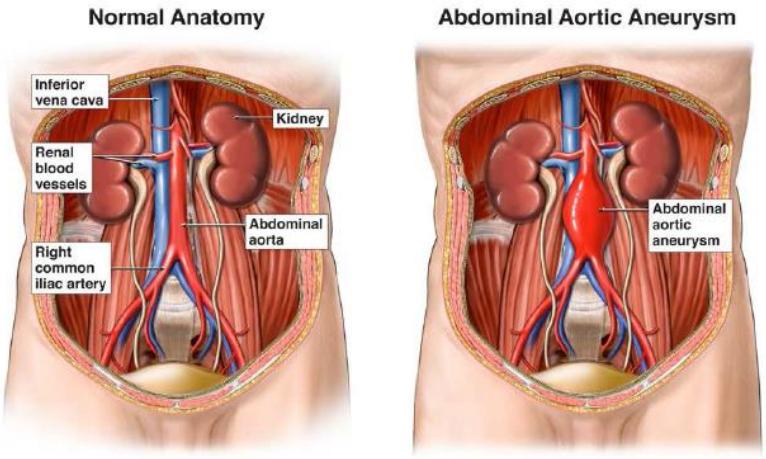

Figure 2.1 – Normal (healthy) aorta anatomy (left) and abdominal aortic aneurysm anatomy (right) (Speelman, 2009).

However, tobacco smoking is considered the most significant risk factor (Wilmink et al., 1999; MacSweeney et al., 1994; Brown et al., 1999). The prevalence of AAAs in tobacco smokers is more than four times larger than in lifelong non-smokers (Vardulaki et al., 2000). Production of nitric oxide by the endothelium, which mediates vasodilatation in response to altered hemodynamics, is reduced in both active and passive smokers (Barua et al., 2001). Thus, endothelial dysfunction caused by smoking can diminish the dilatory capacity of arteries, which leads to a stiffer wall.

In general, the risk of rupture increases as the diameter of the aneurysm enlarges (Brown et al., 1999). In some cases an AAA can lead to back pain, abdominal pain or a palpable pulsating mass in the abdomen. However, an AAA is most often asymptomatic until rupture of the AAA wall occurs, leading to a large abdominal hemorrhage and eventually death within a short period of time. The overall mortality rate for patients with ruptured AAAs is between 65% and 85% (Thompson et al., 1996). Moreover, about half of these patients die before they reach the surgical room (Scott et al., 1991).

Ultrasound imaging represents the modality of choice for the detection of AAA with a sensitivity of 95% and a specificity of almost 100% (Lindholt et al., 1999). US imaging can be used to accurately measure the diameter of the aorta in antero-posterior and transverse directions. This imaging technique is valuable for the initial assessment and follow-up surveillance, but also for population screening (Sakalihasan et al., 2005). An unruptured AAA can either be scheduled for follow-up surveillance or for elective repair. Figure 2.2 shows a proposed clinical management for asymptomatic AAAs.

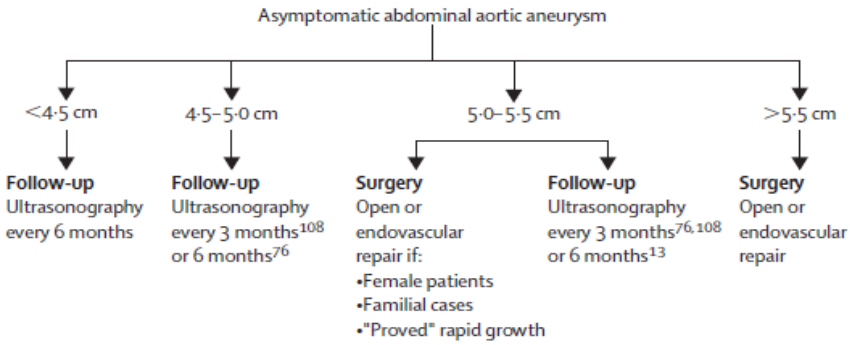

Figure 2.2 – Proposed size-dependent clinical management for asymptomatic abdominal aortic aneurysms (Sakalihasan et al., 2005).

2.1.1 AAA Clinical Management

In current clinical practice, the decision upon surgical intervention is based on the maximum anterior-posterior diameter of the AAA. Therefore, surgery is recommended when the diameter of the aneurysm is larger than 5.5 cm or when the aneurysm grows more than 1 cm per year (Zankl et al., 2007). However, clinicians analyze *a priori* if the risk associated with an AAA rupture exceeds the risks associated with a surgical intervention. If so, there are two possible treatment options: conventional open surgical repair or endovascular repair (EVAR). Both procedures exclude the aneurysm wall from the systemic pressure by means of a vascular graft.

In open surgical repair, a regular graft is sutured to healthy parts of the aorta by means of a transabdominal open surgery (Figure 2.3a). However, a retroperitoneal approach has been recommended in patients with COPD (Sakalihasan et al., 2005). This surgical procedure has been used for more than 50 years and is associated with a rate of graft failure as low as about 0.3% per year (Hallett et al., 1997).

On the other hand, endovascular repair - introduced by Parodi in 1991 (Parodi et al., 1991) - is a catheter-based procedure and therefore does not require an incision in the abdomen. Basically it consists of the insertion of a stent-graft via catheterization of the femoral artery (small incision in the groin) and placement of a stent-graft across the aneurysm (Figure 2.3b). For this reason, EVAR is less invasive than open surgical repair and is associated with a shorter recovery period. However, there are also downsides for the endovascular approach such as endoleaks or stent migration, which require open surgical treatment as a second step. In addition, there are several concomitant vascular conditions, such as significant occlusive disease of the renal, mesenteric and iliac arteries, which can preclude safe and effective endografting (Zankl et al., 2007).

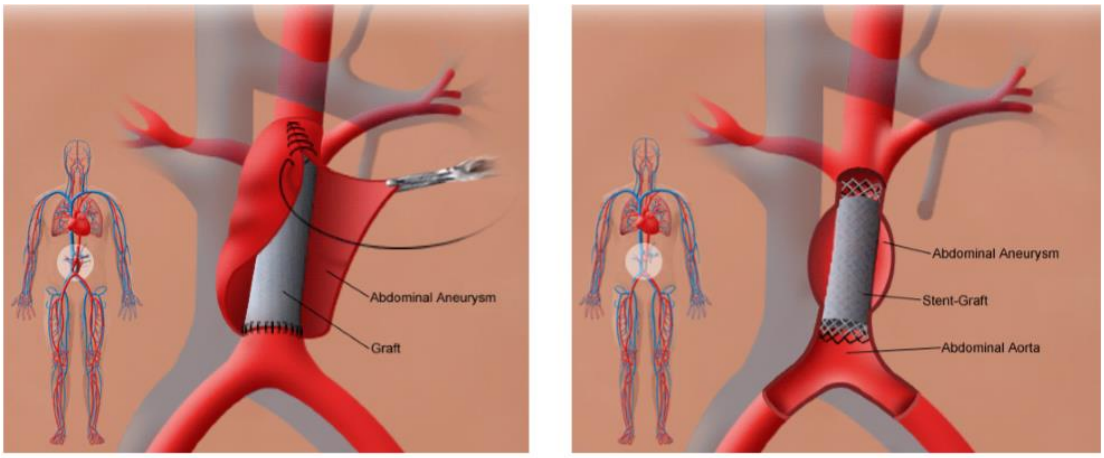

Figure 2.3 – AAA open surgical repair (a) and AAA endovascular repair (b) (Callanan et al., 2011).

Mean 30-day mortality rates for elective repair have been reported between 1.1% and 7.0% (Sakalihasan et al., 2005). Open surgical repair has a 30-day mortality rate of about 5%, whereas EVAR has a 30-day mortality rate of about 2% (Greenhalgh et al., 2004).

Yet, as far as emergency repair for ruptured AAAs is concerned, mortality depends on the hemodynamic status of the patient at the time of surgery. Operative mortality of ruptured AAAs has been reported as high as 30-70% (Kniemeyer et al., 2000). Overall, EVAR shows a lower operative mortality rate, shorter recovery time and less frequent complications than with open surgical repair (Greenhalgh et al., 2004; Prinssen et al., 2004).

2.1.2 AAA Pathogenesis

The function of the aorta is to distribute blood flow from the pulsating heart to smaller blood vessels that supply oxygenized blood to the tissue. Normal aortic function relies on the elasticity and strength of the aortic wall. The aortic wall consists of three layers (Figure 2.4). The most inner layer is the *tunica intima*, which is the thinnest layer, typically consisting of one single layer of endothelial cells. The *tunica media* is the middle and thickest layer, consisting of smooth muscle cells (SMCs), elastic fibers and collagen; the *tunica media* allows the aorta to expand and contract within each heartbeat. Finally, the *tunica adventitia* is the outer layer and comprises mostly connective tissue and the *vasa vasorum* (nurturing vessels of the arterial wall); the *tunica adventitia* provides additional structure and support to the aorta (Humphrey, 2002).

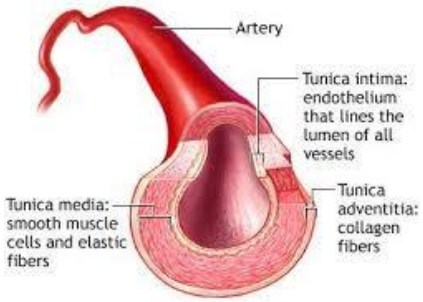

Figure 2.4 – The three layers of the arterial wall: the tunica intima, the tunica media and the tunica adventitia (A.D.A.M. Images ©. A.D.A.M., Inc. All rights reserved. www.adamimages.com).

The ability of the aortic wall to counter the force exerted by the intraluminal blood pressure is dependent on the structural proteins of the vessel wall. Elastin and collagen fibers are the main determinants of the mechanical properties of the aorta, acting to distribute stresses uniformly within the aortic tissue and maintain an appropriate viscoelastic response to the pulsatile oscillation (Wills et al., 1996).

Elastin fibers are mainly responsible for the compliance of the aorta, whereas collagen (types I and III) provide the tensile strength and structural integrity of the vascular wall. Elastin and collagen fibers are degraded by proteolytic enzymes mostly represented by matrix metalloproteinases (MMPs). MMPs derived from macrophages and SMCs, and are locally activated either by other MMPs, or by plasmin generated by plasminogen activators (Thompson et al., 1996). MMPs are significantly elevated in the wall of aortic aneurysms compared with healthy aortas (Longo et al., 2002).

The loss of elastin fibers is thought to be an initiating event in the development of AAA (Campa et al., 1987; Dobrin et al., 1994). The perpetuation of elastin degradation leads to AAA growth, until the time of rupture (Sakalihasan et al., 2005).

On the other hand, the loss of collagen seems to be the factor responsible for the rupture of the AAA (Dobrin et al., 1994). However, enhanced collagen turnover (increase in collagen concentration) has been reported in AAA in human beings (Satta et al., 1995), suggesting the existence of a compensatory response to the increased wall stress, as stretch is known to be a stimulus for connective tissue synthesis (Leung et al., 1976) thereby promoting wall thickening. Nonetheless, in the end, the balance between collagen synthesis and its degradation is in favor of degradation (Zankl et al., 2007), eventually leading to AAA rupture.

Likewise, the reduction of the concentration of SMCs in the *tunica media* of the aortic wall by apoptotic processes is also a histological feature which seems to play a crucial role in aneurysm development (Lopez-Candales et al., 1997). Besides, it has been reported that SMCs have a protective role against inflammation and proteolysis (Allaire et al., 2002).

Furthermore, the development of AAA is also associated with intraluminal thrombus (ILT) in most patients. In about 75% of all AAAs, thrombus is present (Harter et al., 1982). Thrombus is a fibrin structure with blood cells, platelets and blood proteins, which is deposited onto the vessel wall (Harter et al., 1982). Vorp et al. (2001) conducted a study to analyze the influence of ILT formation in AAA development. The study showed that ILT formation and its increasing thickness are found to be related to hypoxic conditions in the *tunica media* layer, thus inducing neovascularization and migration of inflammatory cells. Additionally, it has been suggested that ILT can originate proteolytic enzymes like MMPs, which have a key role in the pathogenesis of AAA formation (Fontaine et al., 2002).

2.2 Vascular Biomechanics

In Humphrey's book on vascular mechanics (2002), Biomechanics is defined as the development, extension and application of mechanics to answer questions of importance in biology and medicine. Through biomechanics one can address many of the physiological phenomena that occur at molecular, cellular, tissue, organ and organism levels. As a sub-discipline within biomechanics, vascular biomechanics can be described as the study of the vessel wall mechanical properties and their responses to blood pressure/flow (Raghavan et al., 2005).

In order to describe the mechanical behavior of the vessel wall, vessel compliance is often used (Imura et al., 1986; Long et al., 2004). The compliance of a blood vessel (C) is defined as the ratio of percentage change in vessel size to change in pressure, i.e., the ability of a blood vessel to 'store' blood as a result of a pressure change. Because one can define different measures of size (diameter, cross-sectional area, volume), several mathematical definitions exist. Yet, the general definition is:

$$C = \frac{\Delta V}{\Delta P} \tag{2.1}$$

where ΔV is the change in volume due to change in blood pressure, ΔP.

Compliance is not an intrinsic property of the vascular tissue, since it can be affected to some extent by size (e.g. compliance of a small-diameter vessel will be higher than that of a large diameter). Hence, the compliance is not suitable to compare vessels with different size. On the other hand, distensibility (*D*) is defined as the compliance divided by the resting (diastolic) volume. This normalized measure of compliance with respect to the initial volume is often used to assess the mechanical behavior of the aortic wall (Wilson et al., 2003) and can be used to compare vessels with different sizes. Distensibility can be defined as:

$$D = \frac{C}{V_d} = \frac{\Delta V}{\Delta P}\frac{1}{V_d} \tag{2.2}$$

where ΔV is the change in volume, ΔP the change in pressure and V_d the diastolic volume.

2.2.1 Mechanical behavior of the arterial wall

The arterial wall mechanics and its interaction with blood flow have been an object of extensive research during the past decades. The first study describing the mechanical behavior of the arterial wall was conducted by Roach & Burton (1959) on human iliac arteries. In addition, Cox (1978, 1979) and Dobrin (1978) performed studies on dogs, rabbits and rats. From these studies, the non-linear behavior of the arterial wall was comprehensively demonstrated. Besides, Patel et al. (1969) were the first who reported upon the anisotropy of the arterial tissue, suggesting that the arterial wall is cylindrically orthotropic, (i.e., arteries exhibit different material properties or strengths in different orthogonal directions), which is generally accepted in the literature. The common assumption of incompressibility was first suggested by Carew et al. (1968), who concluded that changes in volume were very small even for deformations greater than those *in vivo*.

In addition, it has been shown that blood vessels exhibit a non-linear viscoelastic relation between stress and strain (Fung, 1993). This property has been associated with the histological structure of the vascular tissue, specifically the contents of elastin and collagen fibers (Hofzapfel et al., 2000). When the arterial wall is subjected to a certain load, elastin dominates the response at lower pressure levels - causing the elastic recoil of the artery - and collagen gradually starts contributing as the loading increases (Sumner et al., 1970; Kleinstreuer et al., 2007). The collagen-elastin ratio has been reported to be the key determinant of aortic wall mechanics (Holzapfel et al., 2000). A typical stress-strain curve for the aorta is shown in Figure 2.5 along with elastin and collagen curves.

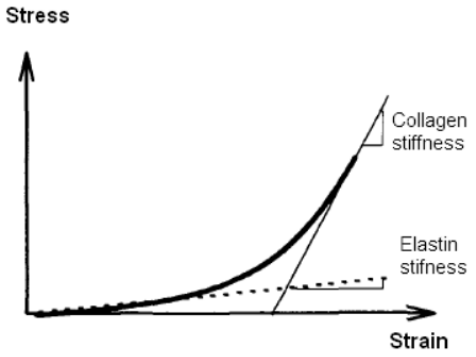

Figure 2.5 – Stress-strain curve for the aorta and the elastin and collagen curves (Raghavan et al., 1996).

The intraluminal blood pressure in the aorta leads to the following components of stress: *Hoop* stress or circumferential stress, radial stress and longitudinal stress. *Hoop* stress is thought to be critical in aortic dissection eventually followed by rupture, and radial stress can be of interest when intraluminal thrombus is present. On the other hand, the stress in the longitudinal (axial) direction is barely influenced by the pulsating blood pressure (Raghavan et al., 2005). These stress components acting on the wall lead to an anisotropic mechanical behavior of the aortic tissue (Thubrikar et al., 2001) and yield strain components in the respective directions (Figure 2.6).

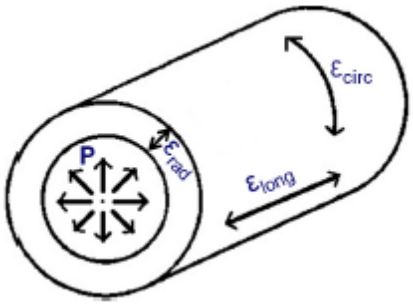

Figure 2.6 – Schematic view of the aorta. The pulsating blood pressure yields strains in the circumferential (ε_{circ}), radial (ε_{rad}) and longitudinal (ε_{long}) directions (Peters, 2013).

Over the last decades, mechanical properties of AAAs have been examined by *in vitro* tensile testing (He et al., 1994; Raghavan et al., 1996; Xiong et al., 2008). Biomechanical analysis by means of tensile testing can provide an important insight into the mechanical behavior of aortic tissue, particularly in understanding the formation, growth and rupture of AAAs. For instance, He et al. (1994) conducted uniaxial tensile tests on aneurysmal tissue as well as on non-aneurysmal controls. AAAs were found to be less distensible and stiffer than non-aneurysmal

aortas. Besides, it was shown that elastin and SMC were reduced by 89% and 90%, respectively, and collagen content is increased by 74% in AAAs compared to healthy aortas (Table 2.1). In short, in AAAs, collagen synthesis is increased and elastin degradation is enhanced, leading to stiffer vessels (Wills et al., 1996).

Table 2.1 – Composition of normal (healthy) aortic tissue and AAAs (He et al., 1994).

	Normal aorta (%)	Aneurysm (%)
Elastin		
Average	22.7	2.4
Maximum	32.5	6.7
Minimum	16.1	0.2
Muscle		
Average	22.6	2.2
Maximum	33.6	6.4
Minimum	15.5	0.4
Collagen and ground substances		
Average	54.8	95.5
Maximum	63	98
Minimum	48	91.4

Since the aortic tissue is loaded in multiple directions *in vivo*, uniaxial tensile testing may be inadequate for a complete characterization of its mechanical response. Thus, biaxial tensile testing allows for a more suitable modelling of the aortic tissue. Vande Geest et al. (2006) reported a population-wide study on the mechanical behavior of human healthy abdominal aortic tissue and AAA tissue using the well-validated biaxial tensile testing system proposed by Sacks (2000). As expected, both tissues exhibited an anisotropic behavior. Additionally, it has been shown that healthy abdominal aortic tissue is more distensible than AAA tissue.

2.2.2 Vascular modelling

In order to analyze the mechanical behavior of the arterial wall a theoretical framework is required. Hence, an overview of the main constitutive mechanical models will be addressed.

The simplest mechanical model of a linearly elastic solid is a spring. The Hooke's Law states that the force F to extend or compress a spring by some distance ΔL is proportional to that distance:

$$F = k\Delta L \tag{2.3}$$

where k is a constant.

If an elastic body requires a larger force to achieve a certain deformation, it is stiffer or less compliant. Stress (σ) can be defined as force per unit of cross-sectional area (F/A), whereas strain (ε) can be described as the fractional increase in length, that is, $\Delta L/L_0$ or $(L-L_0)/L_0$; L and L_0 being the final and initial length, respectively. Therefore, an equation analogous to the Hooke's Law describes the relationship between stress and strain:

$$\sigma = E\varepsilon \Leftrightarrow \frac{F}{A} = E\frac{\Delta L}{L_0} \tag{2.4}$$

where E represents the Young's modulus.

According to the Hooke's Law, stress and strain should have a linear relationship. Besides, the Hooke's Law assumes that the material is homogeneous and isotropic. However, the arterial wall is not homogeneous since it is composed out of various elements such as elastin, collagen fibers and SMCs (Holzapfel et al., 2000), which are not arranged in the arterial wall as simple linear springs. In addition, it is commonly accepted that the arterial wall is anisotropic (Patel et al., 1969; Thubrikar et al., 2001). Furthermore, the Hooke's Law is only valid for small deformations, which is not the case of the vascular tissue (Fung, 1993).

The neo-Hookean model is a hyperelastic material model which can be used for predicting stress-strain behavior of materials undergoing large deformations. However, this model also assumes linear elastic, isotropic behavior and incompressibility of the tissue. The neo-Hookean model was proposed by Rivlin (1948) and is based on the statistical thermodynamics of cross-linked polymer chains (Kim et al., 2012). The stress-state for a Neo-Hookean material can be described as follows:

$$\sigma = -p\boldsymbol{I} + G(\boldsymbol{B} - \boldsymbol{I}) \tag{2.5}$$

with σ the Cauchy stress tensor, p the hydrostatic pressure, $\boldsymbol{I}$ the identity matrix, G the shear modulus and $\boldsymbol{B}$ the left Cauchy-Green deformation tensor.

Strain energy density function is often used to characterize the constitutive material models. It relates the strain energy density of a material to its deformation gradient. For incompressible materials the respective strain energy density function of the Neo-Hookean model is described as (Kim et al., 2012):

$$W = c_{10}(I_1 - 3) \tag{2.6}$$

where c_{10} is a specific material parameter and I_1 the first invariant of the left Cauchy-Green deformation tensor.

Furthermore, Raghavan et al. (2000) proposed a non-linear biomechanical model based on the generalized Neo-Hookean model, and developed specifically to estimate wall stress distribution within the AAA wall. The AAA tissue was modeled as hyperelastic, homogeneous, isotropic and incompressible. The strain energy density function was derived from mechanical testing data of AAA tissue and was defined as:

$$W = c_{10}(I_1 - 3) + c_{20}(I_1 - 3)^2 \tag{2.7}$$

where α and β represent specific material properties of the AAA wall, estimated experimentally; and I_B is the first invariant of the left Cauchy-Green deformation tensor.

In a study analyzing the mechanical behavior of rabbit carotid arteries and taking into account the anisotropy of the arterial tissue, Fung et al. (1979) proposed the following exponential strain energy density function:

$$W = \frac{c}{2}(e^Q - 1) \quad \text{where } Q = A_{ijkl}E_{ij}E_{kl} \tag{2.8}$$

where E_{ij} and E_{kl} are components of the Green strain tensor and c and A_{ijkl} are specific material parameters in tensor notation.

Fung's model can describe the behavior of several soft tissues especially the highly non-linear stiffening observed at higher strains (Humphrey, 2002).

Over the last years, other hyperelastic material models, which incorporate also fiber orientation, have been proposed for studying mechanical behavior of arteries (Holzapfel et al., 2002; van den Broek et al., 2011).

Hence, before choosing and applying a material model, a thorough assessment and comparison of all these models is required, in order to identify which model leads to the most feasible results.

2.3 Ultrasound

Ultrasound imaging or echography is commonly used worldwide in clinical routine as a diagnostic imaging technique since the 50s. The first reported use of reflected US waves as a medical diagnostic tool was by an Austrian neurologist, Dr. Karl Theodore Dussik, who publicly presented his work on diagnosis of brain tumors using ultrasound in 1948 (Edler et al., 2004). In 1953, Drs. Inge Edler and Carl Hellmuth Hertz used ultrasound for the diagnostic evaluation of mitral

regurgitation, which is known as the first reported attainment of the use of ultrasound as a cardiac diagnostic tool (Lawrence, 2007).

Besides its bedside applicability and relatively low costs, echography combines its non-invasive nature with the absence of radiation hazard and its high temporal resolution, being a practical, safe and real time imaging technique and therefore a modality of choice for cardiac applications (echocardiography) and fetal imaging. Nevertheless, ultrasound can also be used to obtain images of liver, kidneys, muscles, thyroid, breast, brain and blood vessels (Lopata, 2010).

2.3.1 Physics and Instrumentation of Ultrasound

Sound waves are mechanical longitudinal waves, which can be described in terms of particle displacement or pressure changes (Aldrich, 2007). In fact, sound waves can be regarded as mechanical impulses of kinetic energy (vibrations) which propagate through a medium by alternating between two states: compression and rarefaction (Lawrence, 2007). In general, ultrasound corresponds to sound waves with a frequency that exceeds the range of the human hearing (> 20 kHz). Typically, medical US devices use frequencies between 1-20 MHz.

An ultrasound machine consists of a transducer, a central processing unit (CPU) connected to a display (monitor), keyboard and printer. The US transducer (US probe) contains piezoelectric crystals interconnected electronically, which vibrate when charged with an alternating current - the so-called Piezoelectric effect (Weyman, 1994). Each piezoelectric crystal vibrates at a characteristic frequency. These vibrations induce the piezoelectric crystals to send a short burst of acoustic waves into its surroundings. Repeated pulses of US will therefore generate an US beam. At the same time, the transducer act as a receiver and waits for the reflected acoustic waves to return (Figure 2.8). The reflected acoustic waves are recorded by the same piezoelectric crystals, which have the ability to transform the US pulse back into an electrical voltage.

The received signals are sampled at time t after the transmission of the pulse. The relation between the time t for sampling a scan-line of depth d is:

$$t = \frac{2d}{c} \tag{2.9}$$

where c is the speed of sound, and the factor 2 accounts for the two-way distance the pulse propagates, i.e., forward and backward.

Every tissue in the human body has its own characteristic acoustic impedance *Z*, which is defined as:

$$Z = \rho . c \tag{2.10}$$

where ρ represents the tissue mass density (kg/m^3) ; c is the speed-of-sound (approximately 1540 m/s in soft tissue).

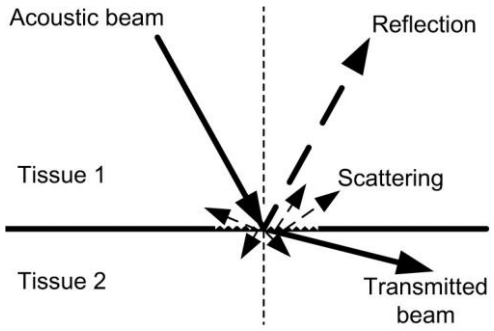

Figure 2.7 - Schematic representation of the reflection and scattering of acoustic waves in tissue (Lopata, 2010).

The acoustic impedance represents the capacity of a tissue to transmit sound. Denser materials such as muscle and blood transmit sound better than air and lungs (Hendee & Ritenour, 2002). Moreover, if the acoustic impedance differs from one tissue to another, the US beam will be partially reflected. However, if this difference is too large, almost total reflection will occur, which is the case in the lungs and the skull (Lopata, 2010). In general, the greater the difference in acoustic impedance between tissues (or greater difference in tissues mass densities), the greater the amount of reflected US waves. This larger amount of reflected sound waves is observed as brighter edges in the US image.

Besides, if the US beam encounters small or irregularly shaped structures that are much smaller than the wavelength of the US waves, such as blood cells and collagen fibers, scattering occurs. These micro-structures that are present in most tissues will act as scattering sources reflecting the US waves in random directions, yielding interference patterns, the so-called speckle patterns, which can be seen in 2D US images as small white blobs. These speckle patterns are somewhat consistent for each type of tissue. Nevertheless, the majority of these scattered waves will be absorbed by the tissue and eventually transformed into heat, as they are not aligned with the ultrasound transducer.

Besides the aforementioned effects, US waves can also be attenuated when passing through different tissues. Attenuation is dependent on the mass density of the tissue, the depth and the frequency of the US wave. Higher frequencies (shorter wavelengths) have the most difficulty penetrating the tissues of the body, since they are more attenuated than lower frequencies (longer wavelengths). Thus, greater penetration depths require US waves with a lower frequency, but at the cost of a poorer resolution (Lawrence, 2007).

Once the US information is generated and transmitted to the US machine, it is processed and displayed visually to provide the clinician with the required information. It should be noted that when the transducer receives the US signals, it acquires the so-called raw US data, or radiofrequency data (RF-data) (Lawrence, 2007). There are different types of US acquisition modes (Figure 2.8). In A-Mode (Amplitude Mode), a single US echo measurement produces a one-dimensional map of the positions of the reflecting waves along the direction of the transmitted US beam, i.e., the amplitude of one echo line is displayed versus depth. Next, in B-Mode (Brightness Mode), the amplitude of the received signals is represented with pixels of varying intensity, displaying a group of neighboring imaging lines as grey scale image. With the use of a multi-element transducer, this acquisition mode creates a two-dimensional (2D) image of the tissue. Finally, the time-series of a single A-line in brightness mode can be used to visualize motion of the tissue, which is known as M-Mode (Motion Mode). In general, an M-scan consists of repeated A-Scans along a single direction intersecting a moving tissue, such as a heart valve (Guy et al., 2005).

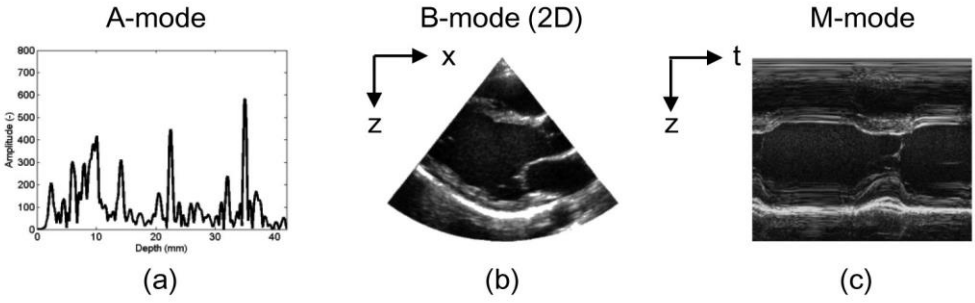

Figure 2.8 - Some of the different types of US acquisition modes: (a) A-mode, a single echo line; (b) B-mode, an image created by several neighboring echo lines; (c) M-mode, time-series of a single echo line (Lopata, 2010).

The quality of the US image plays a crucial role in clinical routine, helping physicians to make a correct and accurate diagnosis. Therefore, there are some aspects which can affect the quality of the US image, such as resolution, contrast and signal-to-noise ratio (SNR) of the US system.

The spatial resolution of US images depends both on the transducer used (transducer configuration) and the US frequency. In 2D US images, spatial resolution includes axial and lateral resolution.

Axial resolution corresponds to the ability of distinguish structures along the axis of the US beam; it can be defined as the length of the transmitted pulse. Typically, the pulse is two or four wavelengths long. Furthermore, a large bandwidth is favored in US acquisition to create a short ultrasound pulse, and hence to yield a higher spatial resolution (Lopata, 2010).

On the other hand, lateral resolution involves the resolution of structures that lie horizontally to the axis of the US beam, i.e., perpendicular to the US beam. Lateral resolution depends on the transducer pitch, i.e., distance between the centers of two adjacent piezoelectric crystals, the depth of the US focus, the width of the US beam and the transducer configuration (Hendee & Ritenour, 2002). Additionally, it should be noted that a higher frequency yields a higher lateral resolution. However, attenuation increases for higher frequencies and hereafter reduces penetration depth. Thus, taking this into account, low frequency transducers (1-5 MHz) are commonly used for imaging deep-laying structures, such as the heart or the aorta (Lopata, 2010).

Moreover, US is also known for its excellent temporal resolution, which makes it an appropriate imaging tool for tissue motion and strain estimation. Temporal resolution of US data depends on the cycles of transmitted and received signals, i.e., pulse repetition rate, as well as on the depth of the image (Lawrence, 2007).

There is a wide range of transducers that are commonly used in US imaging. Each transducer has its own distinctive configuration characteristics and its specific purpose. Single-element transducers have only one piezoelectric crystal to transmit and receive US waves and, as a result, only one echo line can be imaged. Actually, a semi-2D image can be obtained by means of physical motion of a single-element transducer, i.e., sweeping, which can be performed either manually or automatically with the aid of a specific mechanical system, commonly referred to as *mechanical sector scanning* (Hendee & Ritenour, 2002).

Alternatively, the US beam may be swept back and forth without the need of any mechanical motion, using transducer arrays. Transducer arrays are composed by several piezoelectric crystals, which can change the direction or degree of focus of the ultrasound beam by timing the excitation

of the crystals (Hendee & Ritenour, 2002). Linear-array, phased-array and curved-array transducers are examples of transducer arrays regularly used in clinical practice, which enable imaging of sector scans. A general overview of the aforementioned types of transducers is presented below.

The linear-array transducer (Figure 2.9a) is composed by a series of piezoelectric crystals disposed in a line and wired together. Generally, one linear-array transducer can contain about 128 to 256 piezoelectric crystals, which are excited by voltage pulses in sub-groups of 3 up to 20 or more. When the signal is received, the active sub-group will be shifted in position over one element. Then, the following procedure of signal transmission and reception can begin. Each excitation of the crystal group yields one "scan line". In this sense, a reasonable number of scan lines can be acquired, creating the illusion of motion by displaying a sequence of still pictures (Lawrence, 2007). The lateral resolution of the linear-array transducer is mostly dependent on the distance of the piezoelectric elements in the transducer, the so-called 'pitch' (typically 100-400 μm). Moreover, by activating the elements of a sub-group taking into consideration the respective time delays, it is possible to achieve beam focusing within the scan plane (Lopata, 2010).

Another method often used to acquire sector scans is the *phased-array technology*. A phased-array transducer (Figure 2.9b) uses all (typically 128) its elements to obtain each scan line. By wisely using time delays between excitations of the elements, it is possible to focus and steer the US beam over a range of different directions, leading to a sector scan image with an opening angle of 5 – 90º (Hendee & Ritenour, 2002). Since it has a relatively small footprint (area of the US probe that contacts with the patient), the phased-array transducer is normally used for imaging the heart, when positioned between the ribs (Lopata, 2010).

Finally, a curved-array transducer (Figure 2.9c) is similar to a linear-array transducer, apart from the fact that its surface shape is curved. This specific type of transducer enables sector scanning acquisition in a polar coordinate system. The advantage of curved-array transducers is the large field-of-view (FOV) at great depth, which allows imaging of large structures in the abdomen (Jongen, 2011). Nevertheless, the lateral resolution of a curved array transducer is dependent on depth, since at the top of the image the distance between neighboring scan lines is smaller in comparison to those at the bottom of the image (Aldrich, 2007). In particular, for aorta and AAA imaging a curved-array is more adequate, since the use of this type of transducer leads to the largest filed-of-view (Hansen et al., 2008).

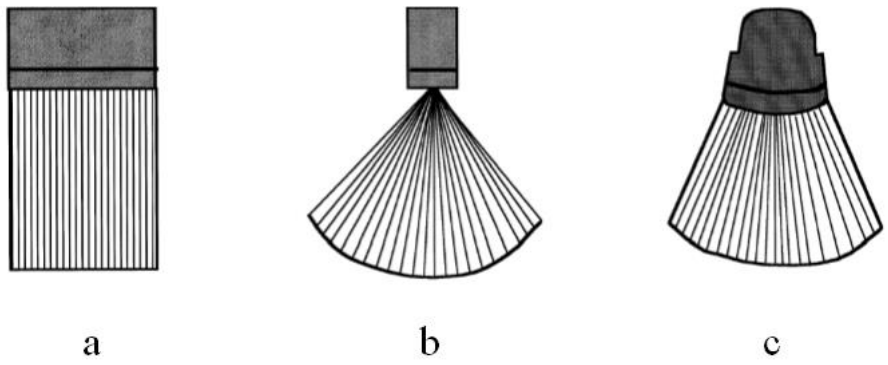

Figure 2.9 – Types of US transducers: linear-array transducer (a), phased-array transducer (b), curved-array transducer (c).

3.3.2 Ultrasound Strain Imaging and Elastography

Strain is a quantitative measure that expresses the relative elongation (expansion) and compression (shortening) of structures due to an internal or external force. In particular, the aortic wall is subjected to an internal mechanical load, the intraluminal blood pressure. Therefore, motion and strain can be considered as the vessel's response to the intraluminal blood pressure (Brekken et al., 2006). Taking into consideration its high temporal resolution, US can be used for motion tracking and strain estimation.

In the early nineties, Ophir et al. (1991) were the first researchers reporting on RF-based strain imaging. In that study, one-dimensional (1D) segments of RF-data were cross-correlated with segments of RF-data of the following time frame, in a window-by-window processing scheme. Template matching was performed using pre-compression and post-compression RF-data. Next, the cross-correlation peak of the RF-data windows was detected and, as a result, the axial displacement, i.e., the displacement along the ultrasound beam, was obtained (Figure 2.10). Furthermore, in order to obtain the strain data, the first-order spatial derivative of the axial displacements was calculated (Ophir et al., 1991; Lopata, 2010).

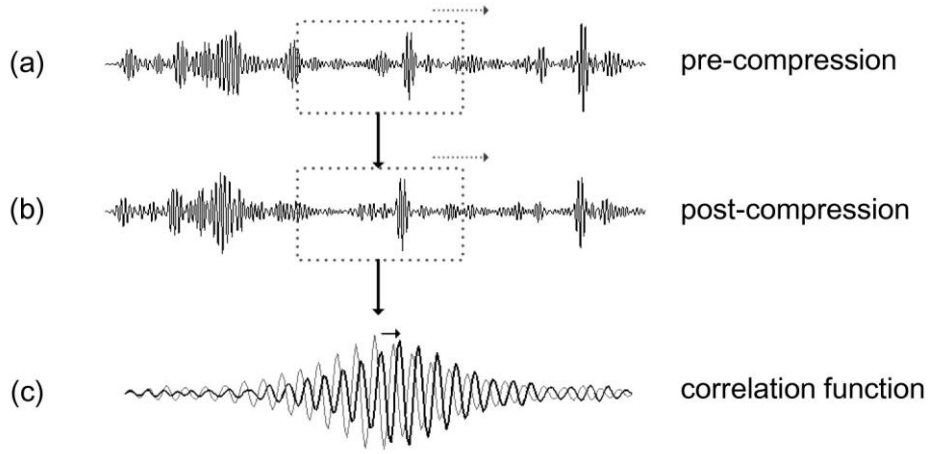

Figure 2.10 – A single RF-line of a time frame *i* (a) and the RF-line of the next time frame *i+1* (b). c) The light grey line represents the auto-correlation of RF-line (a) and the black line corresponds to the cross-correlation of RF-lines (a) and (b). The shift of the cross-correlation function with respect to the auto-correlation function illustrated in the figure corresponds to the displacement of the tissue (Lopata, 2010).

After Ophir's 1991-paper, several studies were reported in regards to applications of RF-based strain imaging. For instance, in a study of Emelianov et al. (1995), an *in vivo* application of this technique was shown in kidney, with promising results in the early detection of renal pathology. RF-based strain imaging has also been observed in tumor (Ophir et al., 1999), breast (Krouskop et. Al, 1998) and prostate (Khaled et al., 2006). In the aforementioned studies, the different tissues were compressed with the aid of an external device, commonly referred to as 'quasi-static' approach.

Alternatively, in the late nineties and beyond, RF-based strain imaging has been applied in dynamic studies, where a physiological deformation source induces tissue strain (Heimdal et al. 1998; de Korte et al. 2000; Kim et al. 2004).

RF-based strain imaging uses both phase and amplitude information. By using one-dimensional (1D) strain imaging techniques, only strains in the axial direction can be estimated. However, tissue motion and deformation are not limited to a single dimension. Most tissues exhibit anisotropic, incompressible and viscoelastic behavior (Thubrikar et al., 2001). Hence, the necessity for 2D and even 3D displacement and strain estimation methods is clearly evident (Lopata, 2008).

Two-dimensional (2D) strain imaging was first reported in a study of Heimdal et al. (1998), who introduced Tissue Doppler Imaging (TDI) based strain rate imaging. This method enabled semi-real time strain rate and derived strain imaging. Nevertheless, the main disadvantage of this

approach was the angle dependency. Moreover, the use of 2D windows is required in two-dimensional strain estimation. However, this is not easy to obtain, since RF-data contains phase information in the axial direction but not in the lateral direction, resulting in a lower accuracy for lateral strain estimates (Lopata et al., 2009). Konofagou et al. (1998) introduced an accurate lateral displacement tracking method using 1D RF-data windows by means of performing weighted linear interpolation of the post-compression RF-lines before tracking the RF-data in the lateral direction. In a more recent study (Lopata, 2010), 2D pre- and post-compression data windows were used to find the maximum cross-correlation, providing correct sub-sample axial and lateral displacement estimates by means of 2D parabolic interpolation. Furthermore, this technique was also applied in 3D strain estimation with promising results (Crosby et al., 2008; Lopata et al., 2011).

Another method commonly used to measure displacements is 2D speckle tracking. This technique was first introduced by Bohs and Trahey (1991) who used conventional B-mode images, i.e., amplitude information only, to track tissue motion and measure displacements. This speckle tracking method yielded 2D deformation at relatively low frame rates and was angle independent. A 2D segment with its characteristic speckle pattern is defined in one time frame and is matched with the speckle patterns within a search area in the following time frame, in a block-matching scheme (Figure 2.11). In a study of Golemati et al. (2003), wall motion of the carotid artery has been analyzed performing 2D speckle tracking, in a block-matching scheme, to obtain radial and longitudinal displacements.

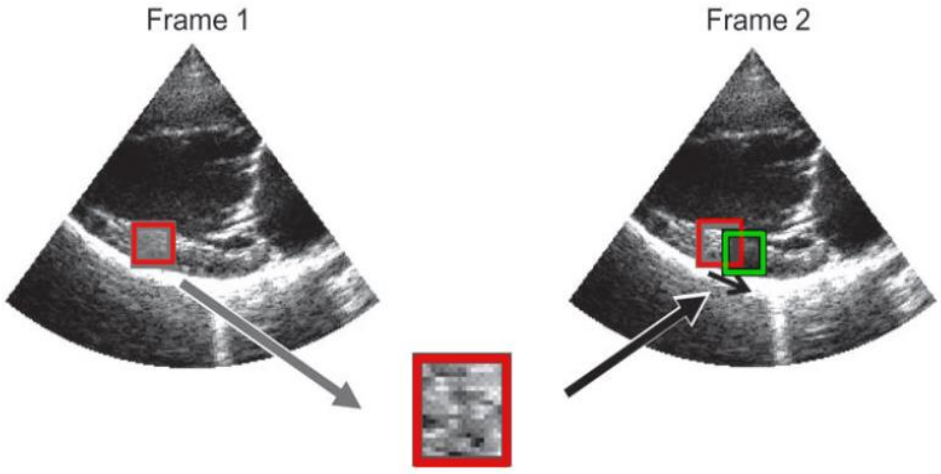

Figure 2.11 – Schematic representation of 2D B-mode speckle tracking. A small segment of image in time frame 1 (red square) is matched with a search area (green square) in the next time frame 2. (Lopata, 2010).

On the whole, the benefit on using RF-data lies in the high resolution - since there is phase information - therefore enabling accurate measurement of diameter-wave forms and local strains in the vessel wall, whereas B-mode speckle tracking is feasible to estimate more global strains in the wall (Lopata et al., 2014).

However, strain profiles are affected by the degree of initial compression and by the interdependence among different tissue components, whose elastic properties are generally unknown.

The Young's modulus, as an intrinsic tissue property, provides quantitative information about tissue elasticity and is therefore a more reliable parameter than strain (Ophir et al., 1991). As a result, with this study, Ophir and colleagues (1991) developed an imaging technique called Elastography. Assuming an uniform stress distribution, by means of controlling compression of the *in vitro* tissue in a 'quasi-static' approach, Ophir et al. (1991) obtained a direct estimation of the Young's modulus, yielding a set of images commonly known as 'elastograms'.

In contrast to US strain imaging, US elastography aims at the identification of different tissue constituents and measurement of soft tissue elastic properties, rather than assessing an instantaneous parameter, such as strain or incremental moduli that depend on the pressure range present during measurements (Lopata et al., 2014). US elastography, as a form of elasticity imaging is usually described as "virtual palpation" (DeWall, 2013), providing an effective assessment on different pathologies, since tissue mechanical changes often correlate with tissue pathological changes (Fung, 1993).

Moreover, numerous applications have been reported using this technique. For instance, intravascular ultrasound (IVUS) catheters were used *in vitro* and *in vivo* on coronary arteries to perform US elastography by use of raw RF-data, providing a valuable tool in the detection of vulnerable plaques in coronary arteries (de Korte et al., 2002). The advantages of IVUS are the high spatial resolution and the availability of RF-data that somehow aligns with the radial directions in the vessel wall, whereas its drawback is the invasive nature and the one-dimensional (1D) assessment of strain (Lopata et al., 2014).

Over the last years, a new technique has come into play: shear wave US elastography. This imaging method is based on the combination of a radiation force induced in a tissue by an ultrasonic beam and an ultrafast imaging sequence capable of catching in real time the propagation of the resulting shear waves (Bercoff et al., 2004). One example is the study of Evans et al. (2010), where the reproducibility of shear wave US elastography was assessed and compared

with greyscale ultrasound for benign/malignant breast tumor classification. This study showed promising results and the authors suggest that shear wave US elastography can be an accurate diagnostic tool for breast lesions.

3. Methods

3.1 Sample Preparation

Porcine aortas were tested in a controlled experimental setup to obtain US data and pressure data of the aortic wall. The porcine tissue was obtained from a local slaughterhouse and comprised a large part of the aortic segment and the complete heart still attached. The pigs were between 5 and 7 months of age and had a body weight between 100 kg and 120 kg. Right after the excision at the slaughterhouse, the porcine tissue was stored in phosphate buffered saline solution (PBS-solution) and transported to the laboratory. All aortas were dissected from the heart as close to the aortic valve as possible. Next, excess of connective and fat tissue was removed from the aortas. Each aorta was stored in a plastic sample bag with some PBS-solution to keep the tissue moist. Finally, the aortas were placed in the freezer at -20°C. In all, 12 porcine aortas (one per day) were tested in the experimental setup.

At the day of the experiment, firstly the aorta was defrosted by placing the plastic sample bag in a container filled with water at room temperature, for about twenty minutes. Next, all remaining connective and fat tissue was removed from the outer layer of the aorta. From time to time, the aorta was rinsed with fresh PBS-solution to keep it moist. For proper inflation of the tissue, the aortic side branches had to be closed. This was done by tying the side branches with thread (Figure 3.1). Finally, the aorta was attached to connectors at both ends using tie wraps. A leakage test was then performed to check whether the side branches were correctly closed and to detect other possible leakage sites (Figure 3.2). If so, superglue was added to completely close the side branches and possible openings within the aortic segment.

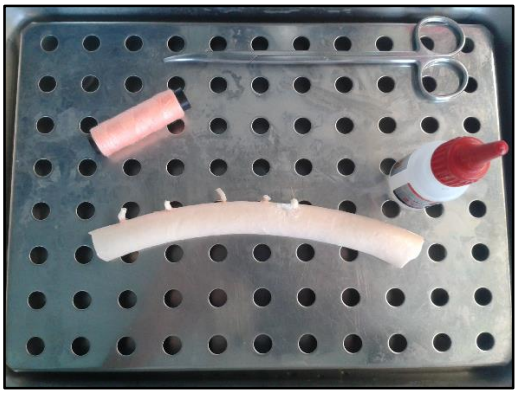

Figure 3.1 – A defrosted aorta with closed side-branches. Side branches were closed with thread. In the case the side branch was too short to close with thread, superglue was used to close the side branch.

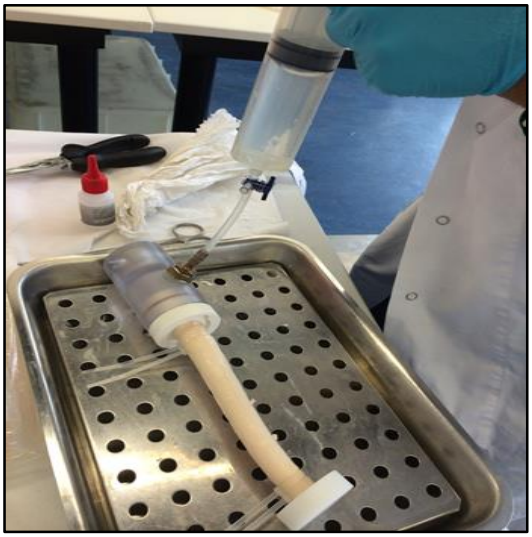

Figure 3.2 – The leakage test. First, the aorta was closed at the distal end and connected to a syringe at the proximal end. Next, the aortic segment was inflated by adding water via the syringe so that any possible leakages could then become visible. The leakages were marked using a marker pen. Finally, these leakages were closed using superglue. This procedure was repeated until there were no leakages left.

3.2 Experimental Setup

The experimental setup comprises a water tank, a circular water compartment, an axial piston pump, two mechanical valves and a vertical air column with two associated resistances (see Figure 3.3). The axial piston pump is connected to the circular water compartment and is used to inflate and deflate the aorta. When the axial piston pump moves forward, i.e., to the right (systole), the water flows from that circular compartment, passing a mechanical valve towards the aorta, which is placed inside the water tank. This leads to the inflation of the aortic segment. The mechanical valve resembles the function of an aortic valve since it enables a unidirectional flux of water from the circular compartment to the aortic segment. Similarly, the circular water compartment can be regarded as the left ventricle as it is where the water (arterial blood) is stored before the systole occurs. Moreover, when the axial piston pump moves backwards, i.e., to the left, the water flows in the opposite direction, i.e., from the water tank back to the circular compartment, leading to the deflation of the aorta. For this purpose, another mechanical valve – placed inside the water tank and connected to the circular water compartment – is used in this experimental setup allowing for the inflow of water from the water tank back to the circular compartment.

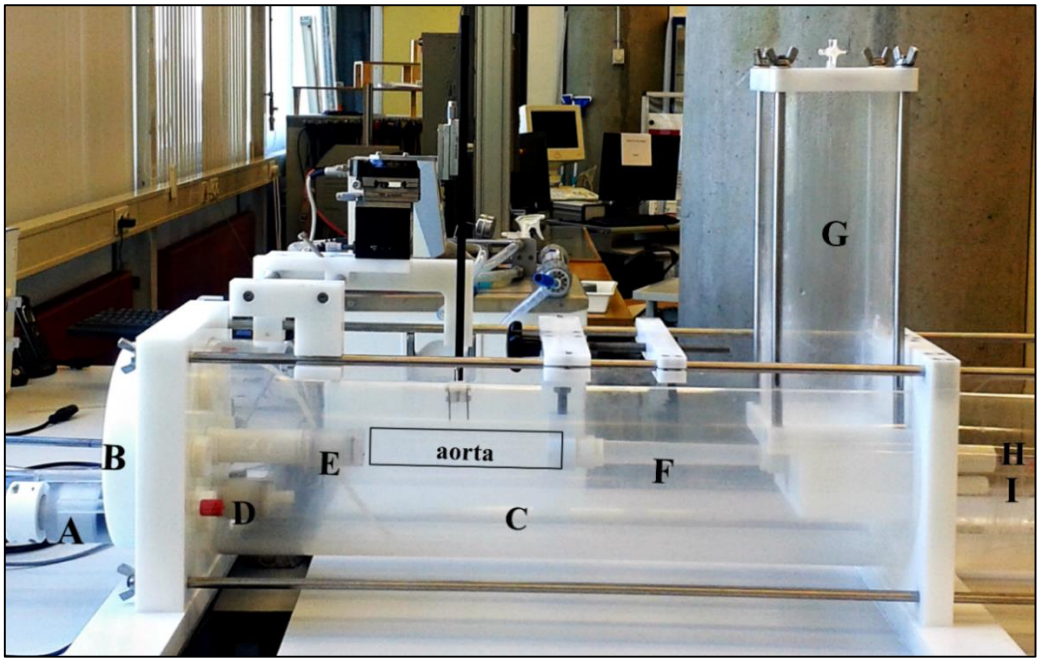

Figure 3.3 – The experimental setup. The axial piston pump (A) pushes the water from the circular compartment (B) towards the aorta, which is placed inside the water tank (C). A mechanical valve (D) is used to allow water to flow from the water tank back to the circular compartment but not vice versa. The proximal end (larger end) of the aorta is connected to another mechanical valve, i.e., 'aortic valve' (E), and the distal end (smaller end) to the silicon tube (F). This silicon tube is attached to a vertical air column (G) with two associated resistances (upper and lower resistance, H and I, respectively).

When placing the aorta inside the water tank, the proximal end (larger end) of the aorta is connected to the 'aortic valve', whereas the distal end (smaller end) of the aorta is connected to a silicon tube attached to a vertical air column. The silicon tube is used to facilitate the longitudinal pre-stretch of the aortic segment, as explained further below. The air column can be filled with water from the water tank and has two associated resistances (upper and lower resistance) that can be used to control the water inflow and outflow within the column. In fact, this part of the experimental setup is a representation of the 3-element arterial Windkessel model, which was proposed by Westerhof et al. (1969) as an improvement on the classical two-element Windkessel model introduced by the German physiologist Otto Frank (1899) for modelling the systemic circulation.

The 3-element Windkessel model comprises a compliant element, C_1, and two impedances, Z_1 and Z_0 (Figure 3.4). C_1 represents the blood storage capacity and is mainly determined by the elasticity of the large conduit arteries. Z_1 refers to the peripheral resistance and represents the viscous pressure drop, i.e., the contribution of the smallest vessels to resistance to flow, as resistance is inversely proportional to blood vessel radius to the power of fourth (Poiseuille's Law). C_1 and Z_1 are connected in parallel. Finally, Z_0, which is connected in series to C_1 and Z_1, and illustrates the aortic characteristic impedance; it symbolizes the impedance of the proximal end of the aorta. In fact, Z_0 was added to the 2-element Windkessel model to minimize high-frequency reflections at the boundary between the arterial vessel and the periphery (Westerhof et al., 1969).

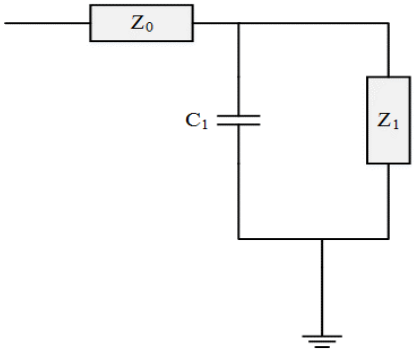

Figure 3.4 – The 3-element Windkessel model. C_1 represents the aortic compliance, Z_1 the peripheral resistance and Z_0 the characteristic impedance of the proximal end of the aorta (input impedance of the circuit).

Hence, it is possible to draw a parallel between the 3-element Windkessel model and the experimental setup. In this sense, the volume of air inside the vertical column and, to a lesser extent, the elasticity of the silicon tube represent the aortic compliance (C_1). Likewise, the upper resistance represents the aortic characteristic impedance (Z_0) and the lower resistance the peripheral resistance (Z_1). These two resistances control the water flow in and out of the vertical column (Figure 3.5). The upper resistance controls the water flow from the silicon tube into the air column, whereas the lower resistance determines the water flow from the air column into the water tank. Thus, the inflow should be opened ($Z_0 \approx 0$) and the outflow should be closed ($Z_1 >>$) when filling the air column with water (Figure 3.5).

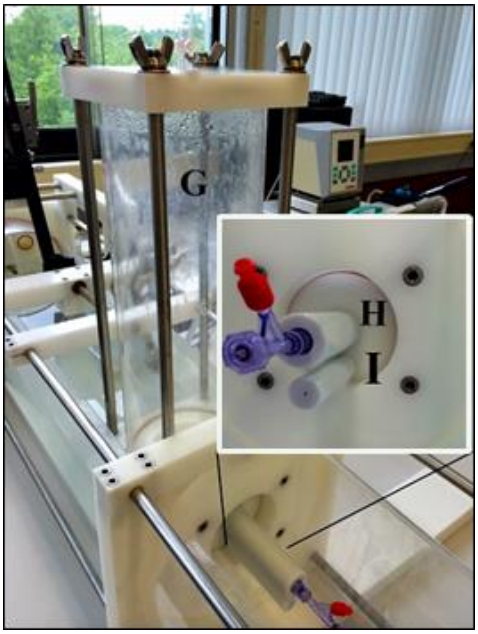

Figure 3.5 – The vertical air column (G) which can be filled with water and the two associated resistances (upper and lower resistances, H and I, respectively) zoomed in. Both resistances can be used to control the water level inside the air column. H is used to control the water inflow from the silicon tube into the air column, whereas I is used to determine the water flow from the air column into the water tank.

3.2.1 Preparation of the experimental setup

Before a description on the preparation of the experiments, some considerations about osmolarity need to be addressed. Osmolarity, or osmotic concentration, is a unit of solute concentration and is defined as the number of moles of ions that contribute to a solution's osmotic pressure; it is expressed in the number of milliosmoles per liter of solution (mOsm/L) (Smeltzer et al., 2010). Osmolarity is shown to have an influence on zero-stress state and on the mechanical properties of the aortic tissue (Guo et al., 2007). Hence, physiological saline solution was chosen for this

experiment since it has a total osmolarity of 308 mOsm/L, which lies within the range of blood osmolality (300-310 mOsm/L) (Smeltzer et al., 2010). In this sense, with the purpose of mimicking the *in vivo* physiological conditions, the water tank was filled with 30 liters of physiological saline solution. The concentration for physiological saline solution is 9 grams of salt per liter of water.

Furthermore, in order to obtain a controlled water temperature of 37ºC (typical body temperature), a heating circulator (Julabo F32 - Julabo©, Seelbach, Germany) - filled with tap water - was used in combination with a heat exchanger device (BIOtherm Heat Exchanger, Medtronic Inc., Minneapolis, USA). Heating the water in the setup consists of two separate loops (properly connected with silicon tubes) separated by the heat exchanger (Figure 3.6). The first loop contains saline solution from the experimental setup; it connects the water tank to the heat exchanger and is driven by a roller pump. On the other hand, the second loop contains tap water from the heating circulator and connects the heating circulator to the heat exchanger. In particular, the heat exchanger contains long and narrow pipes through which the salt water flows. Around those pipes the tap water from the heating circulator can flow. In this sense, the salt and tap water stay separated inside the heat exchanger, while the salt water gets heated. By means of heat transfer, the salt water is heated until a set temperature of 37°C. The temperature inside the water tank was monitored using a temperature sensor (Julabo©, Seelbach, Germany) connected to the heating circulator.

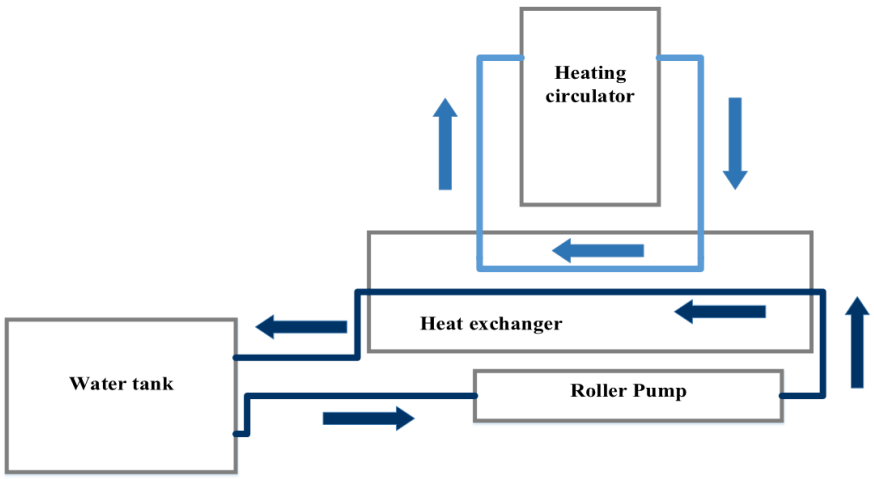

Figure 3.6 – Schematic overview of the two separate loops used for heating the water inside the water tank. The first loop (dark blue) contains salt water; a roller pump is used to push the water from the water tank into the heat exchanger, where it gets heated by the hot tap water that flows in its surroundings; then, the salt water returns to the water tank. The tap water circulates in a separate second loop (light blue) which connects the heating circulator to the heat exchanger.

As previously mentioned, the aorta was closed with connectors at both ends and placed in the experimental setup. The proximal end (larger end) of the aorta was connected to the 'aortic valve', whereas the distal end (smaller end) was connected to the silicon tube attached to the vertical air column.

To achieve more accurate and realistic conditions, the contribution of both aortic compliance and resistances in this experimental setup should be assured. In this sense, the piston pump was started with the purpose of filling the vertical air column with water. Then, the upper resistance was opened and the lower resistance was closed so that the water level inside the air column could rise. The water level was set approximately mid-height and both resistances were almost closed. The described procedure enabled the removal of all air out of the system.

Pressure during pumping was monitored using a pressure sensor (Peekel Instruments©, Rotterdam, NL) placed right after the distal end of the aorta. Before connecting it to the experimental setup, the pressure sensor was appropriately calibrated at zero pressure.

3.2.2 Applying the physiological pre-stretch

Taking into account *in vivo* physiological aortic loading conditions, the aorta was fixed at a constant pre-stretch in the longitudinal direction. Longitudinal pre-stretch is defined as the ratio between the length *in situ* of the sample and the length measured after it was removed from the body, in the longitudinal direction; it plays a crucial role in arterial biomechanics since it increases arterial wall load-bearing capacity (Schulze-Bauer et al., 2003; Horny et al., 2012).

In a previous study within our group, the physiological pre-stretch in the longitudinal direction (λ_{zz}) was determined for ten porcine aortas using a combined tensile-inflation test experiment (Peters et al., 2014). Several constant longitudinal pre-stretches were applied and pressure-force curves were analyzed. It was observed that λ_{zz} was approximately 1.22, i.e., 22% of the aorta's initial length. At this stretch, no longitudinal force was measured during pulsatile pressurization. Furthermore, this value of the longitudinal pre-stretch lies within the range reported by Horny at al. (2012) in a study on abdominal aortas of human cadavers: 1.18 ± 0.10 for male and 1.14 ± 0.10 for female abdominal aortas. Hence, a longitudinal pre-stretch of 1.22 was used in these experiments.

The aorta was hanging slightly curved (not straight) in the experimental setup. To apply the 22% longitudinal pre-stretch, first the initial (stress-free) length (L_0) should be determined. In this particular situation, the aorta should just be hanging straight in the setup with a minimal

(unloaded) longitudinal stretch. Thus, the longitudinal stretch was increased progressively – using a specific longitudinal pre-stretch device (Figure 3.7) - until the aorta seemed to be not too loose and not too stretched at the same time, as assessed by palpation, resulting in a stress-free length (L_0). L_0 was then determined by measuring the length between the inner tie wraps using a regular ruler. Next, the length for the physiological pre-stretch was determined multiplying L_0 by 1.22 and the correct stretch was applied to the aorta. At this point, the experimental setup was finally prepared to use.

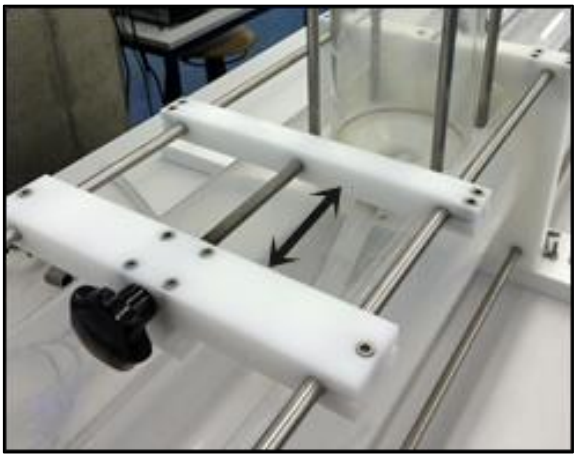

Figure 3.7 - The pre-stretch device used to apply the physiological longitudinal pre-stretch. The two-headed black arrow indicates the direction in which the distance between the two connectors attached to the aorta was increased to apply a pre-stretch in the longitudinal direction.

3.2.3 Applying the pressure pulse

The axial piston pump was connected to a PC workstation. A graphical user interface (GUI) was created using LabVIEW© (National Instruments©, Redmond, USA, 1986) with the purpose of modelling the dynamics of the piston pump.

Dynamic and static inflation experiments were performed in the aortic segments.

In the static experiment, the goal is to perform an inflation experiment for a large pressure range, thereby capturing the complete mechanical behavior of the aortic tissue. These experiments have been performed in a previous study using a less sophisticated experimental setup. The results were compared to bi-axial tensile test experiments to validate the mechanical characterization of aortic tissue using this method (Peters, 2013; Lopata et al., 2014).

In the present study, a pressure pulse, which led to a pressure signal between 0 mmHg and 140 mmHg and an increasing vessel diameter, was applied. The shape of the flow pulse was chosen such that the diameter increased linearly over time, i.e., the same (incremental) increase in circumferential stretch was found between consecutive ultrasound images. An example of the pressure signal for the static experiment is illustrated in Figure 3.8.

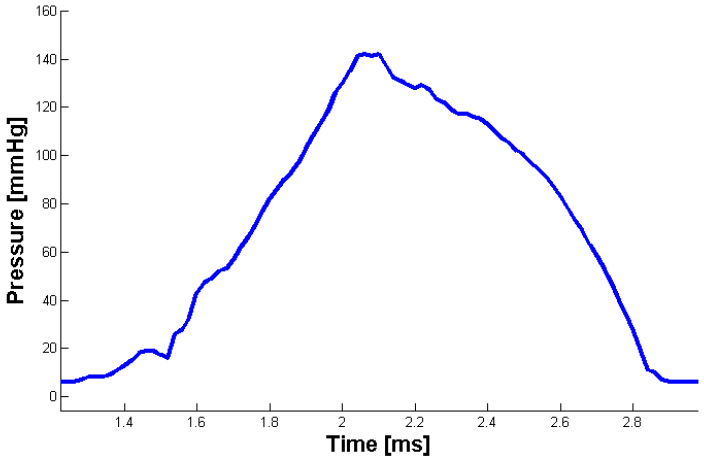

Figure 3.8 - Pressure signal obtained during the static experiment.

Furthermore, in the static experiment, there is a crucial adjustment in the setup that has to be made in order to be able to pump from 0 mmHg to 140 mmHg: the 'aortic valve' should remain opened during pumping, in order to let pressure drop to 0 mmHg for every cycle. A cylindrical iron bar was used for this purpose. The right end of the bar prevented the 'aortic valve' from closing allowing for a complete inflation of the aorta (Figure 3.9).

Figure 3.9 – The cylindrical iron bar is pushed to the right for the static experiment, preventing the aortic valve from closing and thus allowing for a complete deflation of the aortic segment.

Secondly, in the dynamic experiment, the aim was to apply a pulse that resembles the physiological pressure pulse, i.e., approximately between 70 mmHg and 130 mmHg, with the commonly known physiological pressure shape (Figure 3.10). An example of the pressure signal for the dynamic experiment is shown in Figure 3.11.

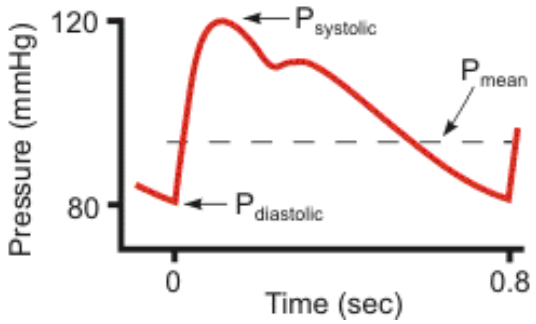

Figure 3.10 – The physiological pressure signal (Klabunde, 2005).

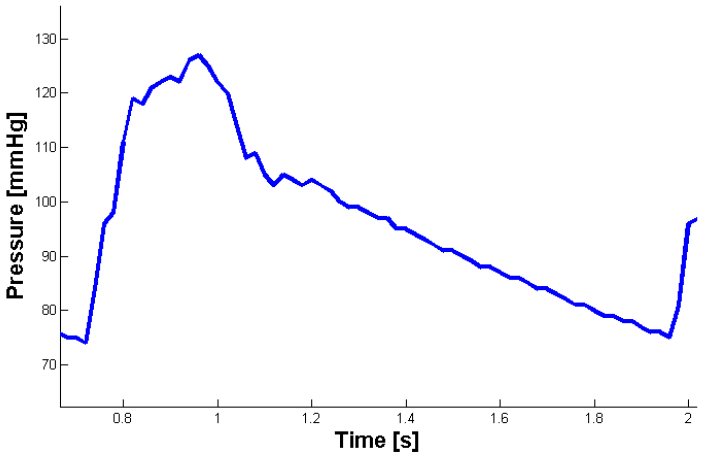

Figure 3.11 – Pressure signal obtained during the dynamic experiment.

Since both dynamic and static pressure pulses are applied to the aorta, two different input dat-files containing the respective pressure signal graphs were created in Matlab© (R2013b, Mathworks Inc., Natick (MA), USA) and added to the Labview© GUI-file. Hence, the dynamics of the piston pump was completely dependent on the selected pressure signal, i.e., the selected dat-file.

Moreover, parameters such as amplitude, requested time interval, and the number of cycles could be adjusted in the Labview© GUI-file for both dynamic and static experiments. The amplitude refers to the amount of water, i.e., the stroke volume, pushed by the piston into the

system in a certain period of time, and it could be changed with the purpose of increasing or decreasing the maximum and the minimum pressure obtained. Usually, the stroke volume applied for the static experiment was found to be 3 times the stroke volume used for the dynamic experiment. The requested time interval was set to 10 ms for the dynamic experiment and to 20 ms for the static experiment, since the latter requires more pressure data points. Finally, the number of cycles was set to 1000 for both experiments to prevent the setup from stopping during the ultrasound data acquisition.

During both dynamic and static experiments, US-data of the aorta were acquired and pressure data was saved and transmitted to a PC-based workstation.

3.3. US acquisition

The US probe was placed just below the water surface using a probe holder device (Figure 3.12). The probe was positioned at the center of the aorta to avoid boundary effects in the measurement plane caused by the cannulation of the aorta near the ends. The surrounding water allowed for a larger field-of-view (FOV) for the US measurements by acting as a medium between the US probe and the aortic wall (Lopata et al., 2014).

Before each US acquisition, the aorta image quality was optimized. Several settings could be changed, such as, gain (brightness), width, depth, focus and frequency of the US beam. The optimal settings were reached when the aorta was in the middle of the FOV, no reverberations were near to the aortic wall and the outer and inner wall were clearly visible as bright edges/lines.

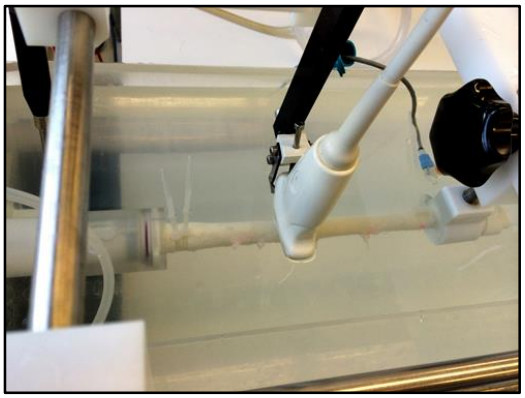

Figure 3.12 – Positioning the US probe in the setup (position for cross-sectional view).

US-data were recorded using a MyLab 70 US-scanner (Esaote© Europe, Maastricht, NL) (Figure 3.13) equipped with a 2D linear array probe (LA-523) with a frequency range of 4-13 MHz and a lateral sampling of 38 RF-lines/cm, and a module to capture the raw radiofrequency (RF) data. The RF-data were digitized at a sampling rate of 50 MHz and transmitted and saved to a PC-based workstation (Art.LAB© system, Esaote Europe, Maastricht, NL). The distance between the RF-lines, the so-called 'pitch', was 315 µm. The RF-data were acquired with a center frequency of 8.7 MHz, resulting in a spatial resolution of 354 µm by 315 µm. The temporal resolution, i.e., the frame rate, was 62 Hz.

A rack-mounted BNC terminal block (NI BNC-2090, National Instruments©, Redmond (WA), USA), in combination with a tee connector and BNC cables, was used to connect the pressure sensor to a PC-workstation (LabVIEW©) and the latter to the ArtLAB© system. The pressure signal was automatically saved during the US-acquisition in the ArtLAB© system together with the raw RF-data (Figure 3.14). One pressure sample was saved per RF-line, resulting in a total sampling of 8 kHz. However, only one sample was used per frame for further processing. Hence, the sampling of the pressure data was equal to the US frame rate (= 62 Hz).

Figure 3.13 – US-Scanner used in the experiments (MyLab 70 US scanner, Esaote© Europe, Maastricht, NL).

One longitudinal (long axis) and two cross-sectional (short axis) B-mode US recordings (Figure 3.15) were acquired for both static and dynamic experiments. Aortic side-branches were used as a reference to select the same location of measurement within the aortic segment for all three B-mode imaging planes (Figure 3.16). The two cross-sectional B-mode US images were acquired in two different regions within the aorta.

Hence, 6 US measurements (data sets) were obtained for each aorta (Figure 3.17).

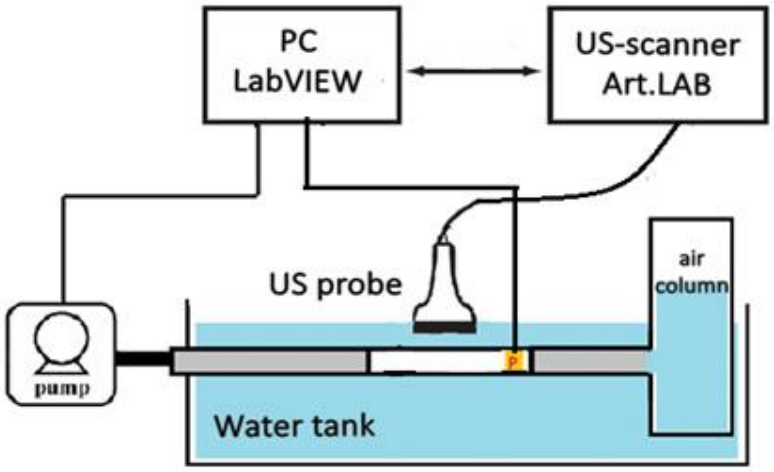

Figure 3.14 – Schematic overview of the interaction between the main components of the devised laboratory setup: the axial piston pump, the water tank, the air column, the US probe, the PC workstation and the US-scanner with the associated ArtLAB© system. P (in red in this figure) represents the pressure sensor. During the US-acquisition, the pressure signal and the raw RF-data are automatically saved in the ArtLAB© system.

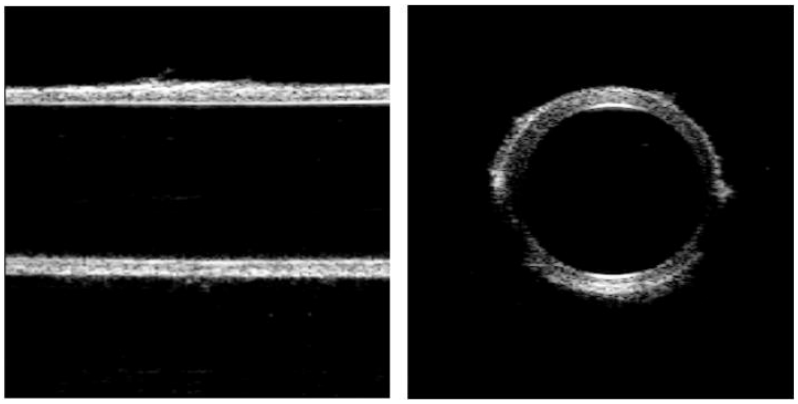

Figure 3.15 – Example of longitudinal (left) and cross-sectional (right) B-mode US images obtained.

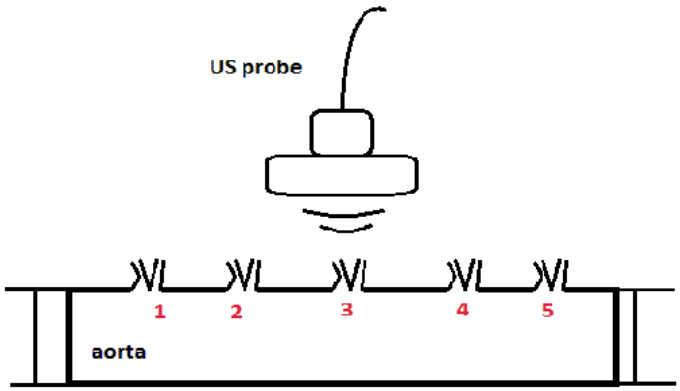

Figure 3.16 – Schematic overview of the US acquisition within the aortic segment. In this figure, as an example, one longitudinal B-mode US image is acquired between the second and the fourth side branch of the aorta. Next, cross-sectional B-mode US images are acquired between the second and third side branches (cross-section 1) and between the third and fourth side branches (cross-section 2). The numbers 1-5 (in red) indicate the side branches.

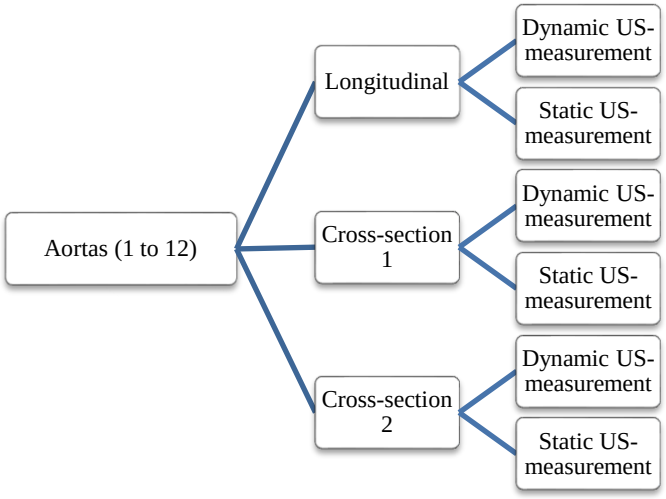

Figure 3.17 – Schematic overview of the 6 different US data sets acquired for each aorta.

3.4. US-Data Processing

The raw RF-data from these static and dynamic US-measurements were imported and analyzed in Matlab©. First, an M-mode image of the aorta was obtained, wherein a region including the frames of one complete cycle was selected. Next, the data were manually segmented, yielding a delineation of the aortic wall and a global region of interest (ROI) completely surrounding the aortic wall, both necessary for further processing. For longitudinal US images, the upper and the lower inner wall were manually segmented and a spline interpolation was used to fit a curve through the selected points. For the cross-sectional images, the inner wall was manually segmented and a spline interpolation was also used to fit a curve through the selected points.

The RF-data were processed using a 2D iterative coarse-to-fine displacement estimation algorithm (Lopata et al., 2009) to assess displacements in the axial (depth) and lateral (width) direction. The 2D displacements were estimated in three iterative steps using both signal envelope data (first iteration) and RF-data (second and third iterations). A general overview of the aforementioned algorithm is described below.

In each step, a 2D pre-compression window of data in image μ is correlated with a 2D post-compression window in image $\mu+1$, that is larger in both dimensions. The size of the post-compression window defines and limits the range of possible axial and lateral displacements measured. The axial and lateral displacements were estimated by calculating the shift of the maximum of the cross-correlation function (CCF) in both directions. Additionally, a parabolic curve fitting was applied to the peak of the CCF to obtain sub-sample displacement estimates, i.e., displacements smaller than one pixel (Lopata et al., 2009). This procedure is repeated for all possible windows within the ROI.

In the first step of this iteration process, segments of envelope data of two consecutive frames were used to measure the coarse (global) displacements of the signals. The next two iteration steps were performed in RF-data to obtain displacement estimates in a finer scale. Actually, in a study of Lopata et al. (2009), it was concluded that it is preferred to use envelope data on a coarse scale, since larger windows of RF-data will suffer more from decorrelation, i.e., reduction in cross-correlation within pre-compression and post-compression signals, which is caused by the displacement of scattering particles during stretching of the tissue (Ophir et al., 1991; Lopata et al., 2009).

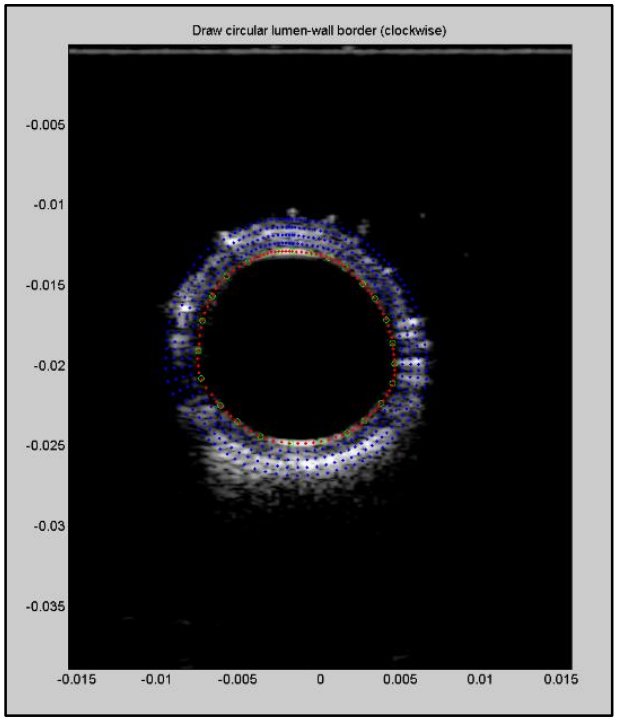

Figure 3.18 - Example of a manual inner wall segmentation performed in a US cross-sectional image. The red points represent aortic inner wall points (manual segmentation). The blue points are defined in the outward direction, i.e., in the normal direction of the red circle, defining the vessel wall.

In each iteration step, the window size was decreased in the axial direction and the maximum shift in the axial direction was fixed at 50% of the used window size, resulting in a higher resolution and a more accurate displacement estimation (Lopata, 2010). All resulting displacements were smoothed using a median filter to remove possible outliers.

After estimating the displacements in the global ROI of the US image, the aortic inner wall was tracked, using the manually segmented points in the vessel wall (Figure 3.18) and the displacement estimates. The manually defined contours of the first time frame of each data set were used as a starting point for the automated 2D vessel tracking.

The frame-to-frame displacements were used to track the segmented aortic wall for all time frames, yielding a measurement of diameter as function of pressure. For longitudinal US images, the diameter was calculated taking the distance between a point in the upper wall and the corresponding point in the lower wall.

Likewise, for cross-sectional US images the luminal curve was tracked over all time frames. Next, the fitting curve was tracked for all time frames. In this case, since a circular shape was

assumed for the lumen of the aorta, the area was calculated as function of pressure and, as a result, the diameter could be determined using $d(p) = 2\sqrt{\frac{A(p)}{\pi}}$.

3.4.1 US-Data Post-Processing and Analysis

Since RF-data and pressure data were saved at different starting time points due to a delay in the pressure acquisition system, diameter and pressure curves needed to be synchronized to get an accurate pressure-diameter behavior. The minimum and maximum of both diameter and pressure curves were adjusted to match each other (Figure 3.19). As a result, a more accurate frame set was obtained. The inflation part of the data, i.e., from minimum to maximum pressure, was used for further processing,

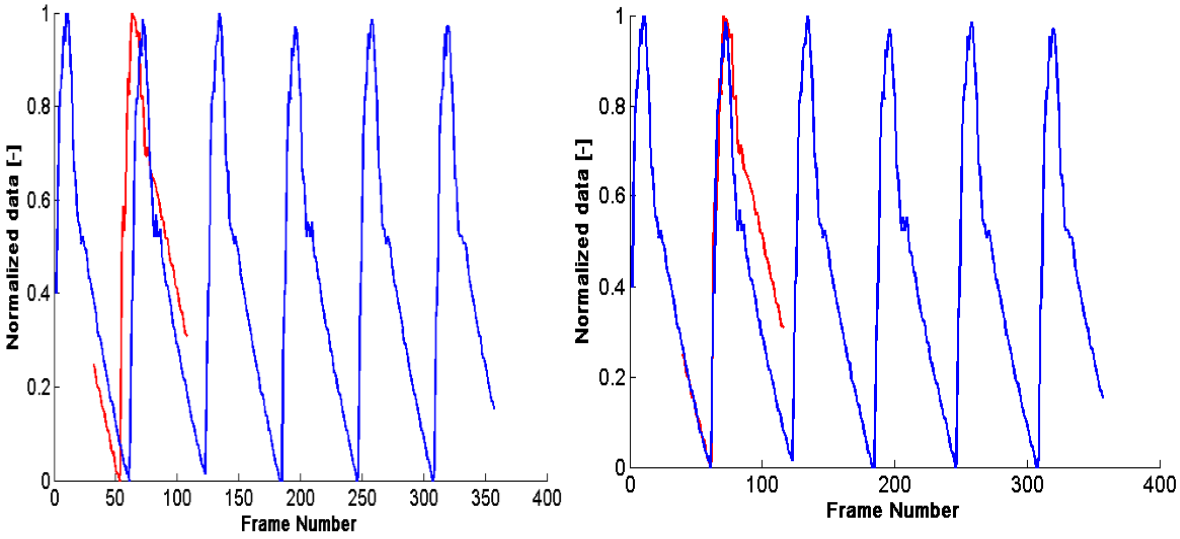

Figure 3.19 – Example of pressure and diameter curves before (left) and after (right) synchronization is performed. The red curve represents diameter data, whereas the blue curve represents pressure data. It should be noted that both curves were normalized with respect to their respective maximum values. The horizontal axis corresponds to the number of frames.

The aforementioned procedure including manual 2D vessel segmentation, 2D displacement estimation and 2D vessel tracking is performed once more, but now for this particular frame set, yielding more accurate values of pressure and diameter, which were saved in two separate arrays.

Furthermore, the initial wall thickness was measured manually in the B-mode image that corresponds to the first frame of the aforementioned frame set. This was done in Matlab©, taking the distance between the outer and the inner aortic wall. Considering each of the three different

B-mode image views acquired (longitudinal, cross-section 1 and cross-section 2), three values of the initial wall thickness were obtained for static and dynamic US-measurements, respectively. In particular, for the B-mode cross-sectional images, the wall thickness was measured at 6 and 12 o'clock, where the resolution is higher and thus it is easier to distinguish the outer and inner aortic wall (bright edges) (Figure 3.15). The mean of these three values of initial wall thickness was calculated for static and dynamic US-measurements and used for further processing.

All the steps of the abovementioned method were applied to the 6 US data sets acquired for each aorta.

Pressure and diameter, both as function of time, and the mean value of the initial wall thickness were obtained. These three parameters were used for the mechanical characterization of the aortic tissue.

3.5 Mechanical characterization

The mechanical behavior of the aortic tissue was modelled as a neo-Hookean material. The Neo-Hookean model is valid for large deformations and assumes linear elastic, isotropic behavior and incompressibility of the tissue (Lopata et al., 2014). For the US-experiments, a segment of the vessel can be visualized as a flat strip, allowing for a more practical continuum mechanics analysis (Figure 3.20).

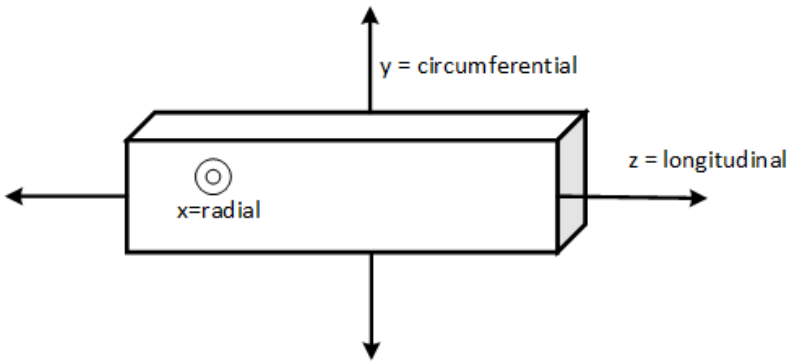

Figure 3.20 – The vessel visualized as a flat strip with the corresponding radial (x-direction), circumferential (y-direction) and longitudinal (z-direction) directions.

The stress-state for a Neo-Hookean material is described as:

$$\sigma = -p_0\boldsymbol{I} + G(\boldsymbol{B} - \boldsymbol{I}) \tag{3.1}$$

In equation 3.1, σ is the Cauchy stress tensor, p_0 is an undetermined hydrostatic pressure contribution, $\boldsymbol{I}$ is the identity matrix, G is the shear modulus and $\boldsymbol{B}$ is the left Cauchy-Green deformation tensor or Finger tensor (Holzapfel et al., 2000), which can be defined as:

$$\boldsymbol{B} = \boldsymbol{F} \cdot \boldsymbol{F}^T \tag{3.2}$$

The Finger strain is defined as (Humphrey, 2002):

$$\varepsilon_F = \frac{1}{2}(\boldsymbol{B} - \boldsymbol{I}) \tag{3.3}$$

Thus, equation 3.1 can be rewritten as:

$$\boldsymbol{\sigma} = -p_0\boldsymbol{I} + 2G\varepsilon_F \tag{3.4}$$

Taking into account that the experiment can be divided in two steps, i.e., first applying a longitudinal pre-stretch and then increasing the pressure (inflation of the vessel), the deformation tensor $\boldsymbol{F}$ can be split into two separate tensors, i.e., $\boldsymbol{F_0}$ and $\boldsymbol{F_1}$ (Figure 3.21). Note that the directions x, y and z correspond to the radial, circumferential and longitudinal direction, respectively (Figure 3.20). By assuming incompressibility, the determinant of both $\boldsymbol{F_0}$ and $\boldsymbol{F_1}$ has to equal 1.

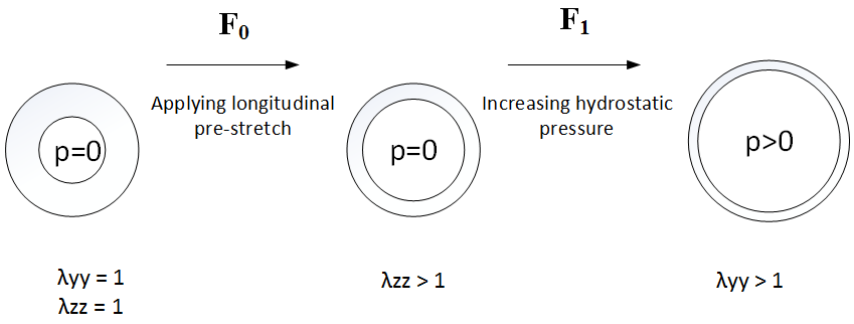

Figure 3.21 - The two steps of the US-experiments: first, the aorta is subject to a longitudinal pre-stretch of 1.22 (F_0) and then to an increasing hydrostatic pressure (F_1). It should be noted that the circles illustrated in the figure represent cross-sectional views of the aorta.

In the first step, as previously mentioned, a longitudinal pre-stretch of 1.22, i.e., 22% of its initial length, is applied to the vessel. Therefore, the resulting deformation tensor $\boldsymbol{F_0}$ is:

$$F_0 = \begin{bmatrix} \frac{1}{\sqrt{\lambda_{zz}}} & 0 & 0 \\ 0 & \frac{1}{\sqrt{\lambda_{zz}}} & 0 \\ 0 & 0 & \lambda_{zz} \end{bmatrix} \tag{3.5}$$

where λ_{zz} corresponds to the pre-stretch in the longitudinal direction.

Next, the vessel is inflated using a hydrostatic pressure p (Figure 3.21). As a result, the deformation tensor $\boldsymbol{F_1}$ can be described as follows:

$$\boldsymbol{F}_1 = \begin{bmatrix} \frac{1}{\lambda_{yy}} & 0 & 0 \\ 0 & \lambda_{yy} & 0 \\ 0 & 0 & 1 \end{bmatrix} \tag{3.6}$$

where λ_{yy} corresponds to the stretch in the circumferential direction with respect to the vessel's diameter. Particularly, λ_{yy} can be defined as:

$$\lambda_{yy} = \frac{d(p)}{d_0} \tag{3.7}$$

Here $d(p)$ corresponds to the pressure-dependent diameter and d_0 is the initial diameter before the inflation, i.e., the diameter at $p = 0$, yet after applying the longitudinal pre-stretch λ_{zz}.

Hence, the total deformation tensor $\boldsymbol{F}$ can be described as the product of both deformation tensors $\boldsymbol{F_0}$ and $\boldsymbol{F_1}$. As a result, $\boldsymbol{F}$ can be defined by the following matrix:

$$\boldsymbol{F} = \begin{bmatrix} \frac{1}{\lambda_{yy}\sqrt{\lambda_{zz}}} & 0 & 0 \\ 0 & \frac{\lambda_{yy}}{\sqrt{\lambda_{zz}}} & 0 \\ 0 & 0 & \lambda_{zz} \end{bmatrix} \tag{3.8}$$

Next, the left Cauchy-Green deformation tensor $\boldsymbol{B}$ can now be calculated using equation 3.2 and becomes:

$$\boldsymbol{B} = \begin{bmatrix} \frac{1}{{\lambda_{yy}}^2\lambda_{zz}} & 0 & 0 \\ 0 & \frac{{\lambda_{yy}}^2}{\lambda_{zz}} & 0 \\ 0 & 0 & {\lambda_{zz}}^2 \end{bmatrix} \tag{3.9}$$

The application of the Neo-Hookean material model constitutive equation (equation 3.1) for the total deformation tensor $\boldsymbol{F}$ leads to the following expressions for the stress in the circumferential direction (σ_{yy}), radial direction (σ_{xx}) and longitudinal direction (σ_{zz}), respectively:

$$\sigma_{yy} = -p_0 + G\left(\frac{{\lambda_{yy}}^2}{\lambda_{zz}} - 1\right) \tag{3.10}$$

$$\sigma_{xx} = -p_0 + G\left(\frac{1}{{\lambda_{yy}}^2\lambda_{zz}} - 1\right) \tag{3.11}$$

$$\sigma_{zz} = -p_0 + G\left({\lambda_{zz}}^2 - 1\right) \tag{3.12}$$

Next, by combining equation 3.10 with equation 3.11, the unknown variable p_0 can be eliminated:

$$\sigma_{yy} - \sigma_{xx} = G\left(\frac{{\lambda_{yy}}^2}{\lambda_{zz}} - \frac{1}{{\lambda_{yy}}^2\lambda_{zz}}\right) = \frac{G}{\lambda_{zz}}\left({\lambda_{yy}}^2 - \frac{1}{{\lambda_{yy}}^2}\right) \tag{3.13}$$

In other words, the difference between circumferential and radial stress and the circumferential and longitudinal stretch are required to estimate the shear modulus.

Moreover, from equations 3.3 and 3.13 the Finger strain can be rewritten as:

$$\varepsilon_F = \frac{1}{2\lambda_{zz}}\left({\lambda_{yy}}^2 - \frac{1}{{\lambda_{yy}}^2}\right) \tag{3.14}$$

It is assumed that there is no additional stretching in the z-direction (longitudinal direction) due to the increase in pressure, thus λ_{zz} remains constant and equal to 1.22.

Additionally, the stretch in the radial direction (λ_{xx}) can be defined as:

$$\lambda_{xx} = \frac{h(p)}{h_0} \tag{3.15}$$

with h_0 referring to the wall thickness before inflation, i.e., the wall thickness at p = 0. Assuming incompressibility of the tissue, the determinant of the total deformation tensor $\boldsymbol{F}$ must be equal to 1. In this case, λ_{zz} can be neglected as the stretch in the longitudinal direction is assumed to be constant throughout the inflation experiment, so for $\boldsymbol{F_1}$.

As a result, for $\boldsymbol{F_1}$

$$\lambda_{xx}\lambda_{yy} = 1 \Rightarrow \lambda_{xx} = \frac{1}{\lambda_{yy}} \tag{3.16}$$

Combining equations 3.15 and 3.16, one can obtain the following expression for the wall thickness at pressure *p*:

$$h(p) = \frac{h_0}{\lambda_{yy}} \tag{3.17}$$

In a previous study, the circumferential stress was estimated using the Law of Laplace (Lopata et al., 2014), using the approximation for thin-walled cylinders ($h(p)/d(p) < 0.05$ or $h(p)/r(p) < 0.1$, with $r(p)$ the pressure-dependent radius). However, healthy aortas do not meet this criterion. For this purpose, the equations for a thick-walled cylinder were derived. The starting point is the momentum equation:

$$\nabla\sigma = 0 \tag{3.18}$$

This equation states that the divergence of stress (σ) should equal zero (Holzapfel et al., 2000). From this equation, the different components of stress can be derived. In polar coordinates, the radial component is given by:

$$\frac{d\sigma_{rr}}{dr} + \frac{1}{r}(\sigma_{rr} - \sigma_{\theta\theta}) \tag{3.19}$$

with σ_{rr} the radial stress, $\sigma_{\theta\theta}$ the circumferential stress and *r* the radius (Holzapfel et al., 2000). If we apply the nomenclature used in this study, this equation is identical to

$$\frac{d\sigma_{xx}}{dr} + \frac{1}{r}\left(\sigma_{xx} - \sigma_{yy}\right) \tag{3.20}$$

A general solution for this differential equation are the so-called Lamé equations:

$$\sigma_{xx} = A - \frac{B}{r^2}$$

$$\sigma_{yy} = A + \frac{B}{r^2} \tag{3.21}$$

with *A* and *B* integration constants. These constants can be found by applying the governing boundary conditions that hold for the inflation experiment:

$$\sigma_{xx} = -p \qquad \text{for } r = r_i \quad \text{(inner radius)} \tag{3.22}$$

$$\sigma_{xx} = 0 \qquad \text{for } r = r_o \quad \text{(outer radius)}$$

Substitution of (3.21) into (3.22) yields:

$$A = \frac{-p}{\left(1 - \frac{r_o^2}{r_i^2}\right)} \qquad \text{and} \qquad B = \frac{-pr_o^2}{\left(1 - \frac{r_o^2}{r_i^2}\right)} \tag{3.23}$$

Finally, the resulting equations for radial and circumferential strain are:

$$\sigma_{xx} = \frac{r_i^2 p}{r_o^2 - r_i^2}\left(1 - \frac{r_o^2}{r^2}\right) \tag{3.24}$$

$$\sigma_{yy} = \frac{r_i^2 p}{r_o^2 - r_i^2}\left(1 + \frac{r_o^2}{r^2}\right) \tag{3.25}$$

It can be derived that these relations hold for both tubes with open and closed ends, which hold when the axial dimension of the cylinder is large with respect to diameter and wall thickness.

The average stress in the wall in the radial direction can be found by means of integration:

$$\bar{\sigma}_{xx} = \frac{\int_{r_i}^{r_o} \sigma 2\pi r dr}{\int_{r_i}^{r_o} 2\pi r dr} = \frac{\int_{r_i}^{r_o} \sigma r dr}{\int_{r_i}^{r_o} r dr} = \frac{\frac{r_i^2 p}{r_o^2 - r_i^2}\left[\left(\frac{1}{2}r^2 - r_o^2 \log(r)\right)\right]_{r_i}^{r_o}}{\left[\frac{1}{2}r^2\right]_{r_i}^{r_o}}$$

$$= \frac{\frac{r_i^2 p}{r_o^2 - r_i^2}\left[\left(\frac{1}{2}r^2 - r_o^2 \log(r)\right)\right]_{r_i}^{r_o}}{\frac{1}{2}\left(r_o^2 - r_i^2\right)} \tag{3.26}$$

Similarly, an expression for the circumferential stress can be obtained:

$$\bar{\sigma}_{yy} = \frac{\frac{r_i^2 p}{r_o^2 - r_i^2}\left[\left(\frac{1}{2}r^2 + r_o^2 \log(r)\right)\right]_{r_i}^{r_o}}{\left[\frac{1}{2}r^2\right]_{r_i}^{r_o}} = \frac{\frac{r_i^2 p}{r_o^2 - r_i^2}\left[\left(\frac{1}{2}r^2 + r_o^2 \log(r)\right)\right]_{r_i}^{r_o}}{\frac{1}{2}\left(r_o^2 - r_i^2\right)} \tag{3.27}$$

The resulting mean stress difference becomes:

$$\bar{\sigma}_{yy} - \bar{\sigma}_{xx} = \frac{4 p r_i^2 r_o^2 (\log(r_o) + \log(r_i))}{\left(r_o^2 - r_i^2\right)^2} \tag{3.28}$$

Finally, the shear modulus can be estimated using this equation:

$$\bar{\sigma}_{yy} - \bar{\sigma}_{xx} = G\left(\lambda_{yy}^2 - \frac{1}{\lambda_{yy}^2}\right)/\lambda_{zz} \tag{3.29}$$

with *G* being the only unknown parameter, which was estimated using a least-squares fitting method in Matlab©, resulting in estimated values of *G* for static and dynamic US-measurements for all twelve aortas.

3.6 Incremental shear modulus

A study on determining the incremental shear modulus for a limited pressure range was performed, considering a specific region of the static pressure-diameter curve. The aim is two-fold:

1) Determine the dependency of the incremental shear modulus (G_{inc}) to mean arterial pressure (MAP) and pulse pressure (ΔP). The mean arterial pressure was varied from 40 to 110 mmHg in 2 mmHg steps. This was repeated for a ΔP of 30, 40, 50 and 60 mmHg, respectively.

$$MAP \approx \frac{2}{3} P_{dia} + \frac{1}{3} P_{sys} \tag{3.30}$$

$$\Delta P = P_{sys} - P_{dia} \tag{3.31}$$

2) Compare the results of the dynamic, 'in vivo' experiment to the incremental modulus for the matching pressure range, derived from the static experiment. Therefore, this study can be regarded as an indirect method to calculate G_{inc}, since it was performed on the data resulting from the analysis of each static US data set.

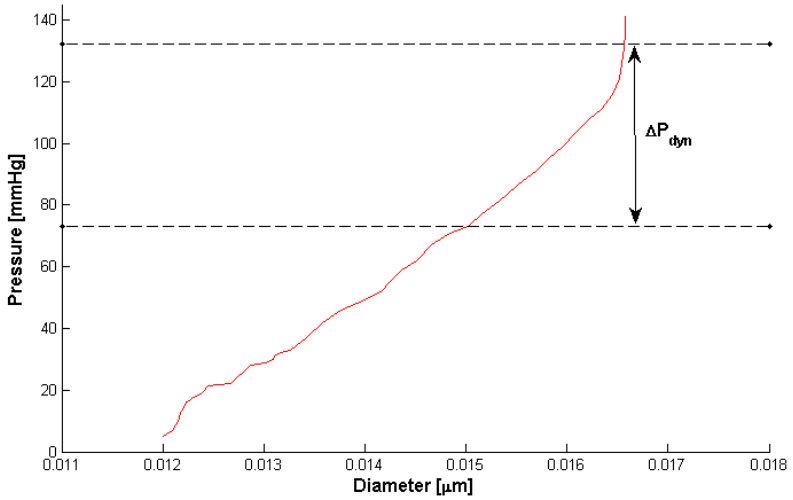

Figure 3.22 – Example of a static pressure-diameter curve (in red) obtained. The region of the plot between the black dashed lines represent the respective dynamic pressure range (ΔP_{dyn}). The dynamic pressure range (ΔP_{dyn}) is defined as the difference between the systolic pressure (P_{sys}) and the diastolic pressure (P_{dia}).

For each US view (longitudinal, cross-section 1 and cross-section 2), there is a static US data set and a dynamic US data set. For the equivalent pressure range, the diameters between the diastolic and systolic pressures were obtained. The new pressure and diameter data have the same length.

Next, by applying equation 3.17, the wall thickness with respect to pressure (*h(p)*) was calculated.

It must be noted that, when exact diastolic and/or systolic pressure were not within the static pressure array, linear interpolation was performed on the pressure-diameter or pressure-wall thickness data in Matlab© to get the corresponding values of diameter and wall thickness for diastolic and/or systolic pressure.

Finally, the shear modulus was estimated, again using a least-squares fitting method in Matlab©.

3.7 Statistical analysis

Paired sample Student's t-tests are commonly used to compare the average values of the same measurement made under two different methods or conditions. Therefore, paired sample Student's t-tests were used to compare the average values of *G*, obtained using two different conditions, tested both on the same subject (e.g. different US imaging planes). This statistical test is based on the paired differences between these two values. The tests were performed at α*100% significance level, with α=0.05 (alpha value). Two-tailed p-values were calculated and compared with the alpha value.

Tests were performed to check whether there were significant differences in the average values of *G* between the different US imaging planes, for each experiment (static and dynamic). Furthermore, again a paired sample Student's t-test was used to detect whether there were significant differences between the overall mean *G* obtained from the incremental analysis and from the dynamic experiment.

Moreover, a Bland-Altman plot was constructed with the purpose of comparing different estimates of *G*, obtained with the incremental analysis and dynamic experiment for matching pressure ranges. A Bland-Altman plot is a statistical tool extensively used to evaluate the agreement between two different methods. It is often used in biostatistics as an alternative to correlation coefficients, which can be misleading (Bland & Altman, 1986). In this graphical

approach, the difference in result between the two methods is plotted against the average of the two methods. Additionally, horizontal lines are plotted at the mean difference and at the limits of agreement, defined as the mean difference plus and minus 1.96 times the standard deviation of the differences.

The aforementioned statistical analyses were performed in Matlab©.

4. Results

4.1 Static US-measurements

Prior to the static and dynamic US-measurements, the initial length (L_0) of the aorta was measured and a 22% of longitudinal pre-stretch was applied to the aortic segment. The initial length and the resulting lengths considering the 22% longitudinal pre-stretch are presented in Table 4.1. A mean initial length of 14.4 cm was found within a range of 11.0-15.8 cm.

Table 4.1 – Initial length (L_0) [cm] measured for each aorta and the respective resulting length after applying the 22% of longitudinal pre-stretch [cm].

	Initial length (l_0) [cm]	1.22*l_0 [cm]		Initial length (l_0) [cm]	1.22*l_0 [cm]
Aorta 1	14.6	17.8	Aorta 7	14.8	18.1
Aorta 2	14.2	17.3	Aorta 8	12.7	15.5
Aorta 3	14.5	17.7	Aorta 9	15.8	19.3
Aorta 4	15.2	18.5	Aorta 10	15.0	18.3
Aorta 5	15.6	19.0	Aorta 11	11.0	13.4
Aorta 6	13.3	16.2	Aorta 12	15.5	18.9

In addition, the wall thickness was measured manually for the three different static US data sets comprising each aorta. The mean wall thickness of the three US views was calculated and assumed for each aorta and used in the analysis of each static US data set. Table 4.2 shows the resulting mean wall thickness of the twelve aortas with regard to the static US-experiments. An overall mean initial wall thickness of 1.407 ± 0.098 mm (mean ± standard deviation) was found.

Table 4.2 – The resulting initial wall thickness (h_0) [mm] of the twelve porcine aortas obtained from the analysis of the static US data sets.

	Initial wall thickness (h_0) [mm]		Initial wall thickness (h_0) [mm]
Aorta 1	1.496	Aorta 7	1.584
Aorta 2	1.373	Aorta 8	1.437
Aorta 3	1.391	Aorta 9	1.290
Aorta 4	1.320	Aorta 10	1.494
Aorta 5	1.290	Aorta 11	1.290
Aorta 6	1.422	Aorta 12	1.496

In the static US-experiment, the purpose was to obtain a pressure signal from 0 mmHg to 140 mmHg. However, it was observed that the resulting static pressure ranges obtained from the analysis in Matlab© differed between aortas and within the same aorta. Considering all the static US-experiments performed in the twelve aortas, the minimum pressure was found within the range of 0 - 11 mmHg, whilst the maximum pressure varied within the range of 135 - 145 mmHg.

The resulting diameter and pressure ranges together with the initial wall thickness were used as input parameters in the calculation of the shear modulus *G* of the aortic tissue (equation 3.29). As an example, table 4.3 presents the three input parameters and the resulting values for the shear modulus considering the different static US-measurements performed in aorta 2. The corresponding tables for all aortas are shown in Appendix A1.

Table 4.3 – Diameter range (ΔD) [mm], pressure range (ΔP) [mmHg], initial wall thickness (h_0) [mm] and the respective value for shear modulus (G) [kPa] regarding aorta 2 static US data sets.

Aorta 2	ΔP [mmHg]	ΔD [mm]	h_0 [mm]	G [kPa]
Static Longitudinal	5-137	10.7 - 15.7	1.373	**92**
Static Cross-section 1	3-138	11.2 - 16.4	1.373	**89**
Static Cross-section 2	2-138	10.8 - 15.9	1.373	**87**

Moreover, the complete mechanical behavior of the aortic tissue was assessed. The stress-strain curves of the different static US data sets were plotted for each aorta. Figure 4.1 reveals the static stress-strain curves for aorta 2.

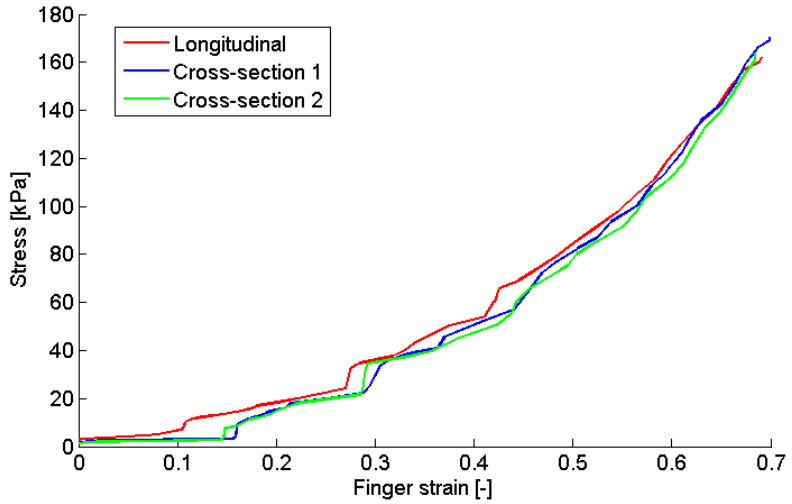

Figure 4.1 – Plot with the stress-strain curves of the different static US-experiments performed in aorta 2. The red curve corresponds to the US longitudinal view, the blue curve to the US cross-sectional view no. 1 and the green curve to the US cross-sectional view no.2. Stress actually refers to the circumferential stress [kPa], whereas strain refers to the Finger strain (dimensionless).

The values for the shear modulus obtained at different locations during static US-measurements are displayed in Figure 4.2 for all aortas. The overall mean value for the shear modulus was 94 ± 16 kPa. The mean values obtained for the shear modulus were 89 ± 23 kPa, 99 ± 12 kPa and 94 ± 11 kPa, for the longitudinal view, cross-sectional view no. 1 and cross-sectional view no. 2, respectively.

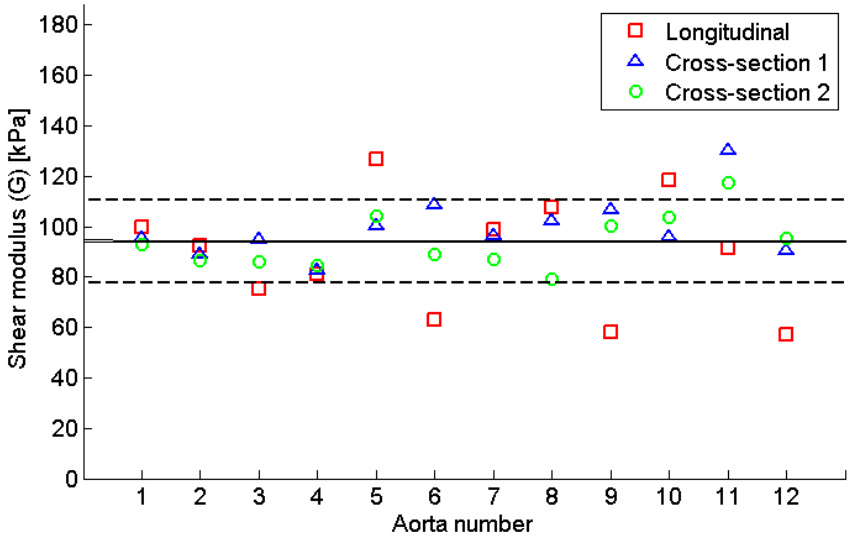

Figure 4.2 – Plot with the values of shear modulus for the twelve aortas obtained from the analysis of static US data sets in the longitudinal view (red squares), cross-section 1 (blue triangles), and cross- section 2 (green circles). The overall mean value of *G* (black solid line) and the overall mean ± standard deviation are also shown (black dashed lines). The overall mean *G* was 94 ± 16 kPa.

Additionally, three paired sample t-tests were performed to compare the means of shear modulus *G* of the different groups (different US imaging planes). No statistically significant difference was found between the mean *G* for static longitudinal and the mean *G* for static cross-section 1 (p=0.20) or between the mean *G* for static longitudinal and the mean *G* for static cross-section 2 (p=0.51). Finally, there was also no significant difference between the mean *G* for static cross-section 1 and the mean *G* for static cross-section 2 (p=0.07).

4.2 Dynamic US-measurements

For each image view, the twelve porcine aortas were also imaged during the dynamic experiment.

Table 4.4 shows the resulting initial wall thickness of the twelve aortas measured in the end-diastolic phase during the dynamic US-experiments. An overall mean initial wall thickness of 1.150 ± 0.088 mm was obtained.

In these experiments, the aim was to get a pressure signal ranging from 80 mmHg to 120 mmHg with a realistic shape. Nonetheless, similarly to what happened with the static US-experiments, the resulting dynamic pressure ranges obtained in Matlab© differed between aortas and within the same aorta. The minimum diastolic pressure was found within the range of 65-81 mmHg, whereas the maximum systolic pressure varied within the range of 127-138 mmHg.

Table 4.4 – The resulting initial wall thickness (h_0) of the twelve porcine aortas obtained from the analysis of the dynamic US data sets.

	Initial wall thickness (h_0) [mm]		Initial wall thickness (h_0) [mm]
Aorta 1	1.158	Aorta 7	1.173
Aorta 2	1.163	Aorta 8	1.246
Aorta 3	1.036	Aorta 9	1.026
Aorta 4	1.095	Aorta 10	1.246
Aorta 5	1.114	Aorta 11	1.041
Aorta 6	1.246	Aorta 12	1.261

As an example, Table 4.5 presents the three input parameters as well as the resulting dynamic shear modulus for the different dynamic US-experiments performed in aorta 2. The respective tables for all aortas are presented in Appendix A2.

Table 4.5 - Diameter range (*ΔD*) [mm], pressure range (*ΔP*) [mmHg], initial wall thickness (h_0) [mm] and the respective value of shear modulus (*G*) [kPa] for aorta 2.

Aorta 2	ΔP [mmHg]	ΔD [mm]	h_0 [mm]	G [kPa]
Dynamic Longitudinal	71-134	14.7 - 16.3	1.163	**255**
Dynamic Cross-section 1	71-134	15.2 - 17.0	1.163	**269**
Dynamic Cross-section 2	72-136	15.0-16.7	1.163	**245**

The values of shear modulus for the different dynamic US-experiments for all aortas are presented in Figure 4.3. In this case, the overall mean of *G* was 250 ± 20 kPa. Concerning each US image view, the mean values obtained for the shear modulus were 247 ± 18 kPa, 259 ± 23 kPa and 245 ± 17 kPa, for longitudinal view, cross-sectional view no. 1 and cross-sectional view no. 2, respectively.

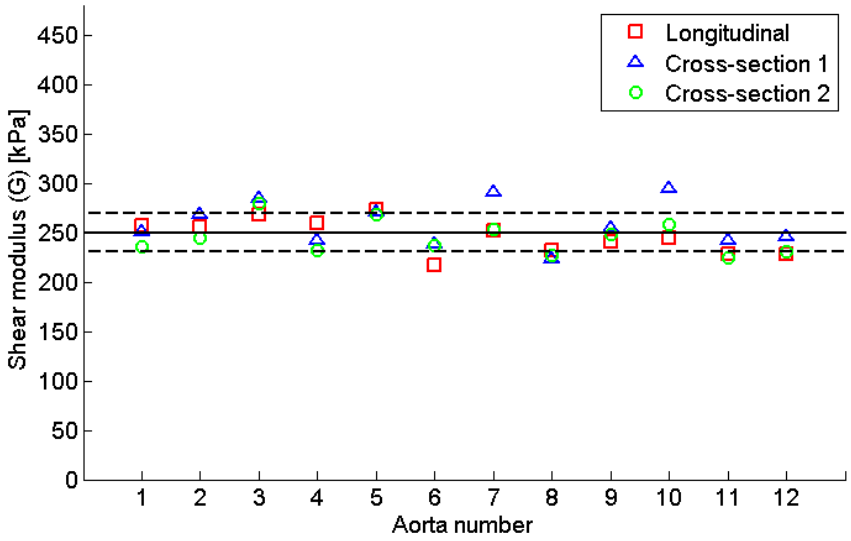

Figure 4.3 - Plot with the dynamic values of shear modulus for all aortas, obtained in the longitudinal view (red squares), cross-section 1 (blue triangles) and cross-section 2 (green circles). The overall mean value of *G* (black solid line) and the overall mean ± standard deviation are also shown (black dashed lines). The overall mean *G* was 250 ± 20 kPa.

Similarly, three paired sample t-tests were performed to compare the means of the shear modulus *G* obtained with different US imaging planes. No statistically significant difference was found between the mean *G* of dynamic longitudinal view and the mean *G* of dynamic cross-section 1 (p=0.05), nor there was a significant difference between the mean *G* of dynamic longitudinal view and the mean *G* of dynamic cross-section 2 (p=0.70). However, it was observed that the mean *G* for cross-section 1 was larger (p=0.01) than that for cross-section 2.

4.3 Incremental shear modulus

An incremental study was performed in each of the twelve aortas, as explained in the Methods chapter. The incremental shear modulus (G_{inc}) was measured as a function of MAP and ΔP. Secondly, for the pressure range matching the in vivo experiment, the incremental modulus was compared to the corresponding dynamic modulus.

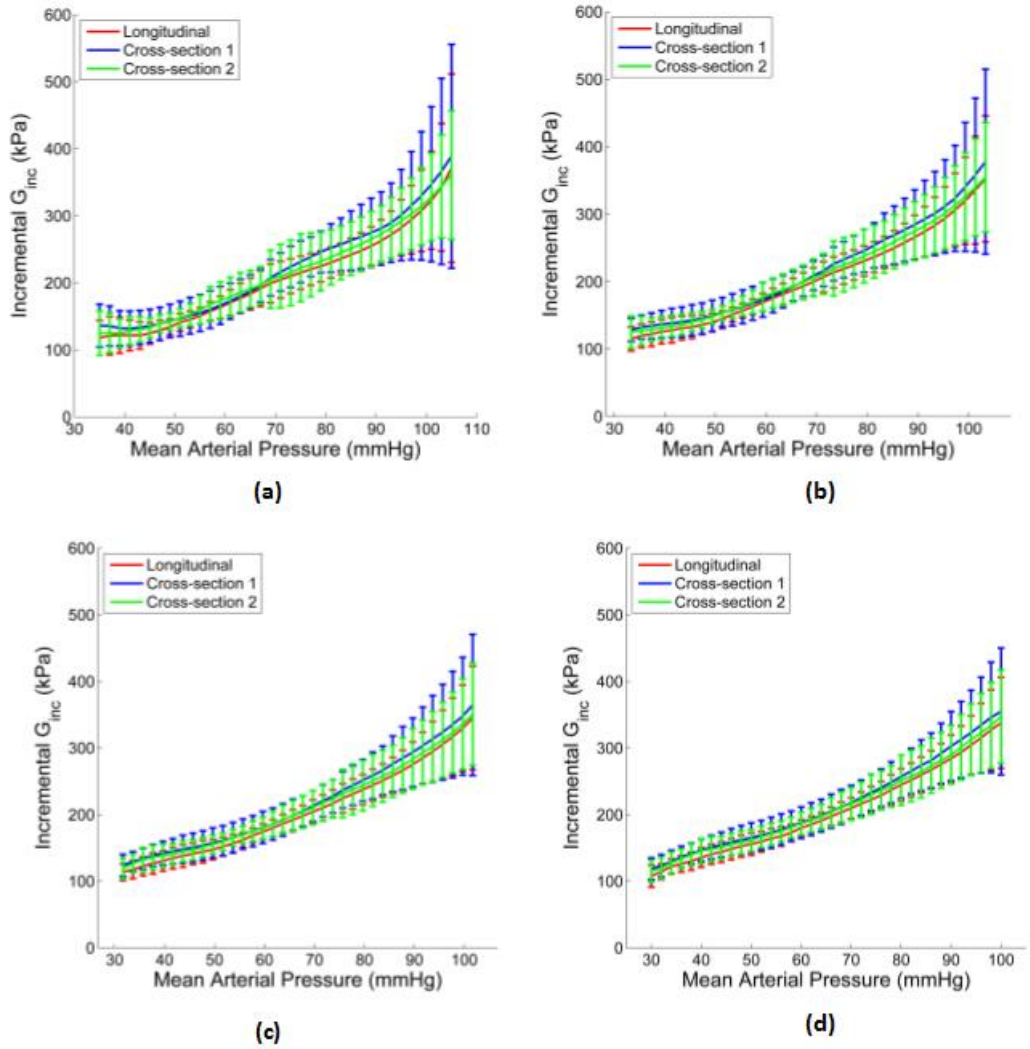

Figure 4.4 - The incremental shear modulus as a function of mean arterial pressure (MAP) for a pulse pressure ΔP of, respectively, 30 mmHg (a), 40 mmHg (b), 50 mmHg (c), and 60 mmHg (d). The red lines indicate the longitudinal view, the green lines correspond to cross-section 1 and the blue lines correspond to cross-section 2. The error-bars indicate the standard deviation of the incremental shear modulus between all aortas.

Figure 4.4 reveals the expected dependency of the shear modulus on the mean arterial pressure. The non-linear behavior of the vascular tissue, and the subsequent linearization by applying the Neo-Hookean model results in an increasing incremental shear modulus. The influence of the chosen pulse pressure is limited, it merely decreases the variation found.

Next, the incremental study was used to verify the results of the dynamic experiments. Table 4.6 shows the three input parameters and the resulting incremental shear modulus for each US image view as obtained in aorta 8. The corresponding tables for all aortas are shown in Appendix A3.

Table 4.6 – Original pressure and diameter arrays (ΔP and ΔD, respectively) obtained from aorta 8 static US data sets. The pressure and diameter arrays corresponding to the dynamic range (ΔP_{dyn} and ΔD_{dyn}, respectively) plus the wall thickness at the diastolic pressure (h_{Pdia}) (columns in blue) were used for the calculation of G_{inc}.

Aorta 8	ΔP [mmHg]	ΔP_{dyn} [mmHg]	ΔD [mm]	ΔD_{dyn} [mm]	h_{Pdia} [mm]	G_{inc} [kPa]
Incremental Longitudinal	5-141	73-132	12.0-16.6	15.0-16.6	1.148	**234**
Incremental Cross-section 1	5-141	71-134	11.6-16.4	14.3-16.2	1.166	**204**
Incremental Cross-section 2	9-142	70-134	10.5-15.9	13.7-15.7	1.100	**211**

An overview of the values of G_{inc} for the different US image views is illustrated in Figure 4.5. The overall mean for all measurements of G_{inc} was 240 ± 39 kPa. In particular, considering each US image view, the mean values obtained for the shear modulus were 235 ± 30 kPa, 246 ± 49 kPa and 241 ± 40 kPa, for the longitudinal view, cross-section 1 and cross-section 2, respectively.

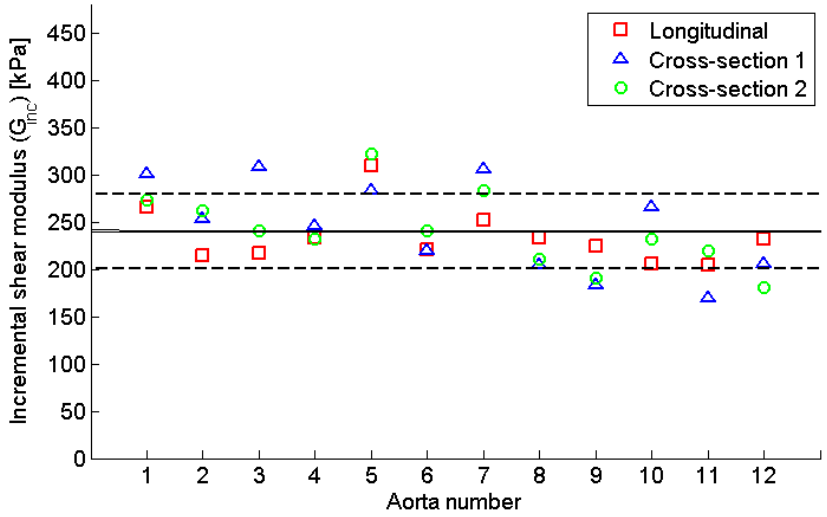

Figure 4.5 - Plot with the values of incremental shear modulus (G_{inc}) for all aortas and all US image views: the longitudinal view (red squares), cross-section 1 (blue triangles) and cross-section 2 (green circles). The overall mean value of G_{inc} (black solid line) and the overall mean ± standard deviation (black dashed lines) are also shown. The overall mean incremental shear modulus was 240 ± 39 kPa.

4.3.1 Incremental G versus Dynamic G

The results found after the analysis of the dynamic US data sets were compared with results obtained from the incremental study (Figure 4.6).

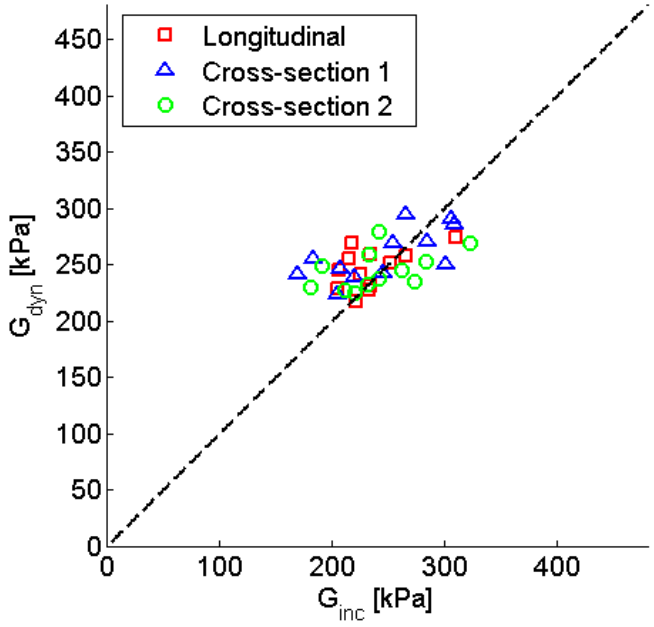

Figure 4.6 – Scatter plot with the correspondence between the values of incremental shear modulus (G_{inc}) and the respective values of dynamic shear modulus (G_{dyn}) considering the same US image view. The red squares correspond to longitudinal view, the blue triangles to cross-section 1 and the green circles to cross-section 2.

Furthermore, a paired-sample t-test showed that there was no statistically significant difference (p=0.07) between the mean *G* obtained from the analysis of the dynamic US data sets (i.e., 250 ± 20 kPa) and the mean *G* obtained from the incremental method (i.e., 240 ± 39 kPa). In addition, a Bland-Altman plot was constructed to analyze the agreement between the dynamic and the incremental analysis results. The difference in shear modulus between these two methods was 10 ± 32 kPa.

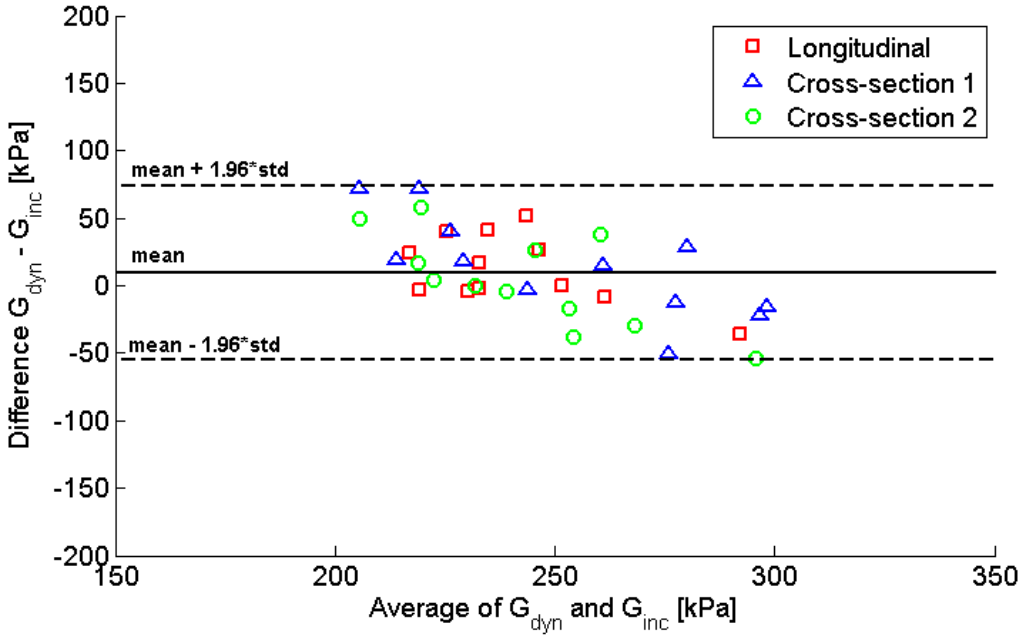

Figure 4.7 – A Bland-Altman plot to compare the values of G obtained using two different methods: the dynamic US-experiment and the incremental analysis. The red squares correspond to longitudinal view, the blue triangles to cross-section 1 and the green circles to cross-section 2. The mean difference in G, i.e., the bias (black solid line) and the mean difference in G ± 1.96 times the standard deviation, the so-called limits of agreement (black dashed lines) are shown as well.

5. Discussion

The aim of this study was to verify and validate vascular elastography using 2D ultrasound in a vascular setting and move towards the translation of this technique into clinical practice. *In vitro* static and dynamic inflation US-experiments were performed to estimate mechanical properties of the aortic tissue. Twelve porcine aortas were tested in a controlled experimental setup and a Neo-Hookean material model was used to calculate the shear modulus *G*. One longitudinal (long axis) and two cross-sectional (short axis) B-mode US recordings were acquired for both static and dynamic US-experiments. Overall mean *G* of 94 ± 16 kPa and 250 ± 20 kPa were obtained from the analysis of static and dynamic US data sets, respectively. Furthermore, an incremental study (indirect analysis) was performed with the purpose of getting insight on the pressure dependency of the estimated incremental shear moduli and comparing the results with those obtained from the dynamic US-experiment (direct analysis) for the same physiological pressure range. A good agreement was found for *G* between these two methods. To our knowledge, this is the first verification of a dynamic US-experiment performed on biological tissue wherein 2D ultrasound elastography was used to provide quantitative information on the biomechanics of the aortic wall, e.g. the shear modulus, for a physiological pressure range.

5.1 Static US-measurements

The stress-strain curves considering the whole pressure range (static stress-strain curves) are consistent with the respective curves obtained in previous studies (Raghavan et al., 1996; Kim et al., 2011; Lopata et al., 2014). From the analysis of the stress-strain curves it is possible to notice

the influence of elastin and collagen in the mechanical behavior of the aortic tissue. Elastin dominates the response at lower pressure levels - causing the elastic recoil of the artery - and collagen gradually starts contributing as the loading increases (Sumner et al., 1970; Kleinstreuer et al., 2007).

An overall mean *G* of 94 ± 16 kPa was found for static US-experiments, which is in agreement with the results found in literature. In a previous study within our group (Lopata et al., 2014), ultrasound elastography was applied to ten porcine aortas during *in vitro* inflation experiments and the results were compared to standard bi-axial tensile testing. In that study, the inflation experiments were performed in a completely different experimental setup. A syringe was used to insert water into the vessel and a glass column was used to measure the hydrostatic pressure, which could be increased from 0 mmHg to 130 mmHg, with a step size of 10 mmHg. An overall shear modulus of 110 ± 11 kPa was found. The higher modulus in that specific study could be explained by the use of water instead of saline solution, leading to swelling of the aorta and thus higher stiffness. In other noteworthy study, Deng et al. (1994) conducted experiments on thoracic aortas of normal rats and found $G = 137 \pm 18$ kPa under physiological conditions (pressure = 120 mmHg; longitudinal stretch = 1.2).

Figure 4.2 shows some outliers. The shear modulus *G* result from the analysis of static longitudinal US data sets of aortas 6, 9 and 12 were found to be considerably lower in comparison with the other static US data sets of the same aorta. It was not clear why these values were so low. A possible explanation is an underestimation of diameters caused by an imperfect position of the US probe (Figure 5.1) or a failure during the vessel tracking. Lower diameters have the effect of lowering the Laplace stress and, as a result, and underestimation of the shear modulus can be obtained.

Longitudinal data of aortas 5 and 10 longitudinal US data sets revealed a shear modulus *G* that was significantly higher compared to the other static US data sets of the same aorta. In these cases, a mismatch of pressure-diameter curves at higher pressures (110 mmHg to 140 mmHg) was observed. This may be related to an inaccurate synchronization of the pressure and diameter curves: the slope of the pressure-diameter curve was higher in that specific region, thus yielding higher values of shear modulus.

Moreover, aorta 11 static cross-section 1 and cross-section 2 US data sets reveal a higher shear modulus in comparison with the shear modulus of the corresponding longitudinal US data set. In this case, a relevant question comes up: which is the outlier? It is possible that the shear modulus

G obtained from the longitudinal US data set is actually the outlier in this case, suggesting that this aorta is stiffer (higher *G*).

Three paired sample t-tests revealed no statistically significant differences between the different groups of static US data sets (longitudinal, cross-section 1 and cross-section 2), suggesting that the three US image views can be used for imaging the aortic wall and thereby provide reliable estimations on the shear modulus of the aortic tissue.

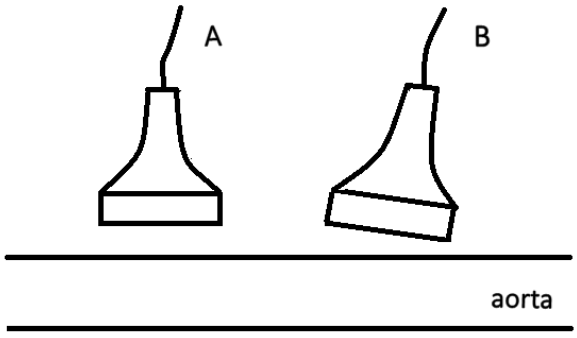

Figure 5.1 - Positioning of the US probe for acquiring longitudinal US images. Situation A (left) shows the correct positioning of the US probe, whereas situation B (right) shows the US probe not perfectly placed. Situation B will lead to an underestimation of the diameter. A similar error can be introduced in the cross-sectional imaging plane.

Overall, with the exception of the aforementioned outliers, all static US-measurements showed a good reproducibility between the different US views.

5.2 Dynamic US-measurements

From the analysis of the dynamic US data sets, an overall mean *G* of 250 ± 20 kPa was obtained. No quantitative information on the shear modulus of the aortic tissue for a physiological/*in vivo* pressure range is available in literature. To our knowledge, this is the first time controlled yet realistic dynamic US-measurements are performed on porcine aortic tissue and ultrasound elastography is used to estimate the respective shear modulus.

Figure 4.3 clearly shows two outliers. A high spread in *G* was found for aorta 7 and aorta 10 dynamic cross-section 1 US data sets. It was not directly clear why those values were so high. Possible reasons could be an inaccurate synchronization of the pressure and diameter curves or a failure during the vessel tracking.

Furthermore, a paired sample t-test showed that the overall mean *G* of the dynamic cross-section 1 data was significantly larger (p=0.01) than the overall mean *G* of the dynamic cross-section 2 data. However, regarding the analogous static US data sets, the difference between the means of *G* was not significant (p=0.07). Thus, a valid and pertinent question may arise: why is there a significant difference in the means of *G* when comparing the dynamic cross-sectional US data sets?

The data of these two groups were acquired in different sites of the aorta. In fact, cross-sectional US image views are more adequate for the estimation of local displacements, which can vary within the aortic segment due to biological variability or to the effect of glue (making the aortic tissue stiffer, i.e., less distensible, in a specific region). Furthermore, cross-sectional data assess the true circumferential behavior, whereas an assumption of rotational axi-symmetry is needed in the longitudinal data. Hence, the analysis of these two US data sets may result in widely dispersed values of shear modulus *G* between the two groups.

Moreover, these differences in the means of *G* could be even more accentuated due to the lower number of data points. For dynamic US-experiments less time frames were acquired, thereby less pressure and diameter data points were obtained comparing to static US-experiments (0 – 140 mmHg), resulting in a more challenging and less precise estimation of *G* using the least-squares fitting.

5.3 Incremental shear modulus

The incremental analysis revealed a huge dependency of incremental shear modulus on mean arterial pressure (MAP). The fact that the ΔP has less influence can be explained in terms of linearization. The MAP determines the work point on the non-linear pressure-diameter curve, or stress-strain curve. ΔP only determines how many data points are taken into account. Therefore, the variation in *G* at higher MAPs becomes larger for larger ΔP. In conclusion, it is of the outmost importance that an accurate pressure measurement is performed *in vivo*. Moreover, it can be discussed whether the shape of the pressure curve is also needed, which is challenging to get *in vivo* in a non-invasive manner, or whether the diastolic and systolic pressures are sufficient.

An overall mean incremental shear modulus of 240 ± 39 kPa was obtained. A high spread in the values of incremental shear modulus was found (Figure 4.5) when compared to the values of shear modulus obtained from the dynamic US-measurements. This could be caused by possible estimation errors when performing linear interpolation on the pressure-diameter and pressure-

wall thickness curves obtained from the analysis of the static US data sets. However, despite these limitations, the incremental shear moduli verify the results from the dynamic 'in vivo' experiment.

An important difference between the two methods is the pressure curves used in each case. It should be noted that the incremental study is performed on data resultant from static US-measurements. For the dynamic US-experiment, a physiological pressure curve mimicking the realistic/*in vivo* situation, was created and applied to the aorta, which resulted in varying strains over the systolic and diastolic phase, whereas for the static US-experiment a pressure curve was used that resulted in uniform steps in strain. Besides, the static US-experiment resulted in more frames than the dynamic US-experiment, yielding more pressure and diameter data points for the estimation of the shear modulus.

However, no significant difference in the values of G was found between the incremental analysis and the dynamic analysis as shown in the paired sample t-test ($p=0.07$), although a slight negative trend was observed in the correlation plot for which we have no explanation (Figure 4.6). However, a good agreement between the two aforementioned methods was shown in the Bland-Altman plot (Figure 4.7). Hence, this result shows that the dynamic US-experiment was verified and the proposed methodology can be used to obtain a reliable estimation of the shear modulus of the aortic wall for a physiological pressure range.

5.4 General limitations

The design of the experimental setup for the *in vitro* US-measurements had several shortcomings. The initial length (L_0) of each aorta was obtained by increasing the longitudinal stretch until the aorta seemed by manual palpation in a stress-free state. Besides, the resulting length was measured using a ruler, which has a limited precision (i.e., 0.5 mm). Taking these two points into account, it is clear that the method to determine L_0 may lack accuracy. An imprecise estimation of L_0 can have an influence on the subsequent calculation of the physiological longitudinal pre-stretch, defined as 1.22 times L_0. In addition, the inaccuracy of this method may also explain the differences found in the resulting shear modulus between aortas. A possible way to overcome this constraint would be measuring the length of the porcine aorta *in vivo* (physiological length) by marking its ends right before the excision of the aorta in the slaughterhouse. However, due to practical limitations, this was not feasible.

The current *in vitro* inflation experiments do profit from the ideal contrast between the vessel and the surrounding physiological saline solution. On the other hand, this also reveals a limitation

of the study, i.e., the lack of surrounding tissue, which will normally constrict movement of the vessel, causing a lower distension of the vessel wall. Additionally, it will result in less contrast in the US images, making the manual segmentation and tracking less accurate.

Moreover, differences in static and dynamic pressure ranges were found between aortas and even within the same aorta, which have an influence in the respective values of shear modulus. These inaccuracies regarding pressure measurements can be related to a possible drift of the pressure sensor, which may have occurred despite multiple calibration.

US-data processing can also lead to inaccuracies. It is well-known (Hansen et al., 2008), and was also observed in this study that cross-sectional US images have poor image quality at 4 and 8 o'clock, causing the manual delineation of the aortic wall to be less reliable in these regions, thus influencing the vessel wall tracking and, as a result, the diameter estimation. Moreover, due to mirroring effect, the RF-data are distorted, resulting in inaccurate displacement estimates.

Several longitudinal and cross-sectional US data sets revealed some translation movement of the aorta, which can also have an impact on the results from the vessel wall tracking. Therefore, automatic segmentation of the aorta can be a more suitable alternative, as it is commonly associated with less noisy pressure-diameter curves and less labor-intensive data processing (Lopata et al., 2014).

The method for determining the initial wall thickness (h_0) manually was found to be very sensitive and prone to errors. The initial wall thickness was estimated considering each of the three different B-mode image views acquired. As a result, three values of the initial wall thickness were obtained for static and dynamic US-measurements, respectively. However, it was observed that a high spread in these values may occur, even within the same group of US data sets (static and dynamic). Therefore, it was decided to calculate the mean of these three values of initial wall thickness for both static and dynamic US-measurements and use these values in the respective US data sets analyses. Nevertheless, even taking the mean value, the errors associated with the estimation of the initial wall thickness are still present and might have an influence on the calculation of the shear modulus. Hence, a more robust method based on automatic image segmentation could give a more precise estimation of the initial wall thickness, thereby providing a more accurate quantification of the shear modulus of the aortic tissue.

It must be also noted that the transducer used, a linear array probe, has excellent resolution due to the equidistant line spacing and relatively high transmit frequency. However, aortic scanning is often performed using a curved array transducer, which operates at lower frequencies

and uses diverging beams to obtain sufficient penetration depth and FOV, respectively. To properly validate the optimal performance of the elastography techniques, one should redo this study with a curved array. Unfortunately, at the start of this study, this specific US probe was not available.

A Neo-Hookean material model was used to describe the material behavior, which is valid for linear-elastic, incompressible and isotropic material subjected to large strains. Nevertheless, the stress-strain curves of the experiments reveal a typical non-linear stress-strain relationship (see Figure 4.1). Besides, aortic tissue is not isotropic, due to specific orientation of collagen fibers (Thubrikar et al., 2001). Hence, a more appropriate material model that better describes the mechanical behavior of the aortic tissue should be used in future research, for instance the non-linear model by Raghavan (1996) or a fiber-reinforced model (Holzapfel et al., 2000).

6. Conclusion

In this study, the performance of 2D ultrasound elastography was investigated and verified in sophisticated mock circulation setups. Results reveal good reproducibility for different hemodynamic conditions and for different US imaging planes. Measurements under physiological conditions (dynamic US-experiments) revealed good performance when compared to a more controlled pressurization (incremental inflation experiments). The dependency on the arterial blood pressure will be a crucial factor in proper assessment of aortic mechanical properties *in vivo*. Future studies will require pathological vessels, the use of non-linear models and the introduction of the proposed methodology into clinical routine.

6.1 Future work

For future experiments, the proposed methodology and experimental setup could also be applied to other vessels. Furthermore, *in vitro* modified porcine aortas could be used with the purpose of mimicking the condition and mechanical behavior of aneurysmal tissue. However, the possibilities of modifying healthy porcine aortas into diseased arteries are yet to be examined.

Additionally, it would be interesting to perform an extension of the current study by including local strain maps, also obtained from the ultrasound RF-data, and used in combination with inverse Finite Element Modelling to obtain specific material properties of the aortic tissue.

The proposed framework could also be attempted with 3D US imaging to get an improved FOV, yet at the expense of a lower temporal resolution (lower frame rate). Hence, this trade-off

in FOV and temporal resolution can be a limiting factor of this technique and thus should be examined in future studies.

A more adequate material model, which assumes anisotropic and non-linear behavior, should be used, yielding more feasible results of *G*. However, the complexity of the non-linear models is strongly limited by the fact that *in vivo* pressure-time data in the lumen of the aorta cannot be acquired non-invasively.

Finally, the main challenge for future research is the incorporation of this technique into established clinical routine. First, patient studies should be performed to investigate the feasibility and reproducibility of this method *in vivo* by: 1) monitoring changes in *G* over time and correlate those with AAA wall weakening, growth and rupture, serving both as a diagnostic and screening tool; 2) comparing local and global differences in *G* to detect possible sites of wall rupture; 3) examine the influence of the incremental shear modulus for varying MAPs and ΔP enabling an extension of this method to a broader range of patient conditions, (e.g. hypertension, hypotension). Therefore, such methodology may have the potential to provide clinicians a non-invasive accurate method to improve AAA risk stratification and enable future screening studies.

7. References

Aldrich J.E. (2007). Basic principles of ultrasound imaging. *Critical Care Medicine, 35*(5 Suppl), S131-S137.

Allaire E., Muscatelli-Groux B., Mandet C., Guinault A.M., Bruneval P., Desgranges P., Clowes A., Méllière D., Becquemin J.P. (2002). Paracrine effect of vascular smooth muscle cells in the prevention of aortic aneurysm formation. *Journal of Vascular Surgery, 36*(5), 1018-1026.

Barua R.S., Ambrose J.A., Eales-Reynolds L.J., DeVoe M.C., Zervas J.G., Saha D.C. (2001). Dysfunctional endothelial nitric oxide biosynthesis in healthy smokers with impaired endothelium-dependent vasodilatation. *Circulation, 104*(16), 1905-1910.

Bengtsson H., Sonesson B., Bergqvist D. (1996). Incidence and prevalence of abdominal aortic aneurysms, estimated by necropsy studies and population screening by ultrasound. *Annals of the New York Academy of Sciences, 800*, 1-24.

Bercoff J., Tanter M., Fink M. (2004). Supersonic shear imaging: a new technique for soft tissue elasticity mapping. *IEEE Transactions on Ultrasonics, Ferroelectrics, and Frequency Control, 51*(4), 396-409.

Bland J.M., Altman D.G. (1986). Statistical methods for assessing agreement between two methods of clinical measurement. *Lancet, 1*(8476), 307-310.

Bohs L.N,, Trahey G.E. (1991). A novel method for angle independent ultrasonic imaging of blood flow and tissue motion. *IEEE Transactions on Biomedical Engineering, 38*(3), 280-286.

Brekken R., Bang J., Ødegård A., Aasland J., Hernes T.A., Myhre H.O. (2006). Strain estimation in abdominal aortic aneurysms from 2-D ultrasound. *Ultrasound in Medicine and Biology, 32*(1), 33-42.

Brown L.C., Powell J.T. (1999). Risk factors for aneurysm rupture in patients kept under ultrasound surveillance. UK Small Aneurysm Trial Participants. *Annals of Surgery, 230*(3), 289-297.

Bush R.L., Lin P.H., Lumsden A.B. (2003). Endovascular management of abdominal aortic aneurysms. *Journal Cardiovascular Surgery (Torino), 44*(4), 527-534.

Callanan A., Davis N.F., Walsh M.T., McGloughlin T.M. (2011). Tissue-Engineered Extracellular Matrices (ECMs) as Adjuvant Scaffolds for Endovascular Repair (EVAR). In E. D. (Ed), *Regenerative Medicine and Tissue-Engineering - Cells and Biomaterials* (pp. 301-322). Rijecka, Croatia: Intech Europe.

Campa J.S., Greenhalgh R.M., Powell J.T. (1987). Elastin degradation in abdominal aortic aneurysms. *Atherosclerosis, 65*(1-2), 13-21.

Carew T.E., Vaishnav R.N., Patel D.J. (1968). Compressibility of the arterial wall. *Circulation Research, 23*(1), 61-68.

Choksy S.A., Wilmink A.B., Quick C.R. (1999). Ruptured abdominal aortic aneurysm in the Huntingdon district: a 10-year experience. *Annals of the Royal College of Surgeons of England, 81*(1), 27-31.

Conway K.P., Byrne J., Townsend M., Lane I.F. (2001). Prognosis of patient turned down for conventional abdominal aortic aneurysm repair in the endovascular and sonographic era: Szilagyi revisited? *Journal of Vascular Surgery, 33*(4), 752-757.

Cox R.H. (1978). Passive mechanics and connective tissue composition of canine arteries. *Journal of Physiology-Heart and Circulatory Physiology, 234*(5), H533-H541.

Cox R.H. (1979). Regional, species, and age related variations in the mechanical properties of arteries. *Biorheology, 16*(1-2), 85-94.

Crosby J., Amundsen B.H., Hergum T., Remme E.W., Langeland S., Torp H. (2009). 3-D speckle tracking for assessment of regional left ventricular function. *Ultrasound in Medicine and Biology, 35*(3), 458-471.

Darling R.C., Messina C.R., Brewster D.C., Ottinger L.W. (1977). Autopsy study of unoperated abdominal aortic aneurysms. *Circulation, 56*(2 Suppl), 161-164.

de Korte C.L., Pasterkamp G., van der Steen A.F., Woutman H.A., Bom N. (2000). Characterization of plaque components with intravascular ultrasound elastography in human femoral and coronary arteries in vitro. *Circulation, 102*(6), 617-623.

de Korte C.L., Sierevogel M.J., Mastik F., Strijder C., Schaar J.A., Velema E., Pasterkamp G., Serruys P.W., van der Steen A.F.M. (2002). Identification of atherosclerotic plaque components with intravascular ultrasound elastography in vivo: a Yucatan Pig Study. *Circulation, 105*(14), 1627-1630.

Deng S.X., Tomioka J., Debes J.C., Fung Y.C. (1994). New experiments on shear modulus of elasticity of arteries. *American Journal of Physiology, 266*(1 Pt 2), H1-H10.

DeWall R.J. (2013). Ultrasound elastography: principles, techniques, and clinical applications. *Critical Reviews on Biomedical Engineering, 41*(1), 1-19.

Dobrin P.B. (1978). Mechanical properties of arteries. *Physiological Reviews, 58*(2), 397-460.

Dobrin P.B., Mrkvicka R. (1994). Failure of elastin or collagen as possible critical connective tissue alterations underlying aneurysmal dilatation. *Cardiovascular Surgery, 2*(4), 484-488.

Edler I., Lindström K. (2004). The history of echocardiography. *Ultrasound in Medicine and Biology, 30*(12), 1557-1712.

Emelianov S.Y., Lubinski M.A., Weitzel W.F., Wiggins R.C., Skovoroda A.R., O'Donnell M. (1995). Elasticity imaging for early detection of real pathology. *Ultrasound in Medicine and Biology, 21*(7), 871-883.

Evans A., Whelehan P., Thomson K., McLean D., Brauer K., Purdie C., Jordan L., Baker L., Thompson A. (2010). Quantitative shear wave ultrasound elastography: initial experience in solid breast masses. *Breast Cancer Research, 12*(6), R104.

Fillinger M.F., Marra S.P., Raghavan M.L., Kennedy F.E. (2003). Prediction of rupture risk in abdominal aortic aneurysm during observation: wall stress versus diameter. *Journal of Vascular Surgery, 37*(4), 724-732.

Fillinger M.F., Raghavan M.L., Marra S.P., Cronenwett J.L., Kennedy F.E. (2002). In vivo analysis of mechanical wall stress and abdominal aortic aneurysm rupture risk. *Journal of Vascular Surgery, 36*(3), 589-597.

Fontaine V., Jacob M.P., Houard X., Rossignol P., Plissonnier D., Angles-Cano E., Michel J.B. (2002). Involvement of the mural thrombus as a site of protease release and activation in human aortic aneurysms. *American Journal of Pathology, 161*(5), 1701-1710.

Fung Y.C. (1993). Mechanical properties and active remodeling of blood vessels. In *Biomechanics: Mechanical properties of living tissues* (2nd ed., pp. 321-391). New York: Springer-Verlag.

Fung Y.C., Fronek K., Patitucci P. (1979). Pseudoelasticity of arteries and the choice of its mathematical expression. *American Journal of Physiology, 237*(5), H620-H631.

Golemati S., Sassano A., Lever M.J., Bharath A.A., Dhanjil S., Nicolaides A.N. (2003). Carotid artery wall motion estimated from B-mode ultrasound using region tracking and block matching. *Ultrasound in Medicine and Biology, 29*(3), 387-399.

Golledge J., Muller J., Daugherty A., Norman P. (2006). Abdominal Aortic Aneurysm: Pathogenesis and Implications for Management. *Arteriosclerosis, Thrombosis, and Vascular Biology, 26*(12), 2605-2613.

Greenhalgh R.M., Brown L.C., Kwong G.P., Powell J.T., Thompson S.G., EVAR trial participants. (2004). Comparison of endovascular aneurysm repair with open repair in patients with abdominal aortic aneurysm (EVAR trial 1), 30-day operative mortality results: randomised controlled trial. *Lancet, 364*(9437), 843-848.

Greenhalgh R.M., Forbes J.F., Fowkes F.G., Powel J.T., Ruckley C.V., Brady A.R., Brown L.C., Thompson S.G. (1998). Early elective open surgical repair of small abdominal aortic aneurysms is not recommended: results of the UK Small Aneurysm Trial. *European Journal of Vascular and Endovascular Surgery, 16*(6), 462-464.

Guo X., Lanir Y., Kassab G.S. (2007). Effect of osmolarity on the zero-stress state and mechanical properties of the aorta. *American Journal of Physiology. Heart and Circulatory Physiology, 293*(4), H2328-H2334.

Guy C., Ffytche D. (2005). *Introduction to the principles of medical imaging* (Revised ed.). London: Imperial College Press.

Hall A.J., Busse E.F., McCarville D.J., Burgess J.J. (2000). Aortic wall tension as a predictive factor for abdominal aortic aneurysm rupture: improving the selection of patients for abdominal aortic aneurysm repair. *Annals of Vascular Surgery, 14*(2), 152-157.

Hallett J.W., Marshall D.M., Petterson T.M., Gray D.T., Bower T.C., Cherry K.T., Gloviczki P., Pairolero P.C. (1997). Graft-related complications after abdominal aortic aneurysm repair: reassurance from a 36-year population-based experience. *Journal of Vascular Surgery, 25*(2), 277-286.

Hansen H.H.G., Lopata R.G.P., Holewijn S., Truijers M., de Korte C.L. (2008). Non-invasive vascular ultrasound strain imaging: different arteries, different approaches. *IFMBE Proceedings: 4th European Conference of the International Federation for Medical and Biological Engineering, 22,* pp. 298-302. Antwerp, Belgium.

Harter L.P., Gross B.H., Callen P.W., Barth R.A. (1982). Ultrasonic evaluation of abdominal aortic thrombus. *Journal of Ultrasound in Medicine, 1*(8), 315-318.

He C.M., Roach M.R. (1994). The composition and mechanical properties of abdominal aortic aneurysms. *Journal of Vascular Surgery, 20*(1), 6-13.

Heimdal A., Støylen A., Torp H., Skjaerpe T. (1998). Real-time strain rate imaging of the left ventricle by ultrasound. *Journal of the American Society of Echocardiography, 11*(11), 1013-1019.

Hendee W.R., Ritenour E.R. (2002). *Medical Imaging Physics* (4th ed.). New York: Wiley-Liss.

Holzapfel G.A., Gasser T.C., Ogden R.W. (2000). A new constitutive framework for arterial wall mechanics and a comparative study of material models. *Journal of elasticity and the physical science of solids, 64*(1-3), 1-48.

Holzapfel G.A., Gasser T.C., Stadler M. (2002). A structural model for the viscoelastic behavior of arterial walls: continuum formulation and finite element analysis. *European Journal of Mechanics A/Solids, 21*(3), 441-463.

Horny L., Adamek T., Vesely J., Chlup H., Zitay R., Konvickova S. (2012). Age-related distribution of longitudinal pre-strain in abdominal aorta with emphasis on forensic application. *Forensic Science International, 214*(1-3), 18-22.

Humphrey, J.D. (2002). *Cardiovascular Solid Mechnanics: Cells , Tissues and Organs* (2nd ed.). New York: Springer-Verlag.

Imura T., Yamamoto K., Kanamori K., Mikami T., Yasuda H. (1986). Non-invasive ultrasonic measurement of the elastic properties of the human abdominal aorta. *Cardiovascular Research, 20*(3), 208-214.

Jongen G. (2011). *Mechanical characterization and imaging of healthy aortas and abdominal aortic aneurysms with 2D ultrasound.* MSc Thesis, Eindhoven University of Technology, The Netherlands.

Khaled W., Reichling S., Bruhns O.T., Ermert H. (2006). Ultrasonic strain imaging and reconstructive elastography for biological tissue. *Ultrasonics, 44*(Suppl 1), 199-202.

Kim B., Lee S.B., Lee J., Cho S., Park H., Yeom S., Park S.H. (2012). A comparison among Neo-Hookean model, Mooney-Rivlin model, and Ogden model for chloroprene rubber. *International Journal of Precision Engineering and Manufacturing, 13*(5), 759-764.

Kim J., Baek S. (2011). Circumferential variations of mechanical behavior of the porcine thoracic aorta during the inflation test. *Journal of Biomechanics, 44*(10), 1941-1947.

Kim K., Weitzel W.F., Rubin J.M., Xie H., Chen X., O'Donnell M. (2004). Vascular intramural strain imaging using arterial pressure equalization. *Ultrasound in Medicine and Biology, 30*(6), 761-771.

Klabunde R.E. (2005). *Cardiovascular Physiology Concepts.* Philadelphia: Lippincott Williams & Wilkins.

Kleinstreuer C., Li Z., Farber M.A. (2007). Fluid-structure interaction analyses of stented abdominal aortic aneurysms. *Annual Review of Biomedical Engineering, 9*, 169-204.

Kniemeyer H.W., Kessler T., Reber P.U., Ris H.B., Hakki H., Widmer M.K. (2000). Treatment of ruptured abdominal aortic aneurysm, a permanent challenge or a waste of resources? Prediction of outcome using a multi-organ dysfunction score. *European Journal of Vascular and Endovascular Surgery, 19*(2), 190-196.

Konofagou E., Ophir J. (1998). A new elastographic method for estimation and imaging of lateral displacements, lateral strains, corrected axial strains and Poisson's ratios in tissues. *Ultrasound in Medicine and Biology, 24*(8), 1183-1199.

Kramer C.M., Cecilli L.A., Hagspiel K., DiMaria J.M., Epstein F.H., Kern J.A. (2004). Magnetic resonance imaging identifies the fibrous cap in atherosclerotic abdominal aortic aneurysm. *Circulation, 109*(8), 1016-1021.

Krouskop T.A., Wheeler T.M., Kallel F., Garra B.S., Hall T. (1998). Elastic moduli of breast and prostate tissues under compression. *Ultrasonic Imaging, 20*(4), 260-274.

Kurvers H., Veith F.J., Lipsitz E.C., Ohki T., Gargiulo N.J., Cayne N.S., Suggs W.D., Timaran C.H., Kwon G.Y., Rhee S.J., Santiago C. (2004). Discontinuous, staccato growth of abdominal aortic aneurysms. *Journal of the American College of Surgeons, 199*(5), 709-715.

Lawrence J.P. (2007). Physics and instrumentation of ultrasound. *Critical Care Medicine, 35*(8 Suppl), S314-S322.

Lederle F.A., Johnson G.R., Wilson S.E., Chute E.P., Littooy F.N., Bandyk D., Kruspski W.C., Barone G.W., Acher C.W., Ballard D.J. (1997). Prevalence and associations of abdominal aortic aneurysm detected through screening. *Annals of Internal Medicine, 126*(6), 441-449.

Lee J.K., Ling D., Hieken J.P., Glazer H.S., Sicard G.A., Totty W.G., Levitt R.G., Murphy W.A. (1984). Magnetic resonance imaging of abdominal aortic aneurysms. *American Journal of Roentgenology, 143*(6), 1197-1202.

Leung D.Y., Glagov S., Mathews M.B. (1976). Cyclic stretching stimulates synthesis of matrix components by arterial smooth muscle cells in vitro. *Science, 191*(4226), 475-477.

Lindholt J.S., Vammen S., Juul S., Henneberg E.W., Fasting H. (1999). The validity of ultrasonographic scanning as screening method for abdominal aortic aneurysm. *European Journal of Vascular and Endovascular Surgery, 17*(6), 472-475.

Long A., Rouet L., Bissery A., Rossignol P., Mouradian D., Sapoval M. (2004). Compliance of abdominal aortic aneurysms: evaluation of tissue Doppler imaging. *Ultrasound in Medicine and Biology, 30*(9), 1099-1108.

Longo G.M., Xiong W., Greiner T.C., Zhao Y., Fiotti N., Baxter B.T. (2002). Matrix metalloproteinases 2 and 9 work in concert to produce aortic aneurysms. *Journal of Clinical Investigation, 110*(5), 625-632.

Lopata R.G.P. (2010). *2D and 3D Ultrasound Strain Imaging: Methods and in vivo applications.* PhD Thesis, Raboud University Nijmegen, The Netherlands.

Lopata R.G.P., Nillesen M.M., Gerrits I.H., Hansen H.H.G., Kapusta L., Thijssen J.M., de Korte C.L. (2008). 3D Cardiac Strain Imaging using a Novel Tracking Method. *IFMBE Proceedings 22: 4th European Conference of the International Federation for Medical and Biological Engineering*, (pp. 697-700). Antwerp, Belgium.

Lopata R.G.P., Nillesen M.M., Hansen H.H., Gerrits I.H., Thijssen J.M., de Korte C.L. (2009). Performance evaluation of methods for two-dimensional displacement and strain estimation using ultrasound radio frequency data. *Ultrasound in Medicine and Biology, 35*(5), 796-812.

Lopata R.G.P., Nillesen M.M., Thijssen J.M., Kapusta L., de Korte C.L. (2011). Three-dimensional cardiac strain imaging in healthy children using RF-data. *Ultrasound in Medicine and Biology, 37*(9), 1399-1408.

Lopata R.G.P., Peters M.F.J., Nijs J., Oomens C.W.J., Rutten M.C.M., van de Vosse F.N. (2014). Vascular Elastography: a Validation Study. *Ultrasound in Medicine and Biology, 40*(8), 1882-1895.

López-Candales A., Holmes D.R., Liao S., Scott M.J., Wickline S.A., Thompson R.W. (1997). Decreased vascular smooth muscle cell density in medial degeneration of human abdominal aortic aneurysms. *American Journal of Pathology, 150*(3), 993-1007.

MacSweeney S.T., Ellis M., Worrell P.C., Greenhalgh R.M., Powell J.T. (1994). Smoking and growth rate of small abdominal aortic aneurysms. *Lancet, 344*(8923), 651-652.

Mendis S., Puska P. , Norving B. (2011). *Global Atlas on cardiovascular Disease.* Geneva: World Health Organization.

Nicholls S.C., Gardner J.B., Meissner M.H., Johansen H.K. (1998). Rupture in small abdominal aortic aneurysms. *Journal of Vascular Surgery, 28*(5), 884-888.

Ophir J., Alam S.K., Garra B., Kallel F., Konofagou E., Krouskop T., Varghese T. (1999). Elastography: ultrasonic estimation and imaging of the elastic properties of tissues. *Proceedings of the Institution of Mechanical Engineers - Part H. Journal of engineering in medicine, 213*(3), 203-233.

Ophir J., Céspedes I., Ponnekanti H., Yazdi Y., Li X. (1991). Elastography: a quantitative method for imaging the elasticity of biological tissues. *Ultrasonic Imaging, 13*(2), 111-134.

Otto F. (1899). Die Grundform des arteriellen Pulses. *Zeitschrift für Biologie, 37*, 483-526.

Parodi J.C., Palmaz J.C., Barone H.D. (1991). Transfemoral intraluminal graft implantation for abdominal aortic aneurysms. *Annals of Vascular Surgery, 5*(6), 491-499.

Patel D.J., Fry D.L. (1969). The elastic symmetry of arterial segments in dogs. *Circulation Research, 24*(1), 1-8.

Peters M.F.J. (2013). *Mechanical characterization of ascending thoracic aortic aneurysms using ultrasound: experimental validation and preliminary in vivo experience.* MSc Thesis, Eindhoven University of Technology, The Netherlands.

Peters M.F.J., Lopata R.G.P., van de Vosse F.N., Rutten M.C.M. (July 2014). Ex Vivo Determination of the Physiological Axial Pre-stretch of Porcine Aortas. *Poster session presented at: World Congress of Biomechanics.* Boston (MA, USA).

Prinssen M., Verhoeven E.L., Buth J., Cuypers P.W., van Sambeek M.R., Balm R., Buskens E., Grobbee D.E., Blankensteijn J.D., Dutch Randomized Endovascular Aneurysm Management (DREAM) Trial Group. (2004). A randomized trial comparing conventional and endovascular repair of abdominal aortic aneurysms. *The New England Journal of Medicine, 351*(16), 1607-1618.

Raghavan M.L., Kratzberg J.A., Golzarian J. (2005). Introduction to biomechanics related to endovascular repair of abdominal aortic aneurysm. *Techniques in vascular and interventional radiology, 8*(1), 50-55.

Raghavan M.L., Vorp D.A., Federle M.P., Makaroun M.S., Webster M.W. (2000). Wall stress distribution on three-dimensionally reconstructed models of human abdominal aortic aneurysm. *Journal of Vascular Surgery, 31*(4), 760-769.

Raghavan M.L., Webster M.W., Vorp D.A. (1996). Ex vivo biomechanical behavior of abdominal aortic aneurysm: assessment using a new mathematical model. *Annals of Biomedical Engineering, 24*(5), 573-582.

Rivlin R.S. (1948). Large elastic deformations of isotropic materials. IV. Further developments of the general theory. *Philosophical Transactions of the Royal Society A: Mathematical, Physical and Engineering Sciences, 241*(835), 379-397.

Roach M.R., Burton A.C. (1959). The effect of age on the elasticity of human iliac arteries. *Canadian Journal of Biochemistry and Physiology, 37*(4), 557-570.

Sacks M.S. (2000). Biaxial mechanical evaluation of planar biological materials. *Journal of Elasticity and the Physical Science of Solids, 61*(1-3), 199-246.

Sakalihasan N., Limet R., Defawe O.D. (2005). Abdominal aortic aneurysm. *Lancet, 365*(9470), 1577-1589.

Satta J., Juvonen T., Haukipuro K., Juvonen M., Kairaluoma M.I. (1995). Increased turnover of collagen in abdominal aortic aneurysms, demonstrated by measuring the concentration of the aminoterminal propeptide of type III procollagen in peripheral and aortal blood samples. *Journal of Vascular Surgery, 22*(2), 155-160.

Schulze-Bauer C.A., Mörth C., Holzapfel G.A. (2003). Passive biaxial mechanical response of aged human iliac arteries. *Journal of Biomechanical Engineering, 125*(3), 395-406.

Scott R.A., Ashton H.A., Kay D.N. (1991). Abdominal aortic aneurysm in 4237 screened patients: prevalence, development and management over 6 years. *British Journal of Surgery, 78*(9), 1122-1125.

Singh K., Bønaa K.H., Solberg S., Sørlie D.G., Bjørk L. (1998). Intra- and interobserver variability in ultrasound measurements of abdominal aortic diameter. The Tromsø Study. *European Journal of Vascular and Endovascular Surgery, 15*(6), 497-504.

Smeltzer S.C., Bare B.G., Hinkle J.L., Cheever K.H. (2010). *Brunner & Suddarth's Textbook of Medical-Surgical Nursing* (12th edition ed.). Philadelphia: Lippincott Williams & Wilkins.

Speelman L. (2009). *Biomechanical Analysis for Abdominal Aortic Aneurysm Risk Stratification.* PhD Thesis, Maastricht University Medical Center, The Netherlands.

Speelman L., Hellenthal F., Pulinx B., Bosboom E.M., Breeuwer M., van Sambeek M.R., van de Vosse F.N., Jacobs M.J., Wodzig W.K., Schurink G. (2010). The influence of wall stress on aaa growth and biomarkers. *European Journal of Vascular and Endovascular Surgery, 39*(4), 410-416.

Sumner D.S., Hokanson D.E., Strandness D.E. Jr. (1970). Stress-strain characteristics and collagen-elastin content of abdominal aortic aneurysms. *Surgery, gynecology & obstetrics, 130*(3), 459-466.

Thompson R.W., Parks W.C. (1996). Role of matrix metalloproteinases in abdominal aortic aneurysms. *Annals of the New York Academy of Sciences, 800*, 157-174.

Thubrikar M.J., al-Soudi J., Robicsek F. (2001). Wall stress studies of abdominal aortic aneurysm in a clinical model. *Annals of Vascular Surgery, 15*(3), 355-366.

Truijers M., Pol J.A., Schultzekool L.J., van Sterkenburg S.M., Fillinger M.F., Blankensteijn J.D. (2007). Wall stress analysis in small asymptomatic, symptomatic and ruptured abdominal aortic aneurysms. *European Journal of Vascular and Endovascular Surgery, 33*(4), 401-407.

Vallabhaneni S.R., Gilling-Smith G.L., How T.V., Carter S.D., Brennan J.A., Harris P.L. (2004). Heterogeneity of tensile strength and matrix metalloproteinase activity in the wall of abdominal aortic aneurysms. *Journal of Endovascular Therapy, 11*(4), 494-502.

van den Broek C.N., van der Horst A., Rutten M.C.M., van de Vosse F.N. (2011). A generic constitutive model for the passive porcine coronary artery. *Biomechanics and Modelling in Mechanobiology, 10*(2), 249-258.

Vande Geest J.P., Sacks M.S., Vorp D.A. (2006). The effects of aneurysm on the biaxial mechanical behavior of human abdominal aorta. *Journal of Biomechanics, 39*(7), 1324-1334.

Vardulaki K.A., Walker N.M., Day N.E., Duffy S.W., Ashton H.A., Scott R.A. (2000). Quantifying the risks of hypertension, age, sex and smoking in patients with abdominal aortic aneurysm. *British Journal of Surgery, 87*(2), 195-200.

Venkatasubramaniam A.K., Fagan M.J., Mehta T., Mylankal K.J., Ray B., Kuhan G., Chetter I.C., McCollum P.T. (2004). A comparative study of aortic wall stress using finite element analysis for ruptured and non-ruptured abdominal aortic aneurysms. *European Journal of Vascular and Endovascular Surgery, 28*(2), 168-176.

Vorp D.A., Lee P.C., Wang D.H., Makaroun M.S., Nemoto E.M., Ogawa S., Webster M.W. (2001). Association of intraluminal thrombus in abdominal aortic aneurysm with local hypoxia and wall weakening. *Journal of Vascular Surgery, 34*(2), 291-299.

Vorp D.A., Raghavan M.L., Muluk S.C., Makaroun M.S., Steed D.L., Shapiro R., Webster M.W. (1996). Wall strength and stiffness of aneurysmal and nonaneurysmal abdominal aorta. *Annals of the New York Academy of Sciences, 800*, 274-276.

Vorp D.A., Raghavan M.L., Webster M.W. (1998). Mechanical wall stress in abdominal aortic aneurysm: influence of diameter and asymetry. *Journal of Vascular Surgery, 27*(4), 632-639.

Westerhof N., Bosman F., De Vries C.J., Noordergraaf A. (1969). Analog studies of the human systemic arterial tree. *Journal of Biomechanics, 2*(2), 121-143.

Weyman A.E. (1994). Physical principles of ultrasound. In *Principles and Practice of Echocardiography* (2nd ed., pp. 29-55). Philadelphia: Lea & Febiger.

Wills A., Thompson M.M., Crowther M., Sayers R.D., Bell P.R.F. (1996). Pathogenesis of abdominal aortic aneurysms - cellular and biochemical mechanisms. *European Journal Vascular and Endovascular Surgery, 12*(4), 391-400.

Wilmink A.B., Quick CG. (1998). Epidemiology and potential for prevention of abdominal aortic aneurysms. *British Journal of Surgery, 85*(2), 155-162.

Wilmink T.M.B., Quick C.R.G., Day N.E. (1999). The association between cigarette smoking and abdominal aortic aneurysms. *Journal of Vascular Surgery, 30*(6), 1099-1105.

Wilson K.A., Lee A.J., Hoskins P.R., Fowkes F.G., Ruckley C.V., Bradbury A.W. (2003). The relationship between aortic wall distensibility and rupture of infrarenal abdominal aortic aneurysm. *Journal of Vascular Surgery, 37*(1), 112-117.

Wilson K.A., Whyman M., Hoskins P.R., Lee A.J., Bradbury A.W., Fowkes F.G., Ruckley C.V. (1999). The relationship between abdominal aortic aneurysm wall compliance, maximum diameter and growth rate. *Cardiovascular Surgery, 7*(2), 208-213.

Xiong J., Wang S.M., Zhou W., Wu J.G. (2008). Measurement and analysis of ultimate mechanical properties, stress-strain curve fit, and elastic modulus formula of human abdominal aortic aneurysm and nonaneurysmal abdominal aorta. *Journal of Vascular Surgery, 48*(1), 189-195.

Zankl A.R., Schumacher H., Krumsdorf U., Katus H.A., Jahn L., Tiefenbacher C.P. (2007). Pathology, natural history and treatment of abdominal aortic aneurysms. *Clinical Research in Cardiology, 96*(3), 140-151.

Appendix

A. Additional Tables

A1. Static US-experiments

Aorta 1	ΔP [mmHg]	ΔD [mm]	h_0 [mm]	G [kPa]
Static Longitudinal	3-141	12.3-17.3	1.4956	**100**
Static Cross-section 1	0-141	12.6-18.4	1.4956	**95**
Static Cross-section 2	0-140	12.0-140	1.4956	**93**

Aorta 2	ΔP [mmHg]	ΔD [mm]	h_0 [mm]	G [kPa]
Static Longitudinal	5-137	10.7 - 15.7	1.373	**92**
Static Cross-section 1	3-138	11.2 - 16.4	1.373	**89**
Static Cross-section 2	2-138	10.8 - 15.9	1.373	**87**

Aorta 3	ΔP [mmHg]	ΔD [mm]	h_0 [mm]	G [kPa]
Static Longitudinal	4-137	10.4-17.2	1.391	**75**
Static Cross-section 1	3-138	12.5-18.6	1.391	**95**
Static Cross-section 2	3-137	11.3-17.3	1.391	**86**

Aorta 4	ΔP [mmHg]	ΔD [mm]	h_0 [mm]	G [kPa]
Static Longitudinal	6-142	10.1-15.8	1.320	**81**
Static Cross-section 1	6-144	10.5-16.7	1.320	**83**
Static Cross-section 2	6-143	10.2-15.8	1.320	**85**

Aorta 5	ΔP [mmHg]	ΔD [mm]	h_0 [mm]	G [kPa]
Static Longitudinal	2-141	12.5-17.1	1.290	**127**
Static Cross-section 1	2-140	11.8-17.6	1.290	**100**
Static Cross-section 2	3-141	12.0-18.0	1.290	**104**

Aorta 6	ΔP [mmHg]	ΔD [mm]	h_0 [mm]	G [kPa]
Static Longitudinal	4-142	9.6-16.4	1.422	**63**
Static Cross-section 1	3-140	11.5-15.8	1.422	**109**
Static Cross-section 2	4-139	10.4-14.3	1.422	**89**

Aorta 7	ΔP [mmHg]	ΔD [mm]	h_0 [mm]	G [kPa]
Static Longitudinal	1-138	12.6-17.4	1.584	**99**
Static Cross-section 1	2-138	12.5-17.5	1.584	**96**
Static Cross-section 2	1-137	11.9-16.9	1.584	**87**

Aorta 8	ΔP [mmHg]	ΔD [mm]	h_0 [mm]	G [kPa]
Static Longitudinal	5-141	12.0-16.6	1.437	**108**
Static Cross-section 1	5-141	11.6-16.4	1.437	**102**
Static Cross-section 2	9-142	10.5-15.9	1.437	**79**

Aorta 9	ΔP [mmHg]	ΔD [mm]	h_0 [mm]	G [kPa]
Static Longitudinal	8-143	8.2-16.2	1.290	**58**
Static Cross-section 1	10-145	11.2-17.2	1.290	**107**
Static Cross-section 2	11-144	10.6-16.1	1.290	**100**

Aorta 10	ΔP [mmHg]	ΔD [mm]	h_0 [mm]	G [kPa]
Static Longitudinal	1-135	11.9-15.8	1.494	**118**
Static Cross-section 1	1-138	11.7-16.6	1.494	**96**
Static Cross-section 2	1-137	12.1-16.8	1.494	**104**

Aorta 11	ΔP [mmHg]	ΔD [mm]	h_0 [mm]	G [kPa]
Static Longitudinal	11-136	10.1-15.6	1.290	**91**
Static Cross-section 1	10-135	11.3-15.8	1.290	**130**
Static Cross-section 2	9-135	10.9-14.7	1.290	**117**

Aorta 12	ΔP [mmHg]	ΔD [mm]	h_0 [mm]	G [kPa]
Static Longitudinal	6-145	9.1-15.9	1.496	**57**
Static Cross-section 1	6-143	11.3-16.5	1.496	**91**
Static Cross-section 2	6-144	11.0-16.1	1.496	**96**

A2. Dynamic US-experiments

Aorta 1	ΔP [mmHg]	ΔD [mm]	h_0 [mm]	G [kPa]
Dynamic Longitudinal	65-142	15.2-17.6	1.158	**257**
Dynamic Cross-section 1	67-135	16.2-18.2	1.158	**251**
Dynamic Cross-section 2	69-134	15.5-17.4	1.158	**235**

Aorta 2	ΔP [mmHg]	ΔD [mm]	h_0 [mm]	G [kPa]
Dynamic Longitudinal	71-134	14.7 - 16.3	1.163	**255**
Dynamic Cross-section 1	71-134	15.2 - 17.0	1.163	**269**
Dynamic Cross-section 2	72-136	15.0-16.7	1.163	**245**

Aorta 3	ΔP [mmHg]	ΔD [mm]	h_0 [mm]	G [kPa]
Dynamic Longitudinal	76-128	15.7-17.5	1.036	**269**
Dynamic Cross-section 1	76-132	17.0-19.0	1.036	**285**
Dynamic Cross-section 2	79-132	16.1-17.7	1.036	**280**

Aorta 4	ΔP [mmHg]	ΔD [mm]	h_0 [mm]	G [kPa]
Dynamic Longitudinal	73-133	14.2-16.1	1.095	**260**
Dynamic Cross-section 1	68-130	14.8-16.8	1.095	**242**
Dynamic Cross-section 2	71-132	14.3-16.1	1.095	**232**

Aorta 5	ΔP [mmHg]	ΔD [mm]	h_0 [mm]	G [kPa]
Dynamic Longitudinal	78-135	15.5-17.1	1.114	**274**
Dynamic Cross-section 1	79-136	16.2-18.0	1.114	**271**
Dynamic Cross-section 2	79-136	16.3-18.0	1.114	**269**

Aorta 6	ΔP [mmHg]	ΔD [mm]	h_0 [mm]	G [kPa]
Dynamic Longitudinal	83-133	15.0-16.3	1.246	**218**
Dynamic Cross-section 1	81-131	15.6-17.0	1.246	**238**
Dynamic Cross-section 2	80-135	15.3-16.5	1.246	**237**

Aorta 7	ΔP [mmHg]	ΔD [mm]	h_0 [mm]	G [kPa]
Dynamic Longitudinal	76-135	15.9-17.4	1.173	**252**
Dynamic Cross-section 1	74-137	16.5-18.0	1.173	**290**
Dynamic Cross-section 2	74-136	15.9-17.5	1.173	**253**

Aorta 8	ΔP [mmHg]	ΔD [mm]	h_0 [mm]	G [kPa]
Dynamic Longitudinal	73-132	14.8-16.3	1.246	**232**
Dynamic Cross-section 1	71-134	15.6-17.6	1.246	**224**
Dynamic Cross-section 2	70-134	15.0-16.8	1.246	**227**

Aorta 9	ΔP [mmHg]	ΔD [mm]	h_0 [mm]	G [kPa]
Dynamic Longitudinal	79-130	14.6-16.3	1.026	**241**
Dynamic Cross-section 1	76-127	15.5-17.0	1.026	**255**
Dynamic Cross-section 2	77-128	14.8-16.3	1.026	**249**

Aorta 10	ΔP [mmHg]	ΔD [mm]	h_0 [mm]	G [kPa]
Dynamic Longitudinal	71-133	14.8-16.3	1.246	**245**
Dynamic Cross-section 1	72-138	15.6-17.2	1.246	**294**
Dynamic Cross-section 2	72-137	15.3-16.9	1.246	**259**

Aorta 11	ΔP [mmHg]	ΔD [mm]	h_0 [mm]	G [kPa]
Dynamic Longitudinal	78-135	14.0-15.9	1.041	**229**
Dynamic Cross-section 1	81-135	14.9-16.7	1.041	**242**
Dynamic Cross-section 2	76-131	14.1-15.8	1.041	**225**

Aorta 12	ΔP [mmHg]	ΔD [mm]	h_0 [mm]	G [kPa]
Dynamic Longitudinal	78-135	15.5-17.1	1.261	**228**
Dynamic Cross-section 1	79-136	16.2-18.0	1.261	**246**
Dynamic Cross-section 2	79-136	16.3-18.0	1.261	**230**

A3. Incremental shear modulus

Aorta 1	ΔP [mmHg]	ΔP_{dyn} [mmHg]	ΔD [mm]	ΔD_{dyn} [mm]	h_{Pdia} [mm]	G_{inc} [kPa]
Incremental Longitudinal	3-141	65-136	12.3-17.3	15.8-17.3	1.167	**265**
Incremental Cross-section 1	0-141	67-135	12.6-18.4	16.7-18.3	1.127	**301**
Incremental Cross-section 2	0-140	69-134	12.0-17.5	15.9-17.4	1.129	**273**

Aorta 2	ΔP [mmHg]	ΔP_{dyn} [mmHg]	ΔD [mm]	ΔD_{dyn} [mm]	h_{Pdia} [mm]	G_{inc} [kPa]
Incremental Longitudinal	5-137	71-134	10.7-15.7	13.8-15.6	1.071	**214**
Incremental Cross-section 1	3-138	71-134	11.2-16.4	14.6-16.3	1.048	**254**
Incremental Cross-section 2	2-138	72-136	10.8-15.9	14.3-15.9	1.043	**262**

Aorta 3	ΔP [mmHg]	ΔP_{dyn} [mmHg]	ΔD [mm]	ΔD_{dyn} [mm]	h_{Pdia} [mm]	G_{inc} [kPa]
Incremental Longitudinal	4-137	76-128	10.4-17.2	15.0-17.0	0.971	**218**
Incremental Cross-section 1	3-138	76-132	12.5-18.6	17.2-18.5	1.011	**308**
Incremental Cross-section 2	3-137	79-132	11.3-17.3	15.5-17.2	1.015	**241**

Aorta 4	ΔP [mmHg]	ΔP_{dyn} [mmHg]	ΔD [mm]	ΔD_{dyn} [mm]	h_{Pdia} [mm]	G_{inc} [kPa]
Incremental Longitudinal	6-142	73-133	10.1-15.8	13.9-15.7	0.960	**233**
Incremental Cross-section 1	6-144	68-130	10.5-16.7	14.6-16.4	0.951	**246**
Incremental Cross-section 2	6-143	71-132	10.2-15.8	13.8-15.5	0.972	**232**

Aorta 5	ΔP [mmHg]	ΔP_{dyn} [mmHg]	ΔD [mm]	ΔD_{dyn} [mm]	h_{Pdia} [mm]	G_{inc} [kPa]
Incremental Longitudinal	2-141	78-135	12.5-17.1	15.8-17.1	1.015	**310**
Incremental Cross-section 1	2-140	79-136	11.8-17.6	15.8-17.4	0.966	**284**
Incremental Cross-section 2	3-141	79-136	12.2-18.0	16.5-18.0	0.955	**323**

Aorta 6	ΔP [mmHg]	ΔP_{dyn} [mmHg]	ΔD [mm]	ΔD_{dyn} [mm]	h_{Pdia} [mm]	G_{inc} [kPa]
Incremental Longitudinal	4-142	83-133	9.6-16.4	14.3-16.2	0.947	**221**
Incremental Cross-section 1	3-140	81-131	11.5-15.8	14.3-15.6	1.140	**220**
Incremental Cross-section 2	4-139	80-135	10.4-14.3	13.2-14.3	1.121	**241**

Aorta 7	ΔP [mmHg]	ΔP_{dyn} [mmHg]	ΔD [mm]	ΔD_{dyn} [mm]	h_{Pdia} [mm]	G_{inc} [kPa]
Incremental Longitudinal	1-138	76-135	12.6-17.4	16.0-17.4	1.254	**252**
Incremental Cross-section 1	2-138	73-138	12.5-17.5	16.1-17.5	1.230	**306**
Incremental Cross-section 2	1-137	74-136	11.9-16.9	15.6-16.9	1.208	**283**

Aorta 8	ΔP [mmHg]	ΔP_{dyn} [mmHg]	ΔD [mm]	ΔD_{dyn} [mm]	h_{Pdia} [mm]	G_{inc} [kPa]
Incremental Longitudinal	5-141	73-132	12.0-16.6	15.0-16.6	1.148	**234**
Incremental Cross-section 1	5-141	71-134	11.6-16.4	14.3-16.2	1.166	**204**
Incremental Cross-section 2	9-142	70-134	10.5-15.9	13.7-15.7	1.100	**211**

Aorta 9	ΔP [mmHg]	ΔP_{dyn} [mmHg]	ΔD [mm]	ΔD_{dyn} [mm]	h_{Pdia} [mm]	G_{inc} [kPa]
Incremental Longitudinal	8-143	79-130	8.2-16.2	13.5-15.8	0.783	**224**
Incremental Cross-section 1	10-145	76-127	11.2-17.2	14.3-16.7	1.009	**184**
Incremental Cross-section 2	11-144	77-128	10.6-16.1	13.6-15.7	1.000	**190**

Aorta 10	ΔP [mmHg]	ΔP_{dyn} [mmHg]	ΔD [mm]	ΔD_{dyn} [mm]	h_{Pdia} [mm]	G_{inc} [kPa]
Incremental Longitudinal	1-135	71-133	11.9-15.8	14.1-15.8	1.263	**206**
Incremental Cross-section 1	1-138	73-137	11.7-16.6	15.1-16.6	1.159	**266**
Incremental Cross-section 2	1-137	72-137	12.1-16.8	15.1-16.8	1.202	**232**

Aorta 11	ΔP [mmHg]	ΔP_{dyn} [mmHg]	ΔD [mm]	ΔD_{dyn} [mm]	h_{Pdia} [mm]	G_{inc} [kPa]
Incremental Longitudinal	11-136	78-135	10.1-15.6	13.4-15.6	0.967	**205**
Incremental Cross-section 1	11-135	81-135	11.2-15.6	13.4-15.6	1.079	**170**
Incremental Cross-section 2	9-135	76-135	10.8-14.6	13.2-14.6	1.058	**220**

Aorta 12	ΔP [mmHg]	ΔP_{dyn} [mmHg]	ΔD [mm]	ΔD_{dyn} [mm]	h_{Pdia} [mm]	G_{inc} [kPa]
Incremental Longitudinal	6-145	80-134	9.1-15.9	14.1-15.7	0.968	**232**
Incremental Cross-section 1	6-143	77-134	11.3-16.5	14.7-16.3	1.151	**206**
Incremental Cross-section 2	6-144	77-134	11.0-16.1	13.9-15.8	1.187	**181**

B. Abstract – ITEC 2014

This work was submitted as abstract to the 13th International Tissue Elasticity Conference (Snowbird, Utah, USA, September 7 – 10, 2014) and was accepted to be presented at the conference. The abstract was published in the *2014 ITEC Proceedings*.

###	**IN VITRO VALIDATION OF VASCULAR ELASTOGRAPHY: FROM INFLATION TEST TOWARDS IN VIVO MEASUREMENTS**
	Edgar J. S. Mascarenhas, Mathijs F.J. Peters, Marcel C.M. Rutten, Frans N. van de Vosse, Richard G.P. Lopata
	Eindhoven University of Technology, Department of Biomedical Engineering, Eindhoven, THE NETHERLANDS;

Background: Rupture of aortic aneurysms (AA) is a major cause of death in the western countries. Currently, clinical decision upon surgical intervention is based on maximum diameter measurements, which is proven to be an unreliable criterion [1]. From a biomechanical perspective, rupture of AA occurs when wall stress locally surpasses the strength of the wall. Thus, noninvasive assessment of the elastic properties of the vessel wall by means of vascular ultrasound (US) elastography might be a better indicator for AA growth and rupture risk. US elastography has been introduced to estimate material properties in coronaries, carotids and aortas [2-4]. To validate these *in vivo* elastography measurements, *ex vivo* inflation testing of aortas was performed and validated using bi-axial tensile testing [5].

Aims: To estimate the mechanical properties of the aortic wall using inflation testing and 2D US elastography, and investigate the performance of the method for physiological conditions.

Methods: Twelve porcine aortas were mounted in an experimental setup filled with physiological saline solution at a set temperature of 37°C. A physiological longitudinal pre-stretch of 1.22 was applied to all aortas. Two different types of *in vitro* inflation US-experiments were performed: 1) a static US-experiment, wherein the elasticity of the aortic wall was tested for a complete pressure range (0 – 140 mmHg) for uniform steps in strain (1.2 %); 2) a dynamic experiment in a sophisticated mock circulation setup in which the aorta was subjected to physiological pressures closely mimicking the *in vivo* hemodynamics (70 – 130 mmHg). One longitudinal and two cross-sectional 2D US datasets were acquired for both experiments using a Mylab70 US scanner equipped with a 7MHz linear array probe and RF interface (Esaote, NL). The RF-data were manually segmented, yielding the initial wall thickness and diameter. RF-based 2D displacement tracking [5] was applied to all datasets to obtain the diameter as a function of time. A linear elastic, isotropic material model (Neo-Hookean) was chosen to describe the mechanical behavior. The shear modulus G was estimated. In addition, an incremental study based on the static data was performed to: 1) investigate the changes in G for increasing mean arterial pressure (MAP) for a certain pressure difference (30, 40 and 50 mmHg), and, 2) compare the results with those obtained from the analysis of the dynamic US data sets, taking into account the same physiological pressure range.

Results: The resulting shear modulus *G* was 94 ± 16 kPa for the static experiment, which is in agreement with a previous study [5]. The dynamic data revealed a *G* of 250 ± 20 kPa. In general, a linear dependency on MAP was found for *G* in the incremental analysis, however, the effect of the pressure difference was negligible. For the same pressure range, the incremental shear modulus (G_{inc}) was 240 ± 39 kPa and good agreement was found with the dynamic US-experiment using Bland-Altman analysis. However, the dynamic US-experiment revealed a higher precision reproducibility. In all experiments, no significant differences were found in *G* between the different image planes, with the exception of the two cross-sections during dynamic testing (paired sample Student's t-test, p-value=0.01<0.05).

Conclusions: In this study, 2D US elastography of aortas during inflation testing is feasible under controlled and physiological circumstances. Dynamic moduli were estimated with low variability (< 10%) and were in good agreement with standard inflation tests (bias < 10 kPa). In future studies, the *in vivo*, dynamic experiment should be conducted for a range of MAPs and pathological vessels should be examined. Furthermore, the use of more complex material models needs to be considered to describe the non-linear behavior of the vascular tissue.

Acknowledgements: This project is granted by the Dutch Technology Foundation (VENI 11885)

References:

[1] Choksy et al. (1999), "Ruptured abdominal aortic aneurysm in the Huntingdon district: a 10-year experience", *Annals of the Royal College of Surgeon of England*, 81(1), pp. 27-31.
[2] de Korte et al. (2003), "Morphological and mechanical information of coronary arteries obtained with intravascular elastography; feasibility study in vivo". *European Heart Journal, 23(5)*, pp. 405-413.
[3] Ribbers et al. (2007), "Noninvasive two dimensional strain imaging of arteries: validation in phantoms and preliminary experience in carotid arteries in vivo", *Ultrasound in Medicine and Biology*, 33(4), pp. 530-540.
[4] Fromageau (2008), "Noninvasive vascular ultrasound elastography applied to the characterization of experimental aneurysms and follow-up after endovascular repair", *Physics Med Biol*, 30(9), pp. 1173-83.
[5] Lopata et al. (2014), "Vascular elastography: a validation study", *Ultrasound Med Biol*, 40(8), pp. 1882-95.